IPP-Report

Max-Planck-Institut
für Plasmaphysik

Philipp Nelde

Influence of Systematic Errors on the Electron Density and Temperature Measured with Thomson Scattering at W7-X

IPP 2021-07
Februar 2021

INFLUENCE OF SYSTEMATIC ERRORS ON THE ELECTRON DENSITY AND TEMPERATURE MEASURED WITH THOMSON SCATTERING AT W7-X

MASTER THESIS

Zentrum für Astronomie und Astrophysik

Technische Universität Berlin

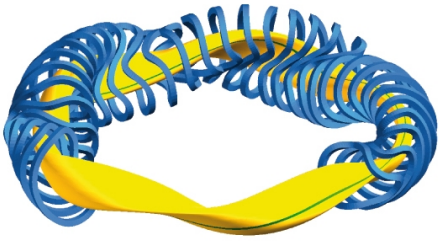

AUTHOR:

Philipp Nelde

FIRST EXAMINER:

Prof. R. C. Wolf

SECOND EXAMINER:

Prof. D. Breitschwerdt

SUPERVISOR:

Dr. G. Fuchert

18. September 2020

Philipp Nelde: *Influence of Systematic Errors on the Electron Density and Temperature measured with Thomson Scattering at W7-X*, Master Thesis, 18. September 2020
Title page image by courtesy of IPP

ABSTRACT

This thesis focuses on the analysis of systematic errors of the Thomson scattering diagnostic at Wendelstein 7-X, the world's most advanced stellarator. The measured electron density and temperature profiles show features which, according to present estimates of the error bars are significant, but that are unphysical. As the electron density and temperature are important parameters to understand the physics of Wendelstein 7-X, reliable measurements and good knowledge of the measurement error are vital for all analyses involving profile data. This also holds for comparison with theoretical predictions and other stellarators. The work of this thesis has shown that single time point measurements of the diagnostic have to be taken with caution because of positional fluctuations of the lasers. As a consequence, the beam position has to be measured for all time points in the future, taking a calibration for every possible beam position. Furthermore, it could be shown that observed spectral calibration errors cannot explain the unphysical features in the profiles. Concluding, further investigations have to be done to improve the significance of the measurements.

ZUSAMMENFASSUNG

Im Rahmen dieser Arbeit wurden systematische Fehler der Thomson-Streuungs Diagnostik am Wendelstein 7-X, dem modernsten Stellarator der Welt, analysiert. Die gemessenen Elektronendichte- und Elektronentemperaturprofile zeigen Eigenschaften, die aufgrund aktueller Fehlerabschätzungen signifikant, aber unphysikalisch sind. Die Elektronendichte und -temperatur sind wichtige Parameter zum Verständnis der Physik am Wendelstein 7-X. Deshalb sind zuverlässige Messungen und eine gute Kenntnis der Messfehler entscheidend für alle Analysen die Profildaten benötigen. Dies gilt weiterhin für Vergleiche mit theoretischen Vorhersagen oder mit anderen Stellaratorexperimenten. In dieser Arbeit konnte gezeigt werden, dass Einzelschussmessungen der Thomson Diagnostik mit Vorsicht behandelt werden müssen, da positionelle Variationen der Laser die Messung beeinflusst haben. Als Folge daraus muss in Zukunft die Position der Laser für alle Zeitpunkte gemessen und eine positionsabhängige Kalibrierung durchgeführt werden. Weiterhin konnte gezeigt werden, dass beobachtete Fehler in der spektralen Kalibrierung nicht die unphysikalischen Eigenschaften der Profile erklären können. Zukünftig sollen noch weitere Untersuchungen durchgeführt werden, um die Signifikanz der Messungen weiter zu verbessern.

CONTENTS

LIST OF FIGURES

Part I

INTRODUCTION

1 INTRODUCTION

Our modern society has a still rising demand of electrical energy. As a consequence, fossil fuels are depleting and new sources for electrical power have to be found [1]. Nuclear fission is still a major resource, but reactor accidents have catastrophic environmental consequences and history has shown that those accidents can happen. Additionally, the problem of the disposal of the highly radioactive waist is still unresolved.
Regenerative energies like wind, water or solar energy have the disadvantage of low efficiencies and strongly varying output depending on changing weather conditions. Consequently, the research in the field of generating electrical power still has a large impact on the modern society.
Thinking about how the sun generates heat, another possible source comes to mind: nuclear fusion. Instead of splitting a large unstable nucleus into more stable smaller nuclei and converting the difference in binding energy into kinetic energy (nuclear fission), nuclear fusion works by combining smaller nuclei into a more stable larger nucleus. In the sun various fusion reactions take place, e.g. the proton-proton chain reaction which forms a helium ion out of hydrogen ions via intermediate formation of deuterium and tritium ions. Because hydrogen is easily available on earth, fusion seems to be a good candidate for future power generation. However, the way fusion works in the sun would not be applicable on earth because the process in the sun depends on the high pressure, resulting from the gravitational force at the suns core. Even with this high pressure, the average reaction time for the first step of the proton-proton chain reaction is on the order of ten billion years [2, p. 56].
In order to realise fusion on earth, the underlying processes have to be understood. The hot hydrogen and helium 'gas' of the sun does not behave like a 'normal' gas or fluid. Because of the high temperatures, essentially all atoms are ionised. This means that the sun consists of non-bound electrons and ions. These charged particles can interact via electromagnetic forces on larger distances than normal gases could, giving this 'hot gas' unique properties, which is therefore called a plasma. Because a gas changes to a plasma by applying heat, it is sometimes called the fourth state of matter. Also in nature on earth plasmas can be observed, for example in lightnings or auroras. But not every plasma is suitable for fusion generators on earth. In order to create a fusion generator, the losses in the system have to be overcompensated by the generated fusion heat. One major factor is the rate at which fusion collisions between the ions happen. This rate depends on factors like the ion temperature and density, but also on the time they spend in hot plasma regions. In the sun this time is very long, because the gravitational forces trap the particles inside the sun. On earth such high gravitational forces cannot be created. Other ways of trapping the particles have to be found.
As a plasma consists of charged particles, confinement in magnetic fields seems to be an applicable option. Two main types of magnetic confinement devices are considered as possible solutions: tokamaks and stellarators. This thesis is conducted at Wendelstein 7-X, the most advanced stellarator currently existing. The main goal of Wendelstein 7-X is to prove that a plasma can be confined in a stellarator at fusion relevant conditions.

To prove fusion relevant conditions and to control plasma confinement, the plasma parameters have to be measured. Two important parameters are the electron density and temperature. One diagnostic capable of measuring both, is the Thomson scattering system, which is well established in plasma experiments and is able to give time and spatially resolved profiles. The diagnostic works by firing high energy laser pulses into the plasma and analysing the light scattered by free plasma electrons, which is called Thomson scattering. This thesis focuses on the analysis of systematic errors of the Thomson scattering diagnostic and aims to evaluate the impact of those errors on the measurements. The knowledge of the measurement errors is particularly important because many analyses use the electron density or temperature as input parameters and consequently propagate these errors. Another aspect is that in order to compare the measurements with theoretical models or measurements at other plasma experiments, the error margins have to be known well.

One reason for starting this thesis was the observation that the measured electron density profiles show features outside the currently estimated error margins, which are unphysical, hinting that some systematic errors are not taken into account. This thesis will show that the positional stability of the Thomson laser system is an important factor regarding the measurement of the electron density and it will be shown that errors in the spectral calibration of the Thomson scattering diagnostic can likely not explain the unphysical features in the profiles.

Before the detailed analysis of the two mentioned systematic errors, a brief definition of a plasma and fusion relevant conditions will be given. Followed by a description of the underlying principles of the Thomson scattering diagnostic and analysis tools used in this thesis. Afterwards, a brief overview of the components of the diagnostic and a summary of the experiments conducted for this thesis will be given. Finally, the analysis and discussion of the results follow.

Part II

THEORETICAL BACKGROUND

2

THEORETICAL BACKGROUND

2.1 PLASMA PHYSICS

This section will give a short introduction to plasma physics, starting with a definition, and ending with plasma characteristics and important parameters. Because there is a wide range of plasmas, this work will focus mainly on W7-X-relevant ones.
In contrast to a gas or fluid, a plasma consists of charged particles which can interact over long distances, mediated by electromagnetic forces. The interaction between neutral particles in a gas or fluid is usually dominated by short range collisions. This difference in interaction distances leads to strongly different behaviour, for example when perturbations are applied to the system, leading to one definition of an ideal plasma given by F. F. Chen: 'A plasma is a quasi-neutral gas of charged and neutral particles which exhibits collective behavior.' [3, p. 2]
This has to be ambiguous, because in contrast to the usual states of matter, the plasma state has no phase transition. Starting from the definition given by Chen, mathematical conditions that have to be fulfilled to count as an *ideal* plasma can be stated [3, pp. 1–11].
The word *quasi-neutral* means that, while the plasma consists of charged particles, there is little excess charge, and the charged particles are distributed evenly. This means that the electron density n_e and atomic number Z times the ion density n_i are roughly the same: $n_e \simeq Zn_i$.
Quasi-neutrality is closely related to Debye shielding, which is the effect whereby a plasma shields electric fields. Imagine a positive point charge placed in a plasma. Because the plasma contains free moving electrons, they will gather around the charge, and in turn, screen it. It could also be assumed that a negative charge would be shielded by the positive charged ions. In reality, the mass of the ions is orders of magnitude larger than the electron mass, leading to the electrons responding more quickly to perturbations, moving away from the negative charge and leaving the positive ion background behind. Concluding, excess charges will be screened on the timescale of the electron motion.
The spatial length it takes to shield the excess charge is called Debye length λ_D. More formally, if there is an unshielded electrostatic potential Φ_0, then the shielded potential Φ along the spatial dimension r can be described by: $\Phi(r) = \Phi_0 e^{-\frac{r}{\lambda_D}}$. The Debye length can be derived from Poisson's equation and depends on the electron temperature T_e and density: $\lambda_D = \left(\frac{\epsilon_0 k_B T_e}{n_e e^2}\right)^{\frac{1}{2}}$, with ϵ_0 being the vacuum permittivity and k_B the Boltzmann constant. Therefore, the first condition of being a plasma should be that the length L of the plasma should be greater than the Debye length:

$$L \gg \lambda_D \tag{2.1}$$

For the shielding to work, there have to be enough free moving particles in the space around the perturbation, which is characterised by a sphere with radius λ_D, which is therefore called Debye sphere. The number N_D of electrons (screening particles) in this

sphere is given by: $N_D = \frac{4}{3}\pi\lambda_D^3 n_e$. Without giving a specific number the second condition for being a plasma consequently is:

$$N_D \gg 1 \tag{2.2}$$

For the plasma to exhibit collective behaviour like e.g. plasma waves, the electromagnetic forces have to be able to compete with collisions with neutrals, which would suppress such behaviour. Therefore, the characteristic collision time with neutrals τ has to be large compared to the frequency ω of common plasma oscillations:

$$\tau\omega > 1 \tag{2.3}$$

As explained before, in terms of a definition the three conditions are a bit vague, but a wide range of ideal plasmas, including fusion plasmas can be described by them. In any case, some important plasma parameters were introduced: the densities n_e and n_i, electron temperature T_e, plasma frequencies ω and the collision time τ. Because this work is oriented towards nuclear fusion, the parameters relevant for fusion will be discussed in the next section.

2.2 NUCLEAR FUSION

Nuclear fusion is the reaction whereby two smaller atomic nuclei fuse into a larger nucleus. If the resulting larger nucleus is more stable than the reactants, the process is exothermic. Regarding atomic nuclei, more stable means that the binding energy per nucleus is larger. The goal of fusion research is to trigger fusion processes in a controlled environment and harness the excess energy. To be able to do that, the underlying processes and physical requirements have to be understood. In the following section the most promising fusion reaction and a criterion for self sustaining fusion (point of ignition) will be discussed.

2.2.1 *Fusion reaction*

The most promising candidate for controlled nuclear fusion as an energy source on earth is the fusion of hydrogen isotopes to helium. One reason for that is the abundance of hydrogen in the universe and on earth and another is the considerable difference in binding energy, resulting in a lot of energy being released during a fusion reaction. There are several reactions between hydrogen (^{1}H) and its isotopes deuterium (^{2}H) and tritium (^{3}H). The one with the highest fusion probability (highest cross section) is the reaction between deuterium and tritium [4, p. 18][5][6]:

$$^2\mathrm{H} + {}^3\mathrm{H} \longrightarrow {}^4\mathrm{He} + \mathrm{n} + 17.6\,\mathrm{MeV} \tag{2.4}$$

Deuterium and tritium fuse to helium (^{4}He) and a neutron (n) is emitted. Because of momentum and energy conservation, the released energy of 17.6 MeV is divided between the two particles according to their mass ratio. This leads to the largest amount of kinetic energy (14.1 MeV) being carried by the neutron. As it is advantageous that only one particle species carries most of the energy, it also presents technical difficulties for fusion devices because the highly energetic neutrons can deteriorate the device and its diagnostics [7, pp. 51–59]. On the other hand, having highly energetic neutrons also gives the opportunity to breed tritium in so-called blankets and thus create fuel for the reactor as a by-product [8].

2.2.2 *Lawson criterion*

In section 2.1 important plasma parameters were introduced. In the last section the fusion reaction of interest was discussed. Now the question is, which combinations of plasma parameters can make that reaction happen in a way that a reactor can be built around that process. In the optimal case, the reaction has to be initiated (ignited) once and afterwards it continues on its own (except for refuelling). For that, the losses and the fusion rate have to be evaluated. To reach the point of ignition, the losses P_l have to be compensated by the generated fusion heat. Because the fast neutrons will not have enough collisions with the plasma, the heat has to come from the helium nuclei P_{He}. The point of ignition is consequently reached when:

$$P_l = P_{\mathrm{He}} \tag{2.5}$$

The reaction power can be calculated by multiplying the reaction energy E_R with the reaction rate f_R. In the case of deuterium tritium fusion, the reaction energy of the helium nuclei is 3.5 MeV. The reaction rate is given by:

$$f_R = n_D n_T \langle \sigma_{DT} v_r \rangle \tag{2.6}$$

where n_D and n_T are the densities of deuterium and tritium, σ_{DT} is the aforementioned cross section, and v_r is the relative velocity between the two species. The $\langle\rangle$ brackets denote the average over the velocity distribution. In thermal equilibrium the velocity distribution can be described by the Maxwell-Boltzmann distribution. The cross section σ_{DT} has to be inside the brackets, because it is velocity dependent. The term $\langle \sigma_{DT} v_r \rangle$ is also called fusion rate coefficient and has its maximum at an ion temperature of about 70 keV. As a side note, in the fusion community the temperature is usually given in energy units of keV, meaning $T \equiv k_B T$, with k_B being the Boltzmann constant. From this point onward these energy units will be used for the temperature.
Making the assumption that both densities are equal to half the so-called plasma density $\frac{n_p}{2} \equiv n_D = n_T$, the reaction power can be written as:

$$P_{\mathrm{He}} = \frac{1}{4} n_p^2 \langle \sigma_{DT} v_r \rangle E_R \tag{2.7}$$

This power has to be equal to the losses for reaching the ignition condition. The losses consist of heat losses (e.g. particle losses, heat transfer) and radiative losses (e.g. bremsstrahlung, line emission). The heat losses can be described by $\frac{P_{th}}{\tau_E}$. Where P_{th} is the sum of the thermal energy ($\frac{3}{2} nT$) of the three particle species (deuterium, tritium, electron) and τ_E is the energy confinement time. This energy confinement time is a characteristic time scale for thermal insulation.
In pure hydrogen plasmas, the radiative losses can mainly be described by bremsstrahlung which is caused by a changing momentum of a charged particle. The main radiating component are the electrons which radiate the power [4, pp. 102–103]:

$$P_{brems} = \frac{e^2}{6\pi\epsilon_0 c^3} a^2 \tag{2.8}$$

with ϵ_0 being the vacuum permittivity, c vacuum light velocity and a the acceleration. The acceleration originates from collisions with other charged particles (e.g. ions) due

to the Coulomb force. Approximating collision rates and integrating over all possible collision parameters (collision distances) gives an approximate result for the radiated power [4, pp. 102–103]:

$$P_{\text{brems}} = \frac{8\pi}{\sqrt{3}} \frac{T_e^{1/2}}{(4\pi\epsilon_0)\, m_e^{3/2} c^3 h} n_e n_i Z^2 \tag{2.9}$$

with h being Planck's constant and n_i the ion density. This approximation does not include quantum mechanical corrections and only takes the mean electron velocity for the collisions. It is important to note that if there were impurities in the plasma, they might add a considerable amount of bremsstrahlung as the dependence on the proton number Z is quadratic and line radiation might also contribute.
Putting both, the heat and radiative losses, into the power balance equation, gives an ignition condition for the so-called Lawson parameter $n_p \tau_E$:

$$n_p \tau_E > 1.5 \times 10^{20}\, \text{m}^{-3}\text{s} \tag{2.10}$$

In principle this so-called Lawson criterion is temperature dependent. The given value is only valid at the optimum temperature. It is also not trivial to just increase the plasma density to increase the Lawson parameter because if the heating power is insufficient the ion temperature might drop, changing the whole parameter. A parameter more fit to represent the overall capability to reach ignition is the so-called fusion triple product, which is used as a figure of merit in the fusion community. This triple product is the Lawson parameter multiplied with the ion temperature: $n_p \tau_E T$. The ignition condition at the optimal temperature for the triple product gives [9, p. 11]:

$$n_p \tau_E T > 3 \times 10^{21}\, \text{m}^{-3}\text{skeV} \tag{2.11}$$

Even this figure of merit is only really comparable at fusion relevant n_e and T. With an optimal temperature present, two parameters, density and confinement time, can be adjusted.
Two concepts for achieving fusion/ignition relevant conditions emerged: inertial confinement fusion and magnetic confinement fusion. In inertial confinement fusion, a frozen pellet of deuterium and tritium is heated by e.g. powerful lasers to reach the ignition point and to get many fusion reactions in the short time period before the pellet expands/explodes. In contrast, a magnetic trap is designed to reach long confinement times. In order to reach these, the magnetic confinement device has to counter the plasma pressure. The magnetic pressure the device can exert is limited technically and thus the maximum plasma pressure is limited as well. As the plasma pressure is proportional to both density and temperature, by default its product is limited and consequently the fusion cross sections that can be achieved are as well.

2.3 STELLARATOR AND TOKAMAK

There are two main concepts for achieving magnetic confinement: tokamak and stellarator [1]. Both were created in the 1950's. The tokamak was first developed in Russia and the stellarator originates from the US. The foundation of both concepts is to confine the plasma in toroidal magnetic fields.
Early research showed that a linear arrangement like a mirror trap was always going

to lose the particles with the highest energy, making that kind of device irrelevant for fusion. The next step in the process was thinking about bending a coil into a torus and creating the plasma inside, to have closed magnetic field lines on which the particles could travel. However, in this concept the magnetic field inside the torus gets weaker with growing major radius. This is caused by the higher winding number density on the inboard side compared to the outboard side of the vessel. A non homogeneous magnetic field leads to a net drift of the plasma. Thus no confinement can be achieved. The general trick to overcome this is to twist the magnetic field lines so that a particle moving along that line is moving through both, the low and high field side, leading to a negligible net drift. To create such a magnetic field, not only a *toroidal* magnetic field, but also a *poloidal* field has to be created. The toroidal and poloidal directions, used in toroidal coordinates, can be seen in figure 2.1. How the poloidal field component is realized is the main difference between the two confinement concepts. The tokamak creates the poloidal field by inducing a toroidal current in the plasma. To keep inducing a current in the plasma, the prime current (responsible for the induction) has to be increased continuously. This is limited technically, because an infinite current can not be created. In consequence, such a device cannot be operated in steady-state. Another downside is that current-disruptions caused by instabilities can cause the termination of the plasma and a tokamak can only withstand a limited number of these disruptions.
In contrast to that, the stellarator creates the poloidal field without a plasma current, but by making the coil structure more complex. Nowadays, non planar coils are being used for that purpose. The geometry of the coils is calculated beforehand by optimisation routines and simulations. For the device to work as planned the actual realisation of the coil geometry has to match the model to 99.9 % [10].
While W7-X's main goal is to show that fusion relevant conditions can be reached in a stellarator, the latest tokamak ITER is being built in France to generate ten times more fusion power than heating power. ITER should be finished in the mid twenties, but the final power output will not be reached for some years, because the device will be tested and plasma experiments are carried out to understand the machine and its parameters before conducting actual fusion experiments.
After this brief description of the two concepts, W7-X will be described in the next section to give a rudimentary description of its goal and structure.

2.4 WENDELSTEIN 7-X

Today, Wendelstein 7-X is the most modern stellarator in the world. It is operated by the Max-Planck-Institut für Plasmaphysik and began operation in 2015. According to the W7-X team its 'main objective [...] is the demonstration of steady-state plasma at fusion relevant plasma parameters' [11]. The name Wendelstein is an homage to one of the first devices in the US being called Matterhorn. W7-X is an optimised stellarator. More precisely, the magnetic configuration was optimised regarding a number of criteria and then the coil geometry needed to create this configuration was being calculated. W7-X is located in Greifswald (Germany) and is the successor of the Wendelstein 7-AS which was located in Garching (Germany). A schematic of W7-X is provided in figure 2.2. The coil system consists of 50 non-planar superconducting coils (shown in red), generating the magnetic field for plasma confinement and 20 planar superconducting coils (shown in orange) built around them, allowing adjustments of the vertical position of the plasma

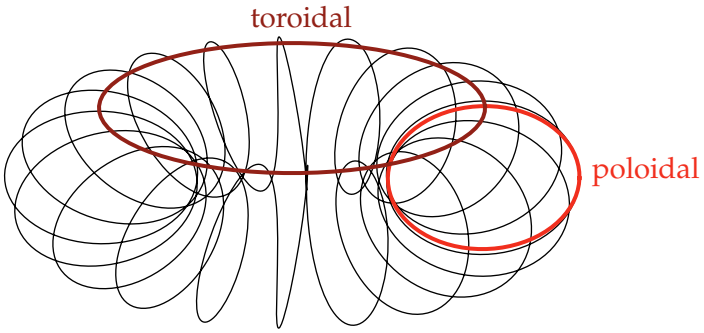

Figure 2.1: Example of a toroidally closed field line (black). Because of the toroidal symmetry of the magnetic field, toroidal coordinates are often used in tokamaks and stellarators. The two angular directions, poloidal and toroidal, are shown in red or dark red, respectively.

in the vessel and the *rotational transform*, enabling the exploration of a wide range of operational regimes. The rotational transform describes, how twisted the field lines are (number of poloidal turns per toroidal turn). A rotational transform of 0 would mean a regular toroidal field line. In W7-X it can be adjusted from approximately 0.8 to 1.25 [12]. The major radius (torus coordinates) of W7-X is 5.5 m. The minor radius changes with the differently shaped coils. The effective/average minor radius is 0.55 m. The average plasma volume is approximately 30 m^3. For comparison, the predecessor (W7-AS) had a plasma volume of 1 m^3 [13] and the tokamak ITER will have a plasma volume of 830 m^3 [14]. The size is important because the smaller the ratio of surface to volume, the better the thermal isolation. The particle losses happen at the surface. This makes the proportional heat losses smaller for smaller surface to volume ratios. With decreasing losses the already mentioned energy confinement time τ_E gets bigger and a higher triple product can be achieved.
To prove fusion relevant conditions a high triple product is an indicator. So the measurement of the plasma density and temperature as well as the energy confinement time is of huge importance for W7-X. This thesis focuses on one method to measure the electron density n_e and temperature T_e: Thomson scattering. This method and underlying physics will be described in the next section.

2.5 THOMSON SCATTERING

2.5.1 *Overview*

In plasma physics the temperature is usually given in energy units, by multiplying with the Boltzmann constant k_B. The aforementioned ion temperature of 70 keV (maximum of the fusion cross section) gives about 800 million Kelvin. The temperatures at W7-X will be below that, but still tens of million Kelvin can be reached. As a comparison: the materials with the highest known melting points are still below 5000 K [16]. Consequently, there is no material that could withstand the plasma particle energies and heat fluxes without polluting or terminating the plasma. A method without contact is needed.
Thomson Scattering is the method of choice for measuring spatially resolved profiles

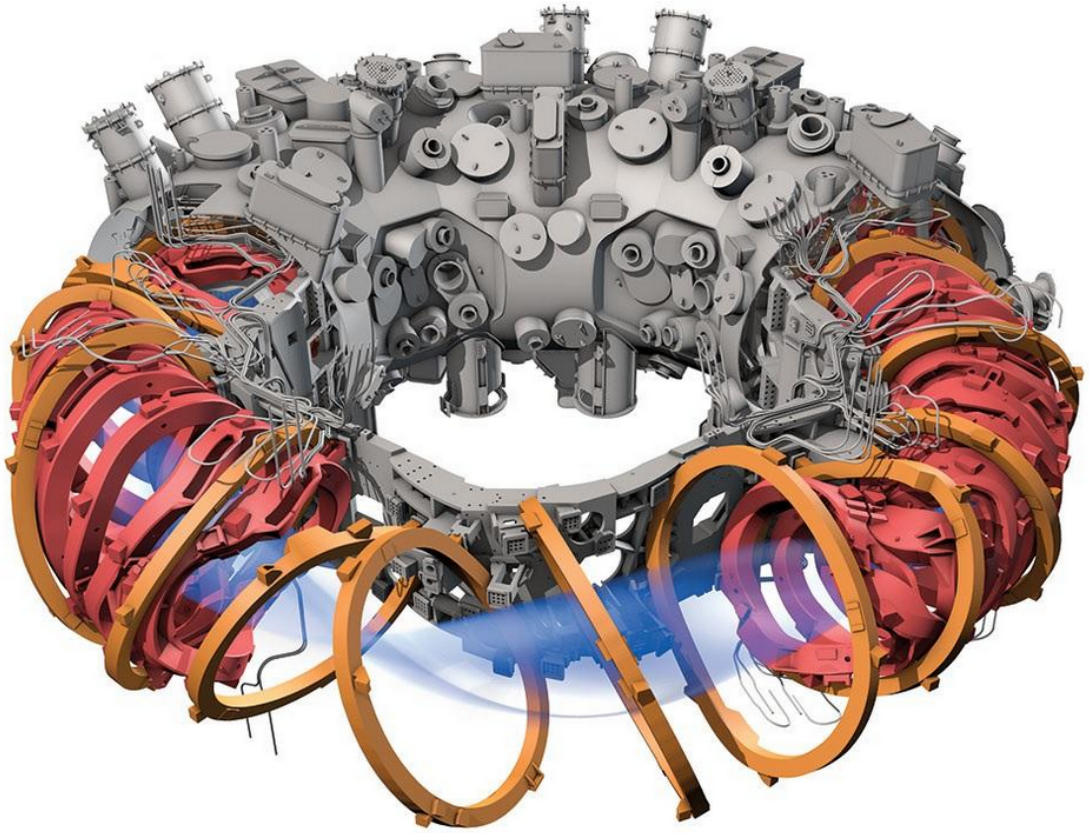

Figure 2.2: Schematic of W7-X. Visible are different layers and coil structures of the plasma vessel. For better visibility only a part of the stainless steel casing with various access ports is depicted in grey. The non-planar coils are coloured in red (also only partially depicted), and the planar coils are coloured in orange. An example plasma shape is shown in blue. Missing are the trim coils (placed outside the vessel), the plasma vessel wall, various diagnostics, supplies for cooling and power, and holding structures. Taken from [15]

of the electron density and temperature in many plasma experiments [17–21]. It was named after J. J. Thomson, who was experimenting with cathode rays and proved the existence of the electron experimentally [22]. The foundation of Thomson scattering is that low energy radiation scattered by free electrons can be described as dipole radiation. Because of the high temperatures and with that high electron velocities, a relativistic treatment is necessary (for W7-X).
The following short derivation of the Thomson scattering formula mainly follows Hutchinson [23]. The goal of this derivation is to show that the electron temperature as well as the electron density can be determined. The former by analysing the scattered spectrum, the latter by the total scattered power. First, Thomson scattering will be derived for a single electron and then for the many electron case. Last, the equation used to analyse the measurements at W7-X will be presented.

2.5.2 *Single electron Thomson scattering*

The basic requirement for Thomson scattering is that the incident photon mass m_p is small compared to the electron rest mass m_e:

$$m_p = \frac{\hbar\omega_i}{c^2} \ll m_e \tag{2.12}$$

In this notation $\hbar$ stands for the reduced Planck constant, ω_i for the incident photon angular frequency and c for the vacuum light velocity. If this assumption holds, the change in electron momentum after the scattering process becomes negligible and a purely wavelike treatment of the light is sufficient. Hence, Thomson scattering can be described as the low energy limit of Compton Scattering.
By treating the incident light as a wave and the electron as a free charge with relativistic momentum $\boldsymbol{p_e}$ the equation of motion of the electron is described by the Lorentz force:

$$\frac{\partial}{\partial_t}\boldsymbol{p_e} = \frac{\partial}{\partial_t}\left(\gamma m_e \boldsymbol{v_e}\right) = -e(\boldsymbol{E} + \boldsymbol{v_e} \times \boldsymbol{B}) \tag{2.13}$$

With the Lorentz factor γ, the electron velocity $\boldsymbol{v_e}$, the electron charge e, the electric field strength $\boldsymbol{E}$ and the magnetic flux density $\boldsymbol{B}$. In the following the electron velocity will be expressed in units of the light velocity: $\boldsymbol{\beta} = \frac{1}{c}\boldsymbol{v_e}$.
This equation of motion can be combined with the radiation equation of an accelerated charge to give the general equation for Thomson scattering. Before stating the equation, the scattering geometry is visualised in figure 2.3. Properties belonging to the incident wave are marked with an i and properties belonging to the scattered wave are marked with an s. Vectors are denoted with a bold font and normalised vectors are indicated by a hat. The scattering plane is defined by the incident wave propagation direction $\hat{\boldsymbol{i}}$ and the scattered wave propagation direction $\hat{\boldsymbol{s}}$.
The incident electric field $\boldsymbol{E_i}$ is polarised in direction $\hat{\boldsymbol{e}}$ and has a wave vector $\boldsymbol{k_i}$. The scattering particle (electron) is marked with a black dot and its velocity $\boldsymbol{\beta}$. Taking these

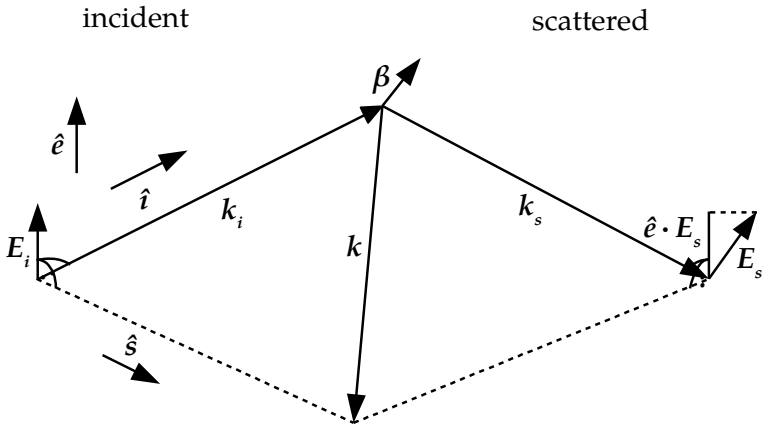

Figure 2.3: Scattering geometry. The incident electromagnetic wave travels in direction $\hat{\boldsymbol{i}}$ with wave vector $\boldsymbol{k_i}$ and electric field $\boldsymbol{E_i}$. It is polarized in direction $\hat{\boldsymbol{e}}$, perpendicular to the scattering plane. After scattering with an electron (black dot) with velocity $\boldsymbol{v} = c\boldsymbol{\beta}$, the wave vector becomes $\boldsymbol{k_s}$ and the polarization might change, noted by the non perpendicular scattered electric field $\boldsymbol{E_s}$. Also denoted is the scattering vector $\boldsymbol{k} = \boldsymbol{k_s} - \boldsymbol{k_i}$.

notations, the general equation for the Thomson scattered electric field of one electron becomes:

$$\begin{aligned}\boldsymbol{E_s}(t) = r_e \Bigg[\frac{E_i \left(1-\beta^2\right)^{\frac{1}{2}}}{R \left(1-\beta_s\right)^3} \Big(& -\left(1-\beta_i\right)\left(1-\beta_s\right)\hat{\boldsymbol{e}} - \beta_e \left(1-\beta_s\right)\hat{\boldsymbol{i}} \\ & + \left(\left(1-\beta_i\right)\hat{\boldsymbol{s}}\cdot\hat{\boldsymbol{e}} + \left(\hat{\boldsymbol{s}}\cdot\hat{\boldsymbol{i}} - \beta_s\right)\beta_e\right)\hat{\boldsymbol{s}} \\ & - \left(\left(1-\beta_i\right)\hat{\boldsymbol{s}}\cdot\hat{\boldsymbol{e}} - \left(1-\hat{\boldsymbol{s}}\cdot\hat{\boldsymbol{i}}\right)\beta_e\right)\boldsymbol{\beta}\Big) \Bigg]_{t'}\end{aligned} \tag{2.14}$$

Where r_e is the classical electron radius, and β_i and β_s are the projections of $\boldsymbol{\beta}$ onto the incident $\hat{\boldsymbol{i}}$ or scattered direction $\hat{\boldsymbol{s}}$, respectively. Note that the equation has to be evaluated at the retarded time t' which takes into account that the electromagnetic wave travels with (finite) light velocity from the scattering particle to the observer.
In a usual Thomson scattering diagnostic, the incident wave is polarised linearly and perpendicular to the scattering plane and only the perpendicular part of the scattered wave is detected. This simplifies the equation to:

$$\hat{\boldsymbol{e}}\cdot\boldsymbol{E_s}(t) = r_e \left[\frac{E_i \left(1-\beta^2\right)^{\frac{1}{2}}}{R \left(1-\beta_s\right)^3} \left(\left(1-\hat{\boldsymbol{s}}\cdot\hat{\boldsymbol{i}}\right)\beta_e^2 - \left(1-\beta_i\right)\left(1-\beta_s\right)\right) \right]_{t'} \tag{2.15}$$

Because this is only the scattering equation for one electron, no density or temperature is appearing in the equation. In the next section the plasma or many electron case will be treated.

2.5.3 *Many electron Thomson scattering*

In a plasma there are many free electrons, but as seen in section 2.1 collective behaviour is defining a plasma, leading to two cases for Thomson scattering: coherent and incoherent Thomson scattering. The former meaning that nearby electrons have a constant phase difference that causes interference. The latter meaning that there is no constant phase difference and accordingly no interference. In case of coherent Thomson scattering, the radiation of the electron and the *holes* (absence of electrons) would nearly cancel. In the case of incoherent scattering, the scattered powers can be added, which introduces the electron density n_e and is the desired operational mode in many plasma experiments. To ensure that the scattering is indeed incoherent, a condition can be given for the scattering vector $\boldsymbol{k} = \boldsymbol{k_s} - \boldsymbol{k_i}$ and the Debye length λ_D:

$$\lambda_D k \gg 1 \tag{2.16}$$

For fusion plasmas and typical scattering geometries this condition is usually satisfied. This condition also means that the scattering wavelength $\frac{2\pi}{k}$ is small compared to the Debye length. The particles in the Debye sphere are taken to be randomly positioned in the Debye sphere. When there is a multitude of scattering wavelengths inside the Debye sphere, the randomly positioned particles phase can also be described as random. The other extreme of this would be that the scattering wavelength is large compared to the Debye length, and the particles in the Debye sphere would all have the same phase. This would be the coherent case.
Even with fixed Debye length and incident wavelength, the kind of Thomson scattering can be varied with the observation direction. This is because the scattering vector $\boldsymbol{k}$ depends on both incident and scattered wave vector. It can easily be seen that if $\boldsymbol{k_i}$ and $\boldsymbol{k_s}$ were equal, then only coherent Thomson scattering could be observed. Furthermore for fixed magnitudes of $\boldsymbol{k_i}$ an $\boldsymbol{k_s}$, it can be seen that $\boldsymbol{k}$ is smallest, when $\boldsymbol{k_i}$ and $\boldsymbol{k_s}$ are parallel and $\boldsymbol{k}$ is largest, when they are perpendicular.
For incoherent Thomson scattering the scattered power P_e of the single electrons is added. The scattered power per unit area A is given by Poynting's theorem:

$$\frac{P_e}{A} = \epsilon_0 c \left|\boldsymbol{E_s}\right|^2 \tag{2.17}$$

Using the distance R between the scattering electron and the observer, this can be expressed as scattering power per solid angle $\Omega_s = \frac{A}{R^2}$:

$$\frac{dP_e}{d\Omega_s} = \epsilon_0 c R^2 \left|\boldsymbol{E_s}\right|^2 \tag{2.18}$$

For multiple electrons N_e the incoherent sum gives:

$$\frac{dP}{d\Omega_s} = \epsilon_0 c R^2 N_e \left|\boldsymbol{E_s}\right|^2 \tag{2.19}$$

This equation can be expressed in terms of the electron density n_e, by including the scattering volume:

$$\frac{dP}{d\Omega_s dV} = \epsilon_0 c R^2 n_e \left|\boldsymbol{E_s}\right|^2 \tag{2.20}$$

This is where the density measurement originates from. In the classical limit, the scattered electromagnetic field becomes the classical dipole field:

$$E_s = \left[\frac{r_e}{R}\hat{\boldsymbol{s}} \times (\hat{\boldsymbol{s}} \times \boldsymbol{E_i})\right]'_t \tag{2.21}$$

Using this to calculate the classical scattering power gives:

$$\frac{dP}{d\Omega_s dV} = \epsilon_0 c r_e^2 \sin^2\theta n_e \left|\boldsymbol{E_i}\right|^2 \tag{2.22}$$

The angle θ between the polarization $\hat{e}$ and scattering direction $\hat{s}$ is used to resolve the vector product. The term $r_e^2 \sin^2\theta$ is the differential Thomson scattering cross section $\frac{d\sigma_T}{d\Omega_s}$. Integrating this over all solid angles ($\Omega_s = 2\pi \sin\theta$) gives the Thomson cross section:

$$\sigma_T = \frac{8\pi}{3} r_e^2 \approx 7 \times 10^{-29}\,\mathrm{m}^2 \tag{2.23}$$

This cross section can be understood as the effective size of an electron for the scattering process. Because the value is small, the scattered power will be orders of magnitude smaller than the input power. Additionally, only a small solid angle will be detected in the experiment, making the measured signal even smaller.

In this classical treatment the dependence on the electron density can be seen easily. The temperature dependence is based on the relativistic Doppler effect. Because the whole derivation of the relativistic scattering formula would go beyond the scope of this thesis, only the motivation and result will be given here and the differences to the classical equation will be pointed out.

The relativistic Doppler effect causes moving electrons to see a Doppler shifted incident frequency, resulting in a shifted emitted frequency. Combining the emissions of many electrons with different velocities leads to a Doppler broadened spectrum. The velocity distribution determines the spectrum. When thermal equilibrium can be assumed, the velocity distribution becomes the Maxwell-Boltzmann distribution, which is solely determined by the temperature. This broadening would also happen in a system with non-relativistic electron velocities, but the effect grows with higher temperatures. In the non-relativistic case the broadening can be described as a Gaussian with the centre frequency being the incident frequency.

With relativistic electron velocities however another effect has to be taken into account: the relativistic blue shift. Instead of a symmetric Doppler broadened Gaussian a spectrum with more intensity on the high energy side will be detected. The reason for that is the changing angular emission characteristic of a radiating dipole shown in figure 2.4. The typical $\sin^2\theta$ characteristic seen in equation 2.22 always stays the same in the rest frame of the electron. In the rest frame of the observer this characteristic undergoes a Lorentz transformation, which leads to a distortion of the characteristic. Instead of emitting most of the power in the direction perpendicular to the dipole motion, the maximum of the transformed characteristic leans towards the electron velocity direction. The higher the electron velocity, the more it will emit in its forward direction, leading to electrons moving towards the observer contributing more to the measured intensity than electrons moving away from the observer. Electrons moving towards the observer emit blue shifted radiation and electrons moving away red shifted radiation, hence the spectrum's lopsidedness towards the high energetic side.

In any case, the temperature dependent velocity distribution will lead to a scattered

spectrum which makes the temperature measurement possible. The fully relativistic formula for the scattered power per solid angle Ω_s and scattering frequency ω_s is given by:

$$\frac{d^2P}{d\Omega d\omega_s} = r_e^2 \int_V \langle \boldsymbol{S_i} \rangle d^3r \int \left| 1 - \frac{1 - \hat{\boldsymbol{s}} \cdot \hat{\boldsymbol{i}}}{(1-\beta_i)(1-\beta_s)} \beta_e^2 \right|^2 \left| \frac{1-\beta_i}{1-\beta_s} \right|^2 (1-\beta^2) f(\beta) \delta(\boldsymbol{k} \cdot \boldsymbol{v} - \omega) d^3\boldsymbol{v} \tag{2.24}$$

The integral of the mean incident Poynting vector $\langle \boldsymbol{S_i} \rangle$ is taken over the scattering volume V and is a measure for the mean incident power in the scattering volume. The velocity integral consists of five parts. The first absolute value is a value below or equal to one. It accounts for relativistic depolarisation effects. The second absolute value resolves to the frequency ratio $\frac{\omega_i}{\omega_s}^2$ if the delta function is evaluated. The third term $(1-\beta^2)$ can be seen as the reduction of the scattering cross section because of relativistic mass increase of the electron mass ($\sigma_T\ r_e = \frac{e^2}{4\pi\epsilon_0 m_e c^2}$). The fourth term $f(\beta)$ is the velocity distribution, taken to be the relativistic Maxwell-Boltzmann distribution. The last term is the delta distribution accounting for the Doppler effect, by allowing only velocities $\boldsymbol{v}$ whose Doppler shift corresponds to the scattering frequency $\omega = \omega_s - \omega_i$. Note that by taking the projection of the velocity onto the scattering vector $\boldsymbol{v} \cdot \boldsymbol{k}$, both, the relative motion of electron and source as well as electron and observer are taken into account.
The velocity integral can usually not be solved analytically. To simplify the notation, the whole integral is named the spectral density function $S(\epsilon, \theta, \alpha)$. This function should behave similarly for a wide range of incident wavelengths and electron temperatures. For that reason, normalised quantities are used as parameters. Instead of a specific frequency, the normalised wavelength shift $\epsilon = \frac{\lambda_s - \lambda_i}{\lambda_i}$ is used. The scattering angle θ is used implicitly in all of the vector projections. Instead of the temperature (which defines the velocity distribution), the normalised inverse temperature $\alpha = \frac{m_e c^2}{2T_e}$ is used as a parameter. With these changes in parametrisation, equation 2.24 can be written in a compact form:

$$\frac{d^2P}{d\Omega d\epsilon} = r_e^2 \int_V \langle \boldsymbol{S_i} \rangle d^3r S(\epsilon, \theta, 2\alpha) \tag{2.25}$$

This equation is not analytically solvable, but before discussing the approximations and equations used for the evaluation of the Thomson scattering data at W7-X in section 2.5.5, a short summary of the measurement setup will be given to introduce the components that have to be included in the analysis.

2.5.4 *Interlude: Measurement setup at W7-X*

In this section an overview of the Thomson scattering system at W7-X will be given for the recent operational period (OP1.2b). Only the parts most important to this thesis will be highlighted and a more detailed description of the diagnostic can be found in the appendix section A, ([21], [24]).
In general, one measurement is conducted by guiding a laser pulse into the plasma and observing the Thomson scattered light with polychromators. The scattered intensity gives information about the electron density and the spectrum about the electron temperature. The measurement at different locations in the plasma gives spatial information, enabling

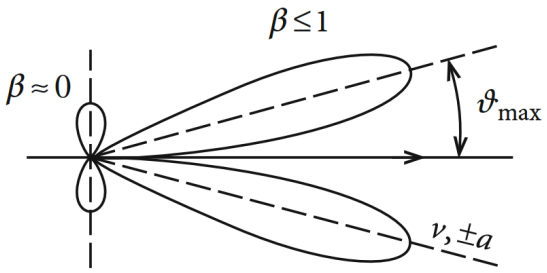

Figure 2.4: Angular scattering distribution of dipole radiation for non-relativistic ($\beta \approx 0$) and relativistic particle velocities ($\beta < 1$). It can be seen that a dipole moving with non-relativistic velocity emits most of its power perpendicular to the dipole motion. A dipole with relativistic speed however, emits more power in the velocity direction. The higher the velocity, the closer the maximum of the distribution gets to the velocity direction. Taken from [26, p. 428].

the analysis of electron density and temperature profiles. The measurement setup is shown in figure 2.5 and will be discussed briefly in the following.
High energy infrared laser pulses are generated with a frequency of 30 Hz by three alternately firing Nd:YAG lasers. They are guided by a mirror system into the plasma vessel (cut through the vessel shown in brown and yellow in figure 2.5) where the plasma electrons scatter a fraction of the pulse and the rest is dumped outside of the vessel to reduce stray light. The scattered light is collected by a set of lenses and glass fibre bundles looking at different plasma positions (giving the spatial information – sight lines shown in red in figure 2.5). It is then analysed by polychromators, which consist of five consecutive bandpass filters (giving the spectral information), each equipped with an avalanche photodiode measuring the respective intensity. Further on, the plasma positions analysed will be called scattering volumes and the five filters with diodes will be called spectral channels.
The adaptation of the theoretical Thomson equations to this measurement setup will be shown in the next section.

2.5.5 *Analysis principles at W7-X*

An analytically solvable approximation of the spectral density function from equation 2.25 is given by Naito et. al. [25]. This approximation is used at W7-X to evaluate the scattering data. Comparing the approximated formula with numerical solutions showed that the approximation gives reliable (less than 0.1 % deviation) results for electron temperatures below 100 keV. Thus, there should be no problem in using this at W7-X where the Thomson system is only designed to give reliable results up to 10 keV.
The formula representing the actual measurement is taken from Bozhenkov et. al. [24]. Due to the already addressed low scattering signal, highly resolved scattering spectra cannot be obtained. Instead, the aforementioned five bandpass filters are being used, meaning that the spectrum only consists of five points which result from (spectral) integration over each of the filter's transmission characteristic. The measured quantity is

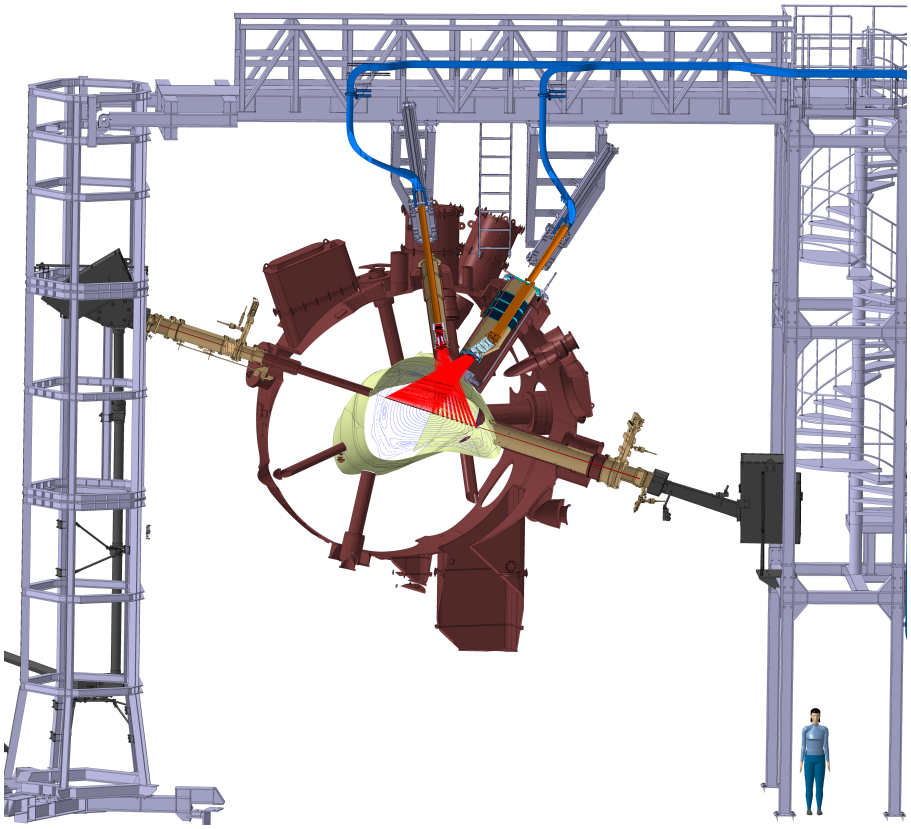

Figure 2.5: Overview of the Thomson diagnostic at W7-X. The laser beams are guided from the bottom left through black tubes into the inner tower of W7-X. There the entrance mirror box guides the beam through the vessel. From above two sets of collection optics gather the Thomson scattered light. Each of the red lines represents the sight line of a glass fibre bundle, showing the spatial resolution of the diagnostic. After passing through the vessel, the beams are absorbed in a beam dump located in the exit mirror box. The holding structure is called the Thomson bridge. It is mechanically decoupled from W7-X to reduce vibrations of the diagnostics components.

then the signal s in the spectral channel i integrated over the pulse duration T and can be approximated by:

$$\left(\int_T s dt\right)_i = n_e \int_T P_i dt \frac{r_e^2}{hc} \delta\Omega g_0 \int\int S(\epsilon, \theta, \alpha) \frac{\lambda_s}{\lambda_i} \frac{g_i(\lambda_s)}{g_0} dL d\lambda_s \tag{2.26}$$

Where $\int_T P_i dt$ is the pulse energy, $\delta\Omega$ is the solid angle covered by the collection optics, $g_i(\lambda_s)$ is the absolute spectral sensitivity function of spectral channel i (including all optical components), g_0 is a reference sensitivity value at a specific wavelength and the integral goes over the length of the scattering volume L and scattered wavelength λ_s. The scattering volume is determined by the overlap of volume seen by the collection optics and the laser beam volume. If the scattering volume is small enough, the plasma parameters can be assumed to be constant and the integration over L becomes a multiplication with the volume length δL. Since there are setup specific parameters: $\delta\Omega g_i(\lambda)\delta L$ a calibration of the system is required. The calibration is split into a relative (spectral) calibration $\frac{g_i(\lambda_s)}{g_0}$ and a separate measurement for the absolute calibration $\delta\Omega\delta L g_0$. The

calibration measurements conducted at W7-X are described in detail in sections 3.3.1 and 3.3.2.

2.6 BAYESIAN ANALYSIS

2.6.1 *Overview*

To evaluate the measured Thomson scattering data, Bayesian statistics is used. This chapter will give an overview on Bayesian statistics, the implementation of this kind of statistics in a model for Thomson scattering and descriptions of tools used to evaluate the data. The following overview on Bayesian statistics is mainly based on 'Data Analysis' by D.S. Sivia [27]. In contrast to *common* statistics, the interpretation of probabilities is different. The common interpretation of a probability is that it denotes the relative frequency of possible outcomes, when an experiment is repeated an infinite number of times. In the Bayesian view, probabilities represent a degree of belief. The basis of Bayesian statistics is Bayes' theorem:

$$p(X|Y,I) = \frac{p(Y|X,I)p(X|I)}{p(Y|I)} \tag{2.27}$$

with X and Y being events, and I background information. The vertical line inside the brackets denotes a conditional probability. For example $p(X|Y,I)$ means: the probability of event X, given that event Y and background information I are true. Bayes' theorem is a direct consequence of the product rule for probabilities:

$$p(X,Y|I) = p(X|Y,I)p(Y|I) \tag{2.28}$$

which states that the probability of X and Y being true is equal to the probability of X given Y multiplied with the possibility of Y being true. Logic dictates that $p(X,Y|I)$ has to be the same as $p(Y,X|I)$. The product rule then becomes:

$$p(X,Y|I) = p(X|Y,I)p(Y|I) = p(Y|X,I)p(X|I) = p(Y,X|I) \tag{2.29}$$

The middle part is basically Bayes' theorem. For practical purposes, the theorem is usually presented in the form of equation 2.27. The left-hand side $p(X|Y,I)$ is called the posterior and the right-hand side consists of the prior $p(X|I)$, the likelihood $p(Y|X,I)$ and the evidence $p(Y|I)$. These terms give an intuitive explanation for Bayes' theorem. The prior $p(X|I)$ denotes the degree of belief of X being true, given the current knowledge I. X could stand for a hypothesis e.g. on how large the electron density n_e is in W7-X. If additional information Y is obtained, the degree of belief of X being true is given by the posterior $p(X|Y,I)$. Bayes' theorem then states that the posterior degree of belief consists of the product of the prior degree of belief and the likelihood $p(Y|X,I)$ of the new data. This is the mathematical formulation of gaining knowledge and gives a measure on how new information effects a given hypothesis. Please note that the product of likelihood and prior only equals the posterior if normalised by the evidence $p(Y|I)$. Because the evidence is a constant and not dependent on the hypothesis X it is often omitted in data analysis. To better distinguish, the product of likelihood and prior is often called *joint probability*. There are cases were the evidence cannot be omitted, e.g. to compare different models on the same data.

Because Bayes' theorem incorporates the process of learning, it is often used as a basis for machine learning. It can also be used for data analysis. Why it is convenient to do a Bayesian data analysis will be discussed in the following. In the Bayesian view measured data is always correct. Imperfect is only the knowledge of the measurement. The degree of belief one has in the parameters of the measurement influences the degree of belief one has in the hypothesis. The degree of belief one has in the parameters usually enters the equation through the prior. Parameters that influence the analysis, but are not of particular interest, are called nuisance parameters. These parameters enter the model, influence the outcome, but do not appear as results of the analysis.
It is important to note that there is no inherent difference in how statistical or systematic errors enter a Bayesian analysis, while the errors might still be modelled differently. Therefore, it is a convenient method to include systematic errors in a consistent manner into the analysis. Because of this consistent inclusion of errors, Bayesian analysis makes it possible to combine data from different diagnostics. Usually, it is not trivial to calculate a combined result for two different diagnostics measuring the same quantity. In the Bayesian way it makes no difference, if the new data Y is acquired with a different diagnostic, because all information about the new measurement is transcribed in the likelihood and evidence. The final result of a Bayesian analysis is the posterior. It is a probability density function (pdf) containing the information of all measurements and uncertainties. Usually the values of interest are the most likely value and the standard deviation. This however implies a Gaussian distribution. The posterior pdf is not limited to a Gaussian one. It can be asymmetrical or multimodal (more than one extreme value). This gives the possibility to calculate asymmetric error bars, representing the pdf in a reduced way, or to consider the whole/unreduced pdf. Because of the possibility of combining different diagnostics, a Bayesian analysis of the W7-X data seems a very useful approach. How this abstract concept of Bayesian analysis is implemented at W7-X will be discussed in the next section.

2.6.2 *Bayesian models*

Because of the aforementioned reasons, multiple diagnostics at W7-X use Bayesian data analysis. To accomplish these analyses, a computational model of each diagnostic is built. The purpose of such a model is to represent every aspect of the measurement in question and to connect those to the evaluation routines. A 'perfect' model would be able to reproduce the measured data, by giving it the same input parameters that were influencing the measurement at the time. As the problem is that not all input parameters are usually known because of e.g. measurement uncertainties, the model calculates the probabilities of data given the known uncertainties in a Bayesian way.
The framework in which the models are built at W7-X is called Minerva. As the general description given in this section might not be easy to understand, a simple example of a Bayesian model in Minerva will be given in the next section. This model will show how applying a linear fit in Minerva could be realised. It is particularly important to understand how these models work because in this thesis the existing model for the Thomson scattering diagnostic was altered to include systematic errors.

2.6.3 *Linear fit Bayesian model in Minerva*

In the previous section the abstract concept of Bayesian data analysis was introduced. To apply Bayesian statistics to data sets, an existing framework called *Minerva* is used. This framework gives the means to build a model representing the measurement and then to evaluate the measured data with this model. Before describing the complex Thomson model, in this section a simple model for the task of applying a linear fit in a Bayesian way is presented.
The models built in Minerva are forward models. Forward modelling is the concept of taking the desired quantities as input parameters and the actual measurement as the result. This is befitting the Bayesian way because of the aforementioned belief that measured data is always correct. In case of the simple task of applying a linear fit in the form of $f(x) = a \cdot x$ (a being the slope), the desired quantity would be a and the measurement would be a set of data points $\{x_i, y_i\}$. In a forward model a would be guessed and compared to the data $\{x_i, y_i\}$ multiple times. The a giving the best agreement with the data $\{x_i, y_i\}$ is the desired outcome. The model representing this simple task will be discussed in the following.
A simplified scheme of the model can be seen in figure 2.6. Each box in the scheme is called a *node*. Blue nodes mark parameters of the model and a grey node marks the observation node *obs*. The measurement is denoted by *values* and consists of a set of measurement points $\{x_i, y_i\}$, which are given to the *obs* node. The slope a is the parameter in question and is represented by the blue node a. The node x consists of the points $\{x_i\}$ were the fit function needs to be evaluated. The arrows from a and x show that both parameters are handed over to the *pred* node. This node makes the prediction, meaning $\text{pred}_i = a \cdot x_i$. These predicted values are handed over to the *obs* node, where they are compared to the measurement (values node). According to the prior of a and the likelihood of the data, the probability of a being correct, given the data, is calculated. This gives the means of finding the slope a with the highest agreement with the data, by finding the a with the highest (joined) probability.
As can be seen by this example, the graph only presents the variables and their connections, while specifying the roles of the variables by colour coding. Still, it is a useful tool to visualise a complex model. In this simple example, the connections are enough to understand the model. If a and x are set, the prediction $a \cdot x$ is calculated. This prediction is assigned an uncertainty (e.g. Gaussian pdf with a certain covariance) by which means it can be compared to the measurement (*values*), which is taken to be exact. The uncertainty assigned to the prediction should represent the degree of belief one has for the measurement. If for example the relative error of the measurement instrument is $\pm 5\,\%$, a multivariate Gaussian with dimensionality i and standard deviation of $0.05 \cdot a \cdot x_i$ would represent the prediction. The model can also take prior knowledge of a into account. If for example, a were a velocity (and x time), than the most conservative (and naive) prior would be a uniform pdf from $0\,\mathrm{m\,s^{-1}}$ to $3 \times 10^8\,\mathrm{m\,s^{-1}}$. This would be the same as stating that the velocity is positive and smaller than the speed of light. A naive prior like this leaves a large parameter space to be sampled from. To reduce computational time, a more sensible prior should be used. If it were known that the moving object in question has a maximum velocity of $10\,\mathrm{m\,s^{-1}}$, a uniform distribution from $0\,\mathrm{m\,s^{-1}}$ to $10\,\mathrm{m\,s^{-1}}$ should be set. As long as the prior does not exclude valid parameters, the final result will be the same, but the computational time to acquire the result may vary.

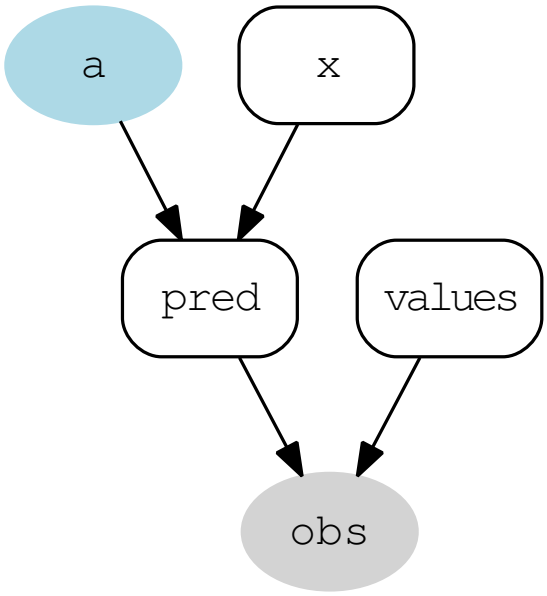

Figure 2.6: Simplified scheme of a linear fit model in Minerva. This graph represents the quantities and connections of the model with boxes called *nodes*. The parameter *a* of the model is represented by a blue node. The linear fit function is evaluated in the prediction node *pred* at the points given by the *x* node. The observation node *obs*, which compares the measurement (*values* node) to the prediction, is coloured in grey.

In the next section an overview of the model representing the Thomson measurement will be given.

2.6.4 *Thomson model in Minerva*

The Thomson model in Minerva is a forward model. This means that instead of calculating the results from measured data, this model uses the expected results to calculate the measured data. In this thesis, the measured data are photon counts and the results are the electron density n_e and temperature T_e. They are obtained by using different n_e and T_e values and calculating the ones with the highest probability in a Bayesian way. A simplified graph of the model, similar to the one shown in the previous section (see figure 2.6), can be seen in figure 2.7. Each box represents a node of the model and the arrows show the connections between the nodes. The parameters of the model are marked in blue and the observations (measured data) are marked in grey. From top to bottom, the model starts with the nanosecond at which the measurement is being evaluated. This nanosecond is given to two data sources *ds* and *vmecIdDS*. A data source loads the requested data and all necessary information. The *vmecIdDS* is a data source for finding the magnetic configuration of W7-X at the requested nanosecond, which is not needed for this thesis. In principle this magnetic configuration then determines the magnetic flux surface belonging to a given scattering volume. Then the electron density n_e and temperature T_e can be mapped to the flux surfaces making it possible to compare the data to diagnostics located at other positions of W7-X.
The data source marked *ds* is the Thomson data source. It loads the raw scattering data from the W7-X archive. The raw data is preprocessed and given to the observations node,

which represents the measurement. The data source also loads relevant background information like the positions of the scattering volumes in the vessel, the dimensions of the scattering volumes, positions of the collection optics, which laser was operating, laser energy, laser direction, spectral and absolute calibrations, and so on. The data collected by the data source is then distributed to the corresponding nodes. Most of the information enters the *thomsonModel* node which contains the calculation of the scattered signal via equation 2.26.

Similar to the slope a in the linear fit model, the two main parameters for this calculation, n_e and t_e, are not provided by the data source but by the two separate boxes marked *ne* and *Te*. These two boxes mark the prior pdf of n_e and T_e of the Thomson model. In this case a uniform prior between $n_{e_{low}}$ and $n_{e_{high}}$ is chosen for n_e. The same holds for T_e. The uniform prior implies no knowledge of the quantity, except for the upper and lower boundary. The range for n_e was chosen to be between $1 \times 10^{15}\,\mathrm{m}^{-3}$ to $2 \times 10^{20}\,\mathrm{m}^{-3}$. The range for T_e was chosen to be between $1 \times 10^{-4}\,\mathrm{keV}$ to $20\,\mathrm{keV}$. The lower limits being well below the measurable limits of the Thomson diagnostic and the upper limits being approximate W7-X limits. The typical densities at the plasma core at W7-X are of the order of $5 \times 10^{19}\,\mathrm{m}^{-3}$ and typical temperatures of the order of $1\,\mathrm{keV}$. Both are well within the chosen intervals.

Back in the model the high and low limits determine the uniform distributions for n_e and T_e, which are marked by the nodes *values*. At both nodes a random value is drawn out of the respective distributions. This drawing of samples is done for each scattering volume individually. The random samples for each scattering volume are saved in a vector named *ne1d* or *te1d* respectively. Those are mapped to the magnetic flux surfaces in *ne3d* or *te3d* for future applications of the model.

The random samples of n_e and T_e are put into the node called *thomsonModel*. There, based on all the information given by the data source and with the random samples, the prediction of the photons generated by Thomson scattering and the fraction of these photons detected is calculated. This prediction is done for all the scattering volumes, including the individual sensitivity measurements (calibrations) and given to the *pred* node. The predictions of the number of measured photons are then given to the observation *obs* node for comparing to the measurement.

The *thomsonModel* node is also providing the photon covariance, meaning the Poisson noise of the calculated scattered photons. This covariance is added to the covariance due to electronic noise and to the covariance due to preprocessing the raw data. As a side note, the covariance is the matrix equivalent of the variance, but for higher dimensional Gaussian distributions.

The covariances give the means to compare the measurement with the prediction. For that, a Gaussian pdf with the total covariance and the prediction as a mean is used in the model. The Gaussian is not used to represent the observation because in a Bayesian point of view, measured data is always correct, only the knowledge about the measurement is imperfect.

There are two main ways of sampling the parameter space (n_e and T_e). If the dimensionality is low the parameter space can be iterated over all possible parameter combinations with the desired resolution. For example, if the desired quantities are n_e and T_e, and it is known that they were in a range of $1 \times 10^{19}\,\mathrm{m}^{-3}$ to $1 \times 10^{20}\,\mathrm{m}^{-3}$ and $0\,\mathrm{keV}$ to $10\,\mathrm{keV}$, and a resolution of $0.01\,\mathrm{m}^{-3}$ or $0.01\,\mathrm{keV}$ is wanted, a grid of 1000×1000 values would have to be evaluated. It can easily be seen that this can only be done when the dimensionality

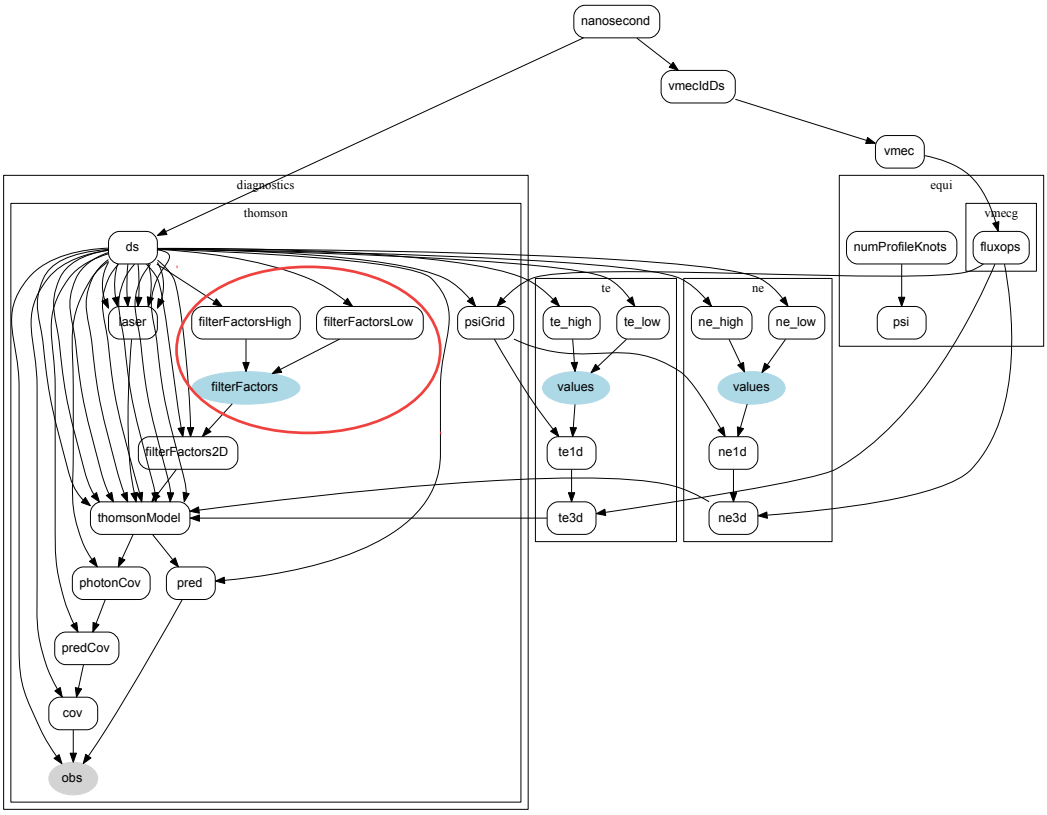

Figure 2.7: Simplified scheme of the Thomson model in Minerva. As in the linear fit model shown in figure 2.6 all quantities and connections of the model are shown. The two main parameters n_e and T_e are represented by the blue *values* nodes and the observation, meaning measured intensity, is represented by the grey observation (*obs*) node. The highlighted (red) part of the model was added in this thesis to represent spectral calibration errors and will be described in section 4.2.

$N_{dimensions}$ is low, because it follows a power law: $N_{iterations} = N_{gridpoints}^{N_{dimensions}}$ (assuming the desired number of grid points were the same for every dimension). This is also known as the *curse of dimensionality*. The other way of obtaining the parameter space is by guessing the parameters. If not for ingenious algorithms this would take a long time. The crux to efficient guessing is that the parameter space where the pdf is low is not of particular interest in most cases. Thus there are algorithms which make sure to get into a parameter space with a high pdf and then sample that parameter space until the wanted resolution is reached. The method that is used in the Thomson model to get into a space with high pdf is called a maximum a posteriori algorithm (Hooke and Jeeves [28]) and the method to sample that space is called Markov Chain Monte Carlo.
In the next section a brief overview on the Markov Chain Monte Carlo method and a popular Markov Chain Monte Carlo algorithm (Metropolis-Hastings) will be given.

2.6.5 *Markov Chain Monte Carlo*

One way of sampling a multidimensional parameter space is the Markov Chain Monte Carlo method. It combines the concept of a Markov Chain with the Monte Carlo method. A Markov Chain is a stochastic process, which consists of a series of steps, where each step is solely depending on the present state. In other words, it is a process without a memory. A simple example can be given by the drawing of black and white marbles out of a bag. Every step in the process is one drawing. Based on what kind of marble was drawn, the question could be how likely it is to draw a white marble next. If the current marble were to be put back into the bag before drawing again, the answer would only depend on the current state of the process. Thus this would be a Markov Chain. If each drawn marble would be removed from the bag, the probability of drawing a white marble next depends on past drawings. Consequently, this would be no Markov Chain. The Monte Carlo method is a well established numerical procedure to solve problems that are not or only with high effort analytically solvable. The main characteristic of a Monte Carlo method is that the samples at which the function in question is evaluated are drawn randomly. The drawing is repeated until the wanted resolution is reached. During that the probability distribution, from which the samples are drawn, stays the same. A simple example of how the Monte Carlo method works can be given by the integration of a circle: The area of a circle with radius r is parametrised by $x^2 + y^2 \leq r^2$. Assume it were not possible to solve the surface integral $A = \int_{x^2+y^2\leq r^2} dA$ to obtain the surface area A. The Monte Carlo way of solving this problem would be drawing a value x_i and y_i from e.g. a uniform distribution between $-r$ and r respectively. Afterwards the function is evaluated at the sample: $x_i^2 + y_i^2 = r_i^2$. Then the parametrisation is checked: $r_i^2 \leq r^2$. If the statement is true then the sample is inside the circle. This procedure is repeated and the number of samples, where the statement returned true, N_{true}, as well as the total number of samples N is saved. The solution A_{MC} then becomes $A_{MC} = \frac{N_{true}}{N} \cdot r^2$. This can be understood as follows: Drawing x and y from uniforms between $-r$ and r means drawing random samples of a square with area $4r^2$. The check then resolves to the question, if the random point in the square is also inside a circle with radius r and the same centre as the square. The fraction $\frac{N_{true}}{N}$ measures the possibility of finding a point that is in the square as well as in the circle. By multiplying that possibility with the area of the square gives the area of the circle. The measurement of the possibility will only be equal to the actual possibility, in the limit of an infinite sample size. This means that like every numerical solution, the result is an approximation.
The same result could have been obtained, if one would have iterated x and y with a step size befitting the wanted resolution. The number of samples would be less or equal to the number of samples needed to obtain the same resolution of the parameter space with the Monte Carlo method. Consequently, no one would use a Monte Carlo method for that problem. For higher dimensional problems however, Monte Carlo methods become more attractive. Still, to improve efficiency, a means of sampling the 'interesting' parts of the parameter space is needed. The Markov Chain Monte Carlo method provides such a possibility.

In this thesis the Markov Chain Monte Carlo method is used to approximate a high dimensional Bayesian joined pdf for which no analytical solution can be obtained. This numerical solution should give a *good* representation of the pdf within the given un-

certainty. This means that with an infinite amount of samples, the sample distribution should be equal to the pdf in question, but even with a finite amount of samples, the parts of the pdf that are highly contributing should be well represented. Taking the integral of the pdf as a measure of good representation, the parts of the pdf with a high contribution to the integral should be sampled with a high resolution and the low contributing parts should be sampled only with a low resolution. How this is done with the Markov Chain Monte Carlo (MCMC) method will be discussed in the following by the means of the Metropolis-Hastings [29, 30] algorithm, which is a widely used realisation of an MCMC.
The Metropolis-Hastings algorithm is an iterative process. Each iteration i ends in the saving of a sample s_i. In the following, a short summary of one iteration and afterwards a more detailed description of the iteration will be given.

- step 0: iteration i resulted in sample s_i
- step 1: a candidate for the $i+1$'th iteration is drawn s^c_{i+1}
- step 2: acceptance ratio α is calculated
- step 3:
  a) candidate is not accepted: $s_{i+1} = s_i$
  b) candidate is accepted: $s_{i+1} = s^c_{i+1}$
- step 4: iteration $i+1$ resulted in sample s_{i+1}

Assume iteration i is done and sample s_i is saved (step 0). The sample consists of a set of parameters $\{X_j\}_i$. The goal of iteration $i+1$ then is to save a sample s_{i+1} (step 4). How this sample is acquired will be described in the following.
A candidate for the next sample s^c_{i+1}, meaning a set of parameters $\{X_j\}^c_{i+1}$, is drawn from the so-called *proposal distribution* (step 1). This proposal distribution could for example be a multivariate Gaussian with the last set of parameters $\{X_j\}_i$ as mean.
Next it will be decided, whether the candidate for the next sample $\{X_j\}^c_{i+1}$ should be kept or not. This is done by comparing the Bayesian probability of the i'th step $p(\{X_j\}_i)$ and the candidate for the $i+1$'th step $p(\{X_j\}^c_{i+1})$. The Bayesian probability is calculated based on a model like e.g. the linear fit model of section 2.6.3. In that example the Bayesian probability would be the result of multiplying the prior probability of the guessed a (assigned on prior knowledge — e.g. uniform distribution with a being positive) with the likelihood of the prediction $a \cdot x$ (assigned on measurement error – e.g. Gaussian distribution with measurement as mean and statistical measurement error as standard deviation).
For an easy comparison of the Bayesian probability of a sample and a candidate, the so-called *acceptance ratio* $\alpha = \frac{p(\{X_j\}^c_{i+1})}{p(\{X_j\}_i)}$ is calculated (step 2). In figure 2.8 the process is illustrated with two exemplary candidates and a simplified representation of a probability density function p (red) standing for the posterior pdf in question. The acceptance ratio α determines the probability of the *keeping* of the candidate, which can be described as:

$$\alpha = \begin{cases} 1 & \text{for } \alpha \geq 1 \\ \alpha & \text{else} \end{cases} \tag{2.30}$$

For candidate 1 in the figure, α is 1, meaning it would always be kept and for candidate 2 it is 0.8, leaving an 80 % chance for keeping. The keeping is determined by drawing a random number d_{random} from a uniform pdf between zero and 1 (step 3).
If $d_{\text{random}} > \alpha$ the candidate $\{X_j\}^c_{i+1}$ is disregarded, $\{X_j\}_i$ is saved as the next sample $s_{i+1} = \{X_j\}_i = \{X_j\}_{i+1}$ (step 3a) and the next iteration $i+2$ is started by drawing a new candidate from the proposal distribution.
If $d_{\text{random}} < \alpha$ the candidate is accepted and saved $s_{i+1} = \{X_j\}^c_{i+1} = \{X_j\}_{i+1}$ (step 3b).
Now the process is repeated for iteration $i+2$, with the difference that the proposal distribution is now centred around the accepted candidate $\{X_j\}_{i+1}$ (step 4 of iteration $i+1$ becomes step 0 of iteration $i+2$).
Note that a candidate is always accepted ($\alpha = 1$) if the probability is higher than before as is shown in the figure for candidate 1. This leads to the wanted efficient way of sampling because the MCMC is effectively moving towards parts of the parameter space with a higher contribution.
However, also allowing jumps into regions with less contribution ensures that the MCMC does not get stuck in a local maximum (given that the number of iterations is large enough). More precisely the amount of time the random walk spends in a parameter region is directly proportional to the pdf.

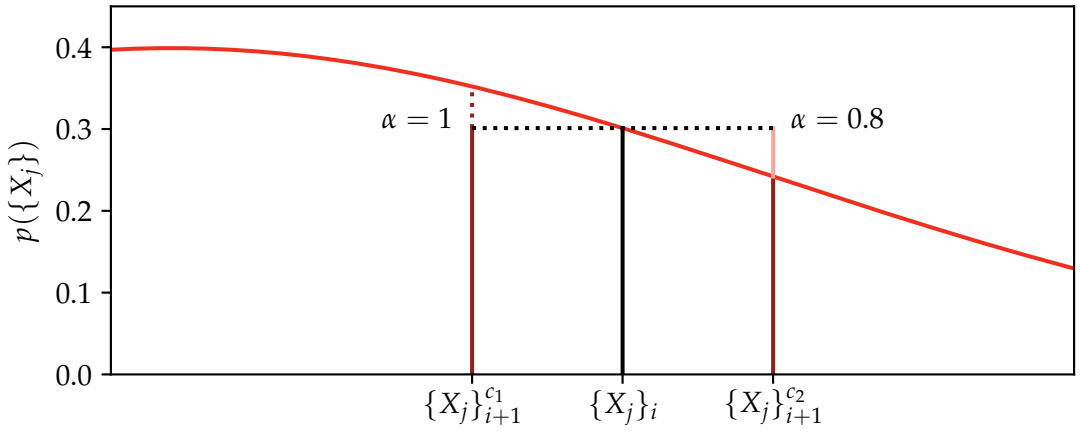

Figure 2.8: Representation of the acceptance probability of an MCMC step. The probability density function p is shown in a one-dimensional representation and the position of the i'th sample $\{X_j\}_i$ is marked with a black line. Starting from there, two candidates for the $i+1$'th step are shown: $\{X_j\}^{c_1}_{i+1}$ and $\{X_j\}^{c_2}_{i+1}$. The possibility of the acceptance is denoted be the acceptance ratio α. Candidate number 1: $\{X_j\}^{c_1}_{i+1}$ would always be accepted because the evaluation of the pdf $p(\{X_j\}^{c_1}_{i+1})$ is larger than the probability of the i'th step $p(\{X_j\}_i)$. Candidate number 2: $\{X_j\}^{c_2}_{i+1}$ has an 80 % chance of acceptance, which is the ratio of the two probabilities $\alpha = \frac{\{X_j\}^{c_1}_{i+1}}{\{X_j\}_i}$.

The method is called Markov Chain Monte Carlo because it combines the random sampling of the aforementioned Monte Carlo method with steps that form a Markov Chain. That the steps indeed satisfy the requirements for a Markov Chain can now be seen easily for the Metropolis-Hastings algorithm with a Gaussian with fixed standard deviations as proposal distribution: the proposal distribution and the acceptance ratio only depend on the current state and the candidate. It does not matter how the current

state is reached, because no history is being saved in the proposal distribution.
The final result of an MCMC analysis are samples representing the distribution in question. How many samples are needed to represent the distribution depends on the wanted resolution, the initial guess and the proposal distribution. Why the initial guess influences the needed number of iterations, can be seen with the example of a very localised distribution, which is to be sampled. If the starting point is in a region of the parameter space far off the localised maximum, a step away from the maximum might not have a much lower acceptance ratio than a step towards the maximum. This leads to the MCMC needing a large number of iterations to get into the parameter space with the localised maximum. This is why methods like *Hooke and Jeeves* [28] are used to find at least a local maximum before starting the MCMC analysis.
Some effort has to be put in finding the most efficient proposal distribution because if the distribution is too narrow, it will take many iterations to move significantly in the parameter space. If the proposal distribution is too broad, the chain might change the parameters too drastically to find the regions of high contribution. If one had an infinite amount of iterations, this would not be a problem, but in reality an infinite amount of computational time to solve a problem is not feasible.
In this thesis an Adaptive Metropolis-Hastings algorithm was used to find a time efficient proposal distribution. This adaptive method uses the history of the chain to optimise the width of the proposal distribution. Strictly speaking this contradicts the Markov Chain principle. However, if the adaption of the proposal distribution is small enough, it can be shown that the adaptive method has the desired properties [31].
After giving a general description of the iterative process of the MCMC, one example iteration through the Thomson model will be given in the next section.

2.6.6 *Example iteration*

In the previous two sections, the Thomson model and the sampling algorithm MCMC were described. In this chapter an example iteration through the model for one laser pulse and one example volume will be given. First the data source loads all the necessary information at the given timepoint. This includes the raw signals of the five spectral channels, which are shown as red dots in figure 2.9. The raw signal is the diode signal, i.e. photon counts over time (in ns). Because of the aforementioned use of one polychromator for multiple scattering volumes, there are correspondingly many signal peaks in the graphs, which have to be sorted to the corresponding scattering volumes, according to the time delay.
In the Thomson model, the raw data is preprocessed. The raw signal is fitted by a Gaussian (temporal laser pulse shape) convolved with a low pass filter (the amplifier applies a low pass filter on the signal). The fitting is done in a Bayesian way by making the parametrisation of the low pass Gaussian the free parameters of a model and using the raw data as the observation. From an MCMC the parameters representing the mean of the posterior pdf and their covariance are calculated. The low pass Gaussian resulting from this process is shown in dark red in figures 2.9.

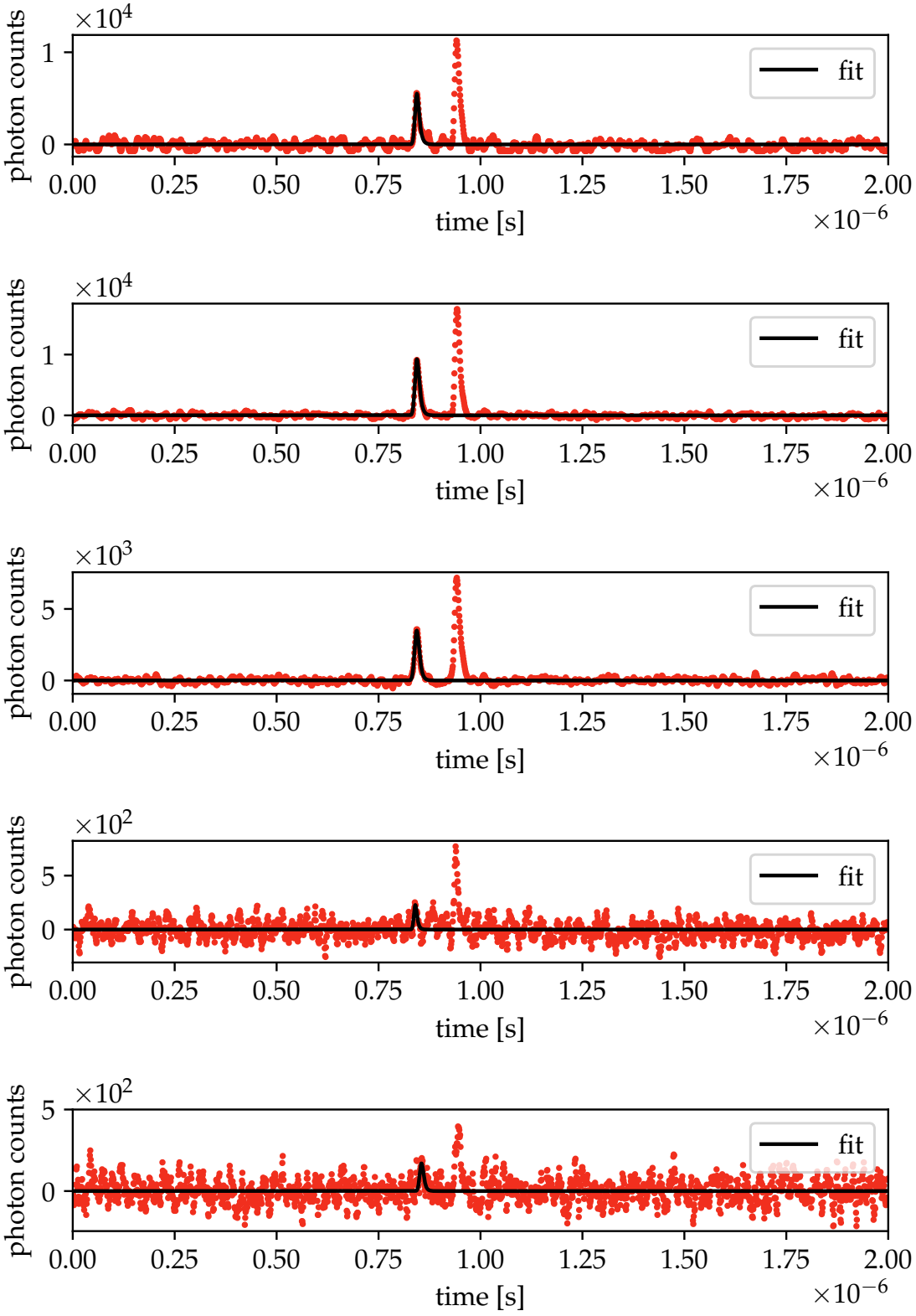

Figure 2.9: Raw signal for one volume. Shown are the time traces of the scattering signals from one polychromator for each spectral channel (one to five from top to bottom). The first signal peak in each graph belongs to the first scattering volume and the second peak belongs to another volume, analysed with the same polychromator. The applied fit with a Gaussian low pass function is shown in dark red. The integral of the fit function gives the total amount of photons detected in a given volume and spectral channel.

One of the parameters calculated is the integral of the low pass Gaussian and its covariance, which are used in the further analysis as the preprocessed scattering data, i.e. five points of measurement (for every scattering volume) denoting the integral over the laser pulse (time integral) and the integral over the sensitivity of the corresponding spectral channel (including amongst others filter transmission and sensitivity of the electronics).
When n_e and T_e are guessed, they are inserted in the scattering formula 2.26. More precisely, T_e enters the spectral density function S, which is approximated by the Naito formula [25]. The resulting scattering spectrum is shown in figure 2.10. To simulate the measurement, this ideal spectrum has to be multiplied by the spectral and absolute calibration. The spectral calibrations for each channel are shown in 2.11. Because the preprocessed signal is integrated spectrally (via bandpass filters), the five resulting multiplied spectra are also integrated. Multiplying each of the integrated values with the absolute calibration factor gives the predicted measurement. In figure 2.12 the predicted values for each channel (dark red dots) are compared to the measurement (red crosses). It can be seen that the prediction is close to the observation. Hence the guessed n_e and T_e should be close to the actual n_e and T_e during the measurement. The acceptance ratio of the MCMC is determined by the joint probability (covariance of the prediction and prior probability) of the guessed n_e and T_e. The steps described in this section are performed in every iteration of the model.

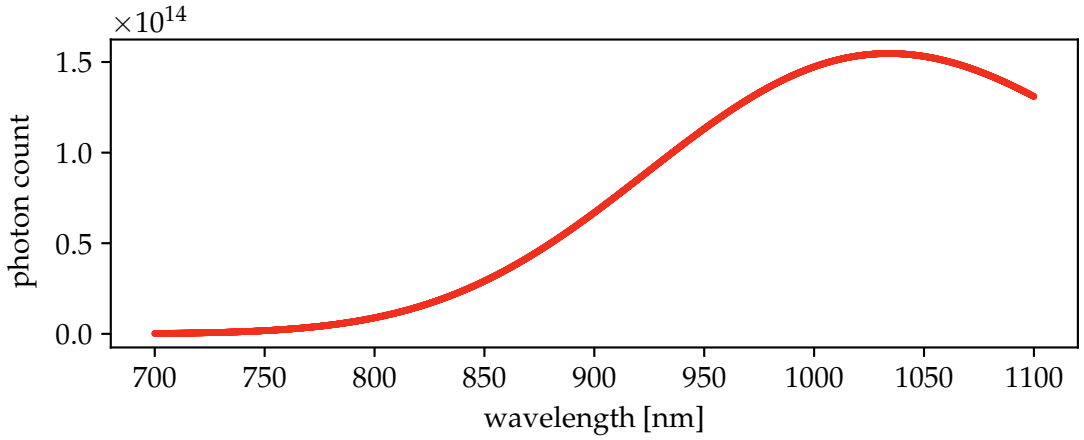

Figure 2.10: Theoretical scattering spectrum for one MCMC step with $n_e = 4.1 \times 10^{19}\,\mathrm{m}^{-3}$ and $T_e = 2.53\,\mathrm{keV}$.

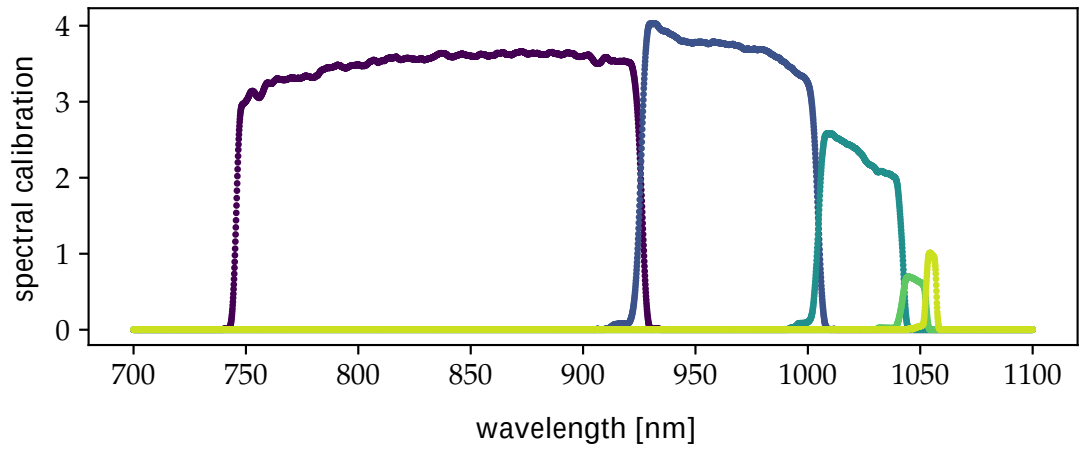

Figure 2.11: Normalised spectral calibration for one volume. Each spectral channel is marked by a different colour. These calibrations consist of all optical and electronic sensitivities contributing to the measurement in the respective channel. For better comparison all the calibrations are normalised to the same wavelength.

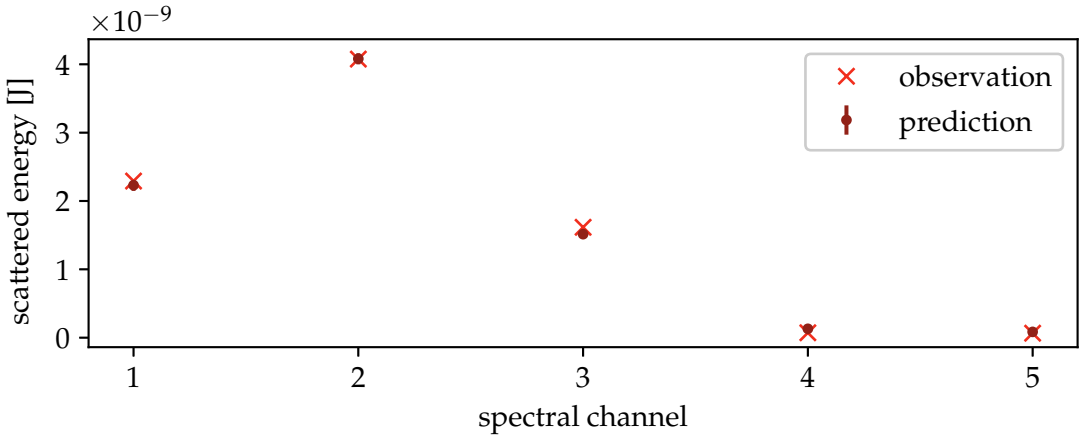

Figure 2.12: Scattered energy for one volume. Marked with a red cross is the observation, i.e. the Thomson measurement. Marked with a dark red dot is the prediction of the Thomson model for one MCMC iteration. The prediction is the result of multiplying the theoretical spectrum (see fig. 2.10) with the spectral calibration (see fig. 2.11) and the absolute calibration and integrating it. It can be seen that the prediction is close to the observation. This means that the guessed n_e and T_e are close to the measured n_e and T_e values.

Part III

EXPERIMENT

3 EXPERIMENTAL SETUP AND CALIBRATION

3.1 OVERVIEW

As an overview of the experimental setup was already given in section 2.5.4 and a summary with the more technical details can be found in the Appendix chapter A as well as in [21] and [24], this chapter will focus on one component with particular importance for the experiments conducted for this thesis and on the calibration which is analysed as a potential error source.

3.2 ENTRANCE MIRROR BOX

One part of this thesis is determining the influence of laser misalignment. For this purpose a closer look into the mirror box used to change the laser alignment will be given.
This particular mirror box is called entrance mirror box and was already shown in figure 2.5. A view of the inside is presented in figure 3.1. The three laser beams are depicted in dark green, light green and yellow. Every laser has its own set of remote controlled mirrors (blue and gold) to adjust each laser individually. Two mirrors are required to adjust beam position and angle separately. The adjustment of the beam position is described in more detail in section 4.1. To monitor the entrance beam positions between experiments, cameras (red) are placed behind the golden mirrors. Between the blue and red mirrors are the converging lenses to adjust the beam diameter in the vessel.
The beams exit the box through a pair of windows (light blue) under Brewster's angle to make sure that the transmission is 1, meaning most of the laser power is transmitted (given 100 % polarised lasers). A camera (violet) monitors the Brewster window. This camera was used in this thesis to determine the beam entrance position, because the data of the red cameras was not saved during the experiments. After passing through the second Brewster window, the beam is guided through one entrance port of W7-X into the plasma vessel. A similar box is placed at the exit of the vessel. It is called exit mirror box. It also contains mirrors with cameras behind them, but the mirrors are not remotely controlled. This box also contains the beam dumps and energy monitors.

3.3 CALIBRATION

As discussed in section 2.5, two separate calibration measurements are conducted at W7-X. A relative/spectral calibration and an absolute calibration. Both methods will be described in the following. A more detailed description of the measurements can be found in [24].

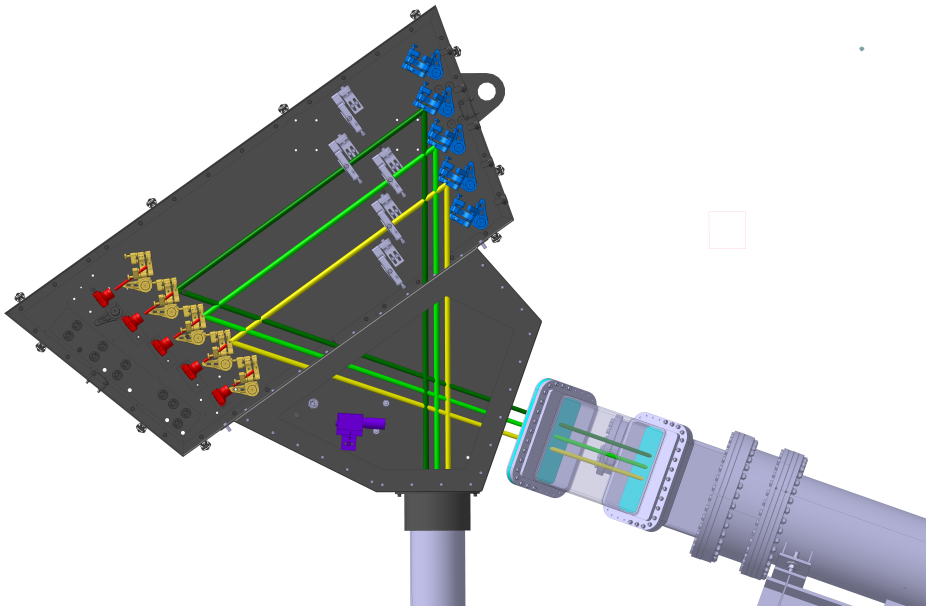

Figure 3.1: Sketch of the entrance mirror box. There are currently three lasers being used for Thomson scattering (dark green, light green, yellow line). They come from the laser room and enter this mirror box from below. Then they are guided over the blue onto the orange mirrors and exit through the two Brewster windows (light blue). The blue and orange mirrors can be remote controlled to adjust the beam paths individually. A set of cameras (red) monitors the entrance beam position during experiments. Additionally a camera (lilac) is looking onto the Brewster window. A similar box (without adjustable mirrors) is placed at the exit of the vessel. It contains another set of cameras to monitor the exit beam positions.

3.3.1 *Spectral Calibration*

The spectral or relative calibration is used to determine the relative sensitivity function $g(\lambda_i)/g_0$ from equation 2.26. For the measurement, the collection optics are retracted (without changing the relative positions of the fibre bundles) and a white diffuse scattering plate is placed in front of it. A supercontinuum pulsed light source (SuperK by KOHERAS) with a high repetition rate (30 kHz) is being used. With a monochromator a wavelength is selected and guided through a fibre onto the scattering plate. The diffusely scattered light is collected by the usual collection optics and guided into the polychromators. This is done in 0.1 nm steps for the spectral range of 700 nm to 1100 nm. This results in five individual filter characteristics for every scattering volume. To get a good signal to noise ratio of the calibration measurement, every wavelength measurement is averaged over 200 light pulses. Because of the high repetition rate of the SuperK this can be done in a reasonable amount of time.
The results of one spectral calibration for one volume can be seen in figure 2.11. There are two principle problems with that kind of measurement. Firstly, because the scattering plate could not be placed in the vessel, the vacuum window that is in front of the collection optics is not included in the measurement. Secondly, the scattering plate is closer to the collection optics than the plasma during the experiments. This is a problem if the *étendue* changes between calibration and measurement. The étendue G is defined by $dG = n^2 d\Omega dA \cos\alpha$, where n is the refractive index, Ω the solid angle, A the area of

the emitting surface and α the angle between the surface normal and the ray [32, p. 238]. For more detail see chapter 6. Also it has been noticed that multiple spectral calibrations conducted at W7-X led to varying filter characteristics in a range of $\pm 5\,\%$. Including this uncertainty into the data analysis is one goal of this thesis and will be discussed in section 4.2. An alternate approach of spectral (and absolute) calibration using Rayleigh scattering and an optical parametric oscillator (tunable wavelength) was tested after this campaign and will be installed for future measurements [33].

3.3.2 *Absolute Calibration*

The absolute calibration is used to determine the absolute calibration factor $\delta L \delta \Omega g_0$ from equation 2.26. There are two common principles for absolute calibration: Rayleigh and Raman scattering. As the laser wavelength is suppressed in the polychromators at W7-X for stray light reduction during the experiments and Rayleigh scattering takes place at the laser wavelength, it is not applicable without using another laser. For that reason, the absolute Calibration is done with Raman scattering.
Raman scattering is scattering at molecules, which have rotational and/or vibrational modes. In contrast to Rayleigh scattering, where the state of the molecule before and after scattering is the same, in Raman scattering the molecule changes its state with respect to its vibrational and/or rotational quantum number. If the molecule ends in a higher energetic state, the scattered light has a correspondingly lowered energy, leading to the so-called Stokes lines. If the molecule ends in a lower energetic state, the scattered light has a correspondingly raised energy. These are the so-called anti-Stokes lines. Because the Thomson diagnostic at W7-X is designed to measure the anti-Stokes scattering, only the high energy side of the laser (below 1064.14 nm) has to be measured. In contrast to the spectral calibration, the Raman calibration is performed with the same lasers and geometry as during the experiments. The vessel is filled with nitrogen gas (N_2) at room temperature and the Raman scattered light is measured in the polychromators. The resulting signal is compared to the well-known Raman spectrum of nitrogen, which can be seen in figure 3.2. Because the spectrum only reaches the spectral channels closest to the laser wavelength, only two channels yield an absolute calibration factor. For a more reliable calibration, the measurement is performed at different nitrogen densities and the measurement at each density is averaged over 500 laser pulses. The use of multiple densities gives the advantage of gaining the absolute calibration factor by determining the slope of the linear density dependence of Raman scattering. This can be described in a similar notation to the scattering formula 2.26 [24]:

$$\left(\int_T s dt \right)_i = n_{N_2} E_l R \delta L \delta \Omega g_0 \tag{3.1}$$

With the left hand side being the integral of the signal s of spectral channel i over laser pulse duration T. The right hand side consists of the density of nitrogen n_{N_2}, the laser pulse energy E_l and R which is a placeholder for known quantities like the scattering cross section and Raman spectrum. Given these parameters, the absolute calibration factor $\delta L \delta \Omega g_0$ can be obtained by the slope of a linear fit, divided by E_l and R. Because R contains the Raman scattering spectrum, also the filter characteristics obtained by the spectral calibration are included in R. The reason for that is that the measured Raman

spectrum is a convoluted with the filter characteristics. This means that any error done in the spectral calibration will also appear in the absolute calibration.

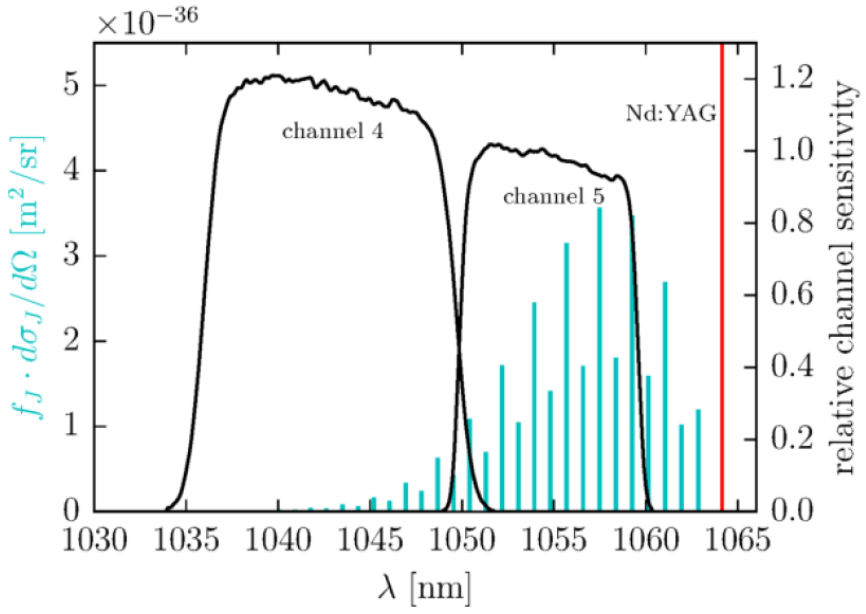

Figure 3.2: Anti-Stokes spectrum for nitrogen (light blue) and filter characteristics of two spectral channels (black). The laser wavelength of 1064.14 nm is shown in red. The Raman calibration is based on the knowledge of the shown anti-Stokes spectrum and the filter characteristics (spectral calibration). By measuring the intensity in both channels for a series of different nitrogen pressures, a linear fit gives the absolute calibration factor for both channels. Either the mean of both calibration factors can be used in the further analysis or only the calibration factor of channel 5, as the signal to noise ratio in this channels is higher, because of more anti-Stokes radiation in this wavelength interval. This figure is reproduced from [24]

4 EXECUTION

4.1 EXPERIMENT ON LASER MISALIGNMENT

One systematic error is laser misalignment which corresponds to a change of the beam path in respect to the beam path during the absolute calibration. If the beam path changes after the calibration the intensity of the laser in the scattering volumes seen by the glass fibres (see A.1) may differ from the one during the calibration measurements. Thus introducing a systematic error. Possible ways of a change of the beam path over time could occur through many effects like thermal drifts, vibrations of components, manual/spontaneous misalignment or even the beam pointing stability of the laser. In this chapter the experiments conducted to measure the influence of laser misalignment will be explained in detail.
The plasma experiments analysed were conducted with nearly constant plasma parameters, giving an ideal condition to manually misalign two of the lasers via shifting the corresponding mirrors. The third laser was kept steady for comparison and to ensure the availability of Thomson scattering data for measurements of electron temperature and density profiles. The full list of analysed experiments can be found in appendix section B.
In figure 4.1 an overview of important parameters is given for the first and the last constant discharge of that day. The first row shows the applied heating power P. It can be seen that the applied ECRH power, while being constant after about 1 s, is about 4.0 MW in 4.1a and 3.3 MW in 4.1b. This shows that in fact not all parameters were the same for all discharges. Any changes of electron density n_e and temperature T_e will be accounted for in the further analysis via normalising to the unchanged laser, henceforth called the reference laser. Starting with discharge number 12 laser 1 and laser 2 were shifted horizontally between discharges. In figure 4.2 the view of the interface of the remote controller to induce the shifts is shown. The left screen shows the view of a mirror of the corresponding laser before the vessel and the right screen shows the view of a mirror after exiting the vessel. Two mirrors per laser can be adjusted with this remote controller. Both are located in the entrance mirror box, which is shown in figure 3.1. The first mirror (blue) allows the manipulation of the beam entrance and the second mirror (orange) of the beam exit. Both manipulations have an interlinked effect on the beam position, but the two degrees of freedom (vertical and horizontal) per mirror give enough parameters to control the whole beam path through the vessel. The red cross hairs mark the position of the beam during the calibration. The green cross hairs mark the current position of the beam. If both cross hairs are aligned the current beam path matches the one during calibration. Typically the position has to be adjusted a few times during a day because of temperature changes in the laser room and torus hall.

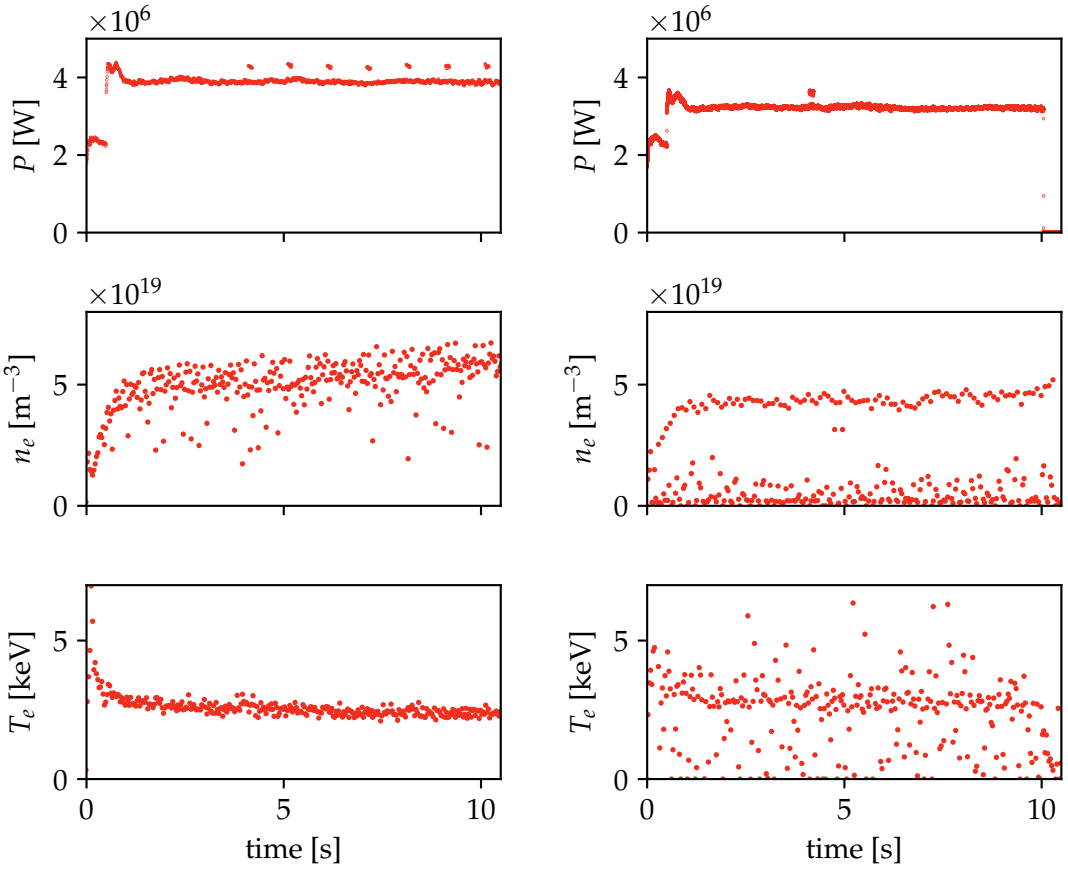

Figure 4.1: Shown are the time traces of the heating power P, electron density n_e and temperature T_e for the first (a) and last experiment (b) of the day. Notice that on the last experiment there are two measured densities because two lasers were misaligned intentionally for this thesis.

4.2 IMPLEMENTATION OF SPECTRAL CALIBRATION ERRORS IN THE THOMSON MODEL

Another source for systematic errors is the spectral calibration which is described in section 3.3.1. The main reason for assuming this to be an error source is that every calibration gives deviating calibration values. These deviations are in a 5 to 10 percent range. To evaluate this uncertainty for the wanted quantities n_e and T_e, these uncertainties have to be included in the statistical model used to calculate n_e and T_e, namely the Thomson model in Minerva. The model is described in detail in section 2.6.4.
In the model the spectral calibration is represented by the *filterFactors* node which is highlighted in red in figure 2.7. To implement the systematic error in this model, these constant calibration values were switched into a probability node (hence, blue colouring in the figure). The probability distribution used to represent the systematic error is a uniform distribution. This distribution could for example go from 95 percent to 105 percent of the formerly used constant value, representing the observation of 5 percent deviations between calibrations. The uniform distribution was chosen because

this assumes the least knowledge about the systematic error. In principle it means that to our knowledge the correct calibration value could lie between 95 and 105 percent of the used value. This represents the starting position of this analysis. Of course the size of the chosen error interval/ uniform distribution effects the size of the error bars. This will be analysed by using different interval sizes.
It has to be pointed out that there are 5 (number of spectral channels) of these calibration factors for every scattering volume. Without assuming any correlation between these factors (which was not done) every one of them is a degree of freedom. Thus, for the first operational period of W7-X *OP1.1* this means that the model went from having 20 degrees of freedom (n_e and T_e for ten volumes) to 70 degrees of freedom (n_e, T_e and $5 \cdot 10$ calibration factors). For the second operational period *OP1.2.* the number of scattering volumes was increased from ten to 42, resulting in 294 degrees of freedom. This increases the time the MCMC needs to converge and thus increases the computational time needed significantly. To improve this and ensure the convergence, the evaluation routine was modified to do one scattering volume after another. For this example it reduces the dimensions to 7 (n_e, T_e and 5 calibration factors) and has to be run 10 times for OP1.1

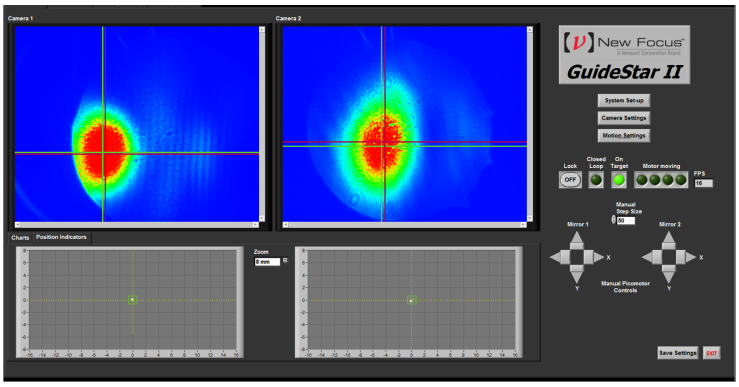

(a)

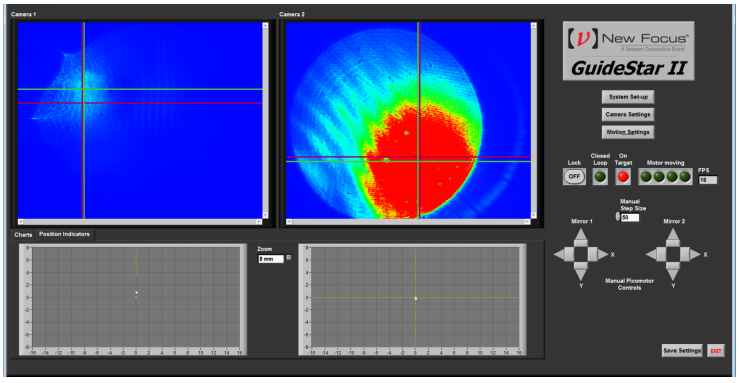

(b)

Figure 4.2: View of the real time camera data used for remote control of laser 1 (a) and laser 2 (b). In both images the left camera view corresponds to the camera in the entrance mirror box (see 3.1) and the right camera view to the camera in the mirror box after the vessel. In b the sensitivity of the first camera was lower, resulting in a weaker signal on the screen. With the triangular shaped buttons the corresponding two mirrors in the mirror box can be tilted horizontally and vertically. This allows full manual control over the beam path. The red cross hairs mark the beam position during calibration and the green cross hairs mark the current beam position.

or 42 times for OP1.2. Physically this procedure is justified, because at this point no information about profile shape was put into the model, so there should be no correlation between the scattering volumes. In principle it should be possible to introduce profile information into the model, but one has to be sure that one does not exclude any possible profile shapes. Else the model would be biased. For that reason it was not done in this analysis, but coud be done in the future, because it is not really sensible to allow too drastic changes in n_e or T_e for neighbouring scattering volumes.

Part IV

ANALYSIS

5 ANALYSIS AND RESULTS

5.1 LASER MISALIGNMENT

5.1.1 *Intentional Misalignment*

Section 4.1 describes how horizontal shifts were induced intentionally on laser 1 and laser 2. In the following, the effects of those shifts on the measured electron density, n_e, will be presented.
First, a measure of the shifts is needed. In the experiment the mirrors could be tilted with a stepper motor. The size of the steps is unknown. If the beam position can be determined, also the shift is known by comparing beam positions. For that reason the beam position was determined via a camera which is looking onto the entrance Brewster window. In figure 5.1 the camera image for laser 1 without a shift (left) and with a 1.9 mm shift (right) is shown. Note that a horizontal shift of the laser appears as a vertical shift in the camera view. Even with only one laser firing, three light spots can be seen. The actual beam on the Brewster window corresponds to the rightmost spot and is due to scattering on dust on the windows surface. Because this speckled reflection is not well suited for determining the beam position consistently and automatically, the spot in the middle was used. This spot and the leftmost spot are probably resulting from reflection (2 times for the leftmost one) on the backside of the Brewster window. The usage of a particular reflection should not introduce an error as long as the same reflection is used throughout the whole analysis.

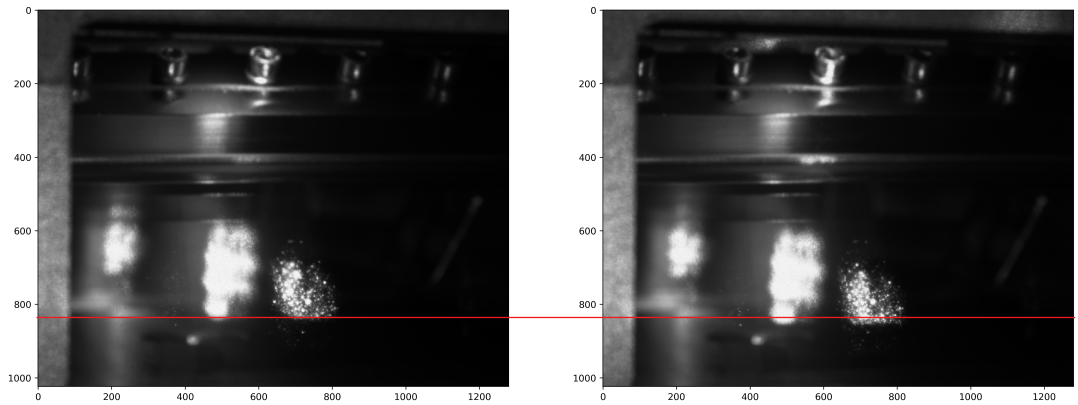

Figure 5.1: Camera images of laser 1 on the entrance Brewster window. The left image shows the laser without shift and the right image shows the laser with a 1.9 mm shift. The red line is a guide for the eye to see the small shift. In both images the rightmost reflection corresponds to the beam on the surface of the window being scattered by dust. The middle reflection is more consistent with the beam shape known from burning paper tests and is probably due to reflection on the backside of the window. This reflection is used for determining the beam position and with that the introduced shifts of the laser.

To get the beam profiles, the middle reflection was integrated along the vertical axis. The average beam position during a plasma experiment is acquired by averaging these beam profiles over the whole experiment. In figure 5.2 the averaged beam profiles of laser 1 are shown for all analysed plasmas. The top figure shows the experiments where a shift in the negative direction was applied. The bottom figure shows where positive shifts were applied. In the further analysis shifts in the negative direction are called *left* shifts and in the positive direction are called *right* shifts. In real space left and right correspond to the horizontal axis directions when looking in the direction of the laser propagation. The red profile marks the laser position at the beginning of the measurement, namely the unshifted profile.

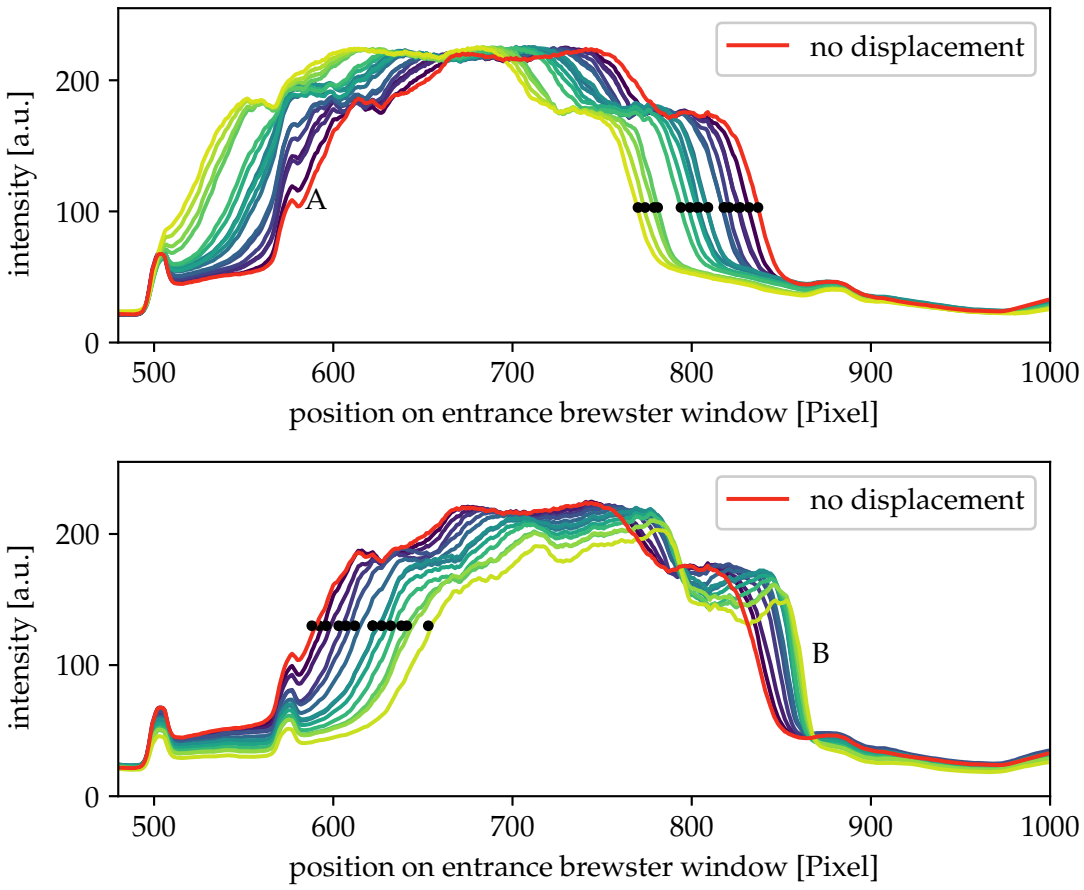

Figure 5.2: Averaged beam profiles of laser 1 for each experiment sorted by shift direction. The top figure shows shifts in the left and the bottom figure shows shifts in the right direction. The red profile marks the unshifted beam. The black dots mark the points chosen to represent the beam position. At position B in the bottom image, it can be seen that the laser is being cut by some kind of aperture.

Because the beam profiles do not have a pronounced maximum, a point on the profile edge was chosen to determine the beam positions. For the left shifts (top figure) the right beam edge was chosen. The chosen points for each profile are marked in black. The left beam edge is not suited for this, because the shape changes with the shifts, which can be seen in the figure at the position marked *A*. For right shifts (bottom figure) it is the other way around. The left edge was used to determine the beam positions, which are also

marked with black dots. For consistency it would be better to choose the same side as before. However, this cannot be done here, because the laser is being cut off at the right edge, marked by B. The cutting can be seen easily by comparing the left and the right edge: while for small shifts (dark blue) both edges move, for larger shifts (green, yellow) only the left edge moves. This leads to a decreasing size of the beam spot and makes the right (unmoving) side of the profile a bad representative for the shift size. The cutting indicates that the beam was positioned near an edge in the beam path and the beam was partially obscured when shifting in that direction.
As a reference, the beam profiles of laser 3 (unshifted laser) are shown in figure 5.3. As in figure 5.2 the averaged profiles are shown for every experiment. The profiles are nearly identical with the unshifted profile (red), showing that the average beam position could be kept stable over many experiments.

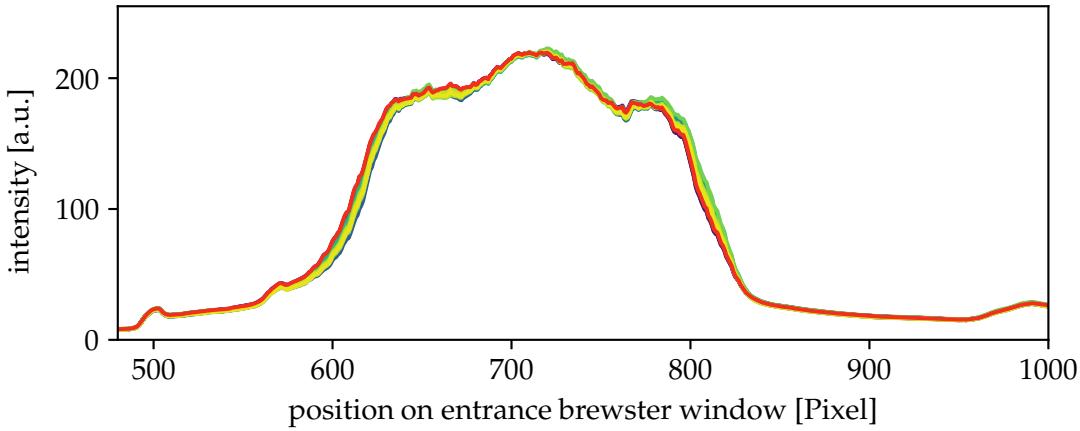

Figure 5.3: Averaged beam profiles of laser 3 for each experiment. It can be seen that the average beam position could be kept stable over many experiments.

Now that the size of the shifts is known in pixels for both shifted lasers, the shifts can be converted into a real space scale by measuring the corresponding length of a pixel. In principle this is not needed for the analysis, because knowing the shifts in pixels is already sufficient. Speaking from an experimentalist point of view, it is still important to know in which order of magnitude those shifts took place. For that a scale paper was placed on the Brewster window and the camera images were analysed, resulting in a scaling factor of $1.58 \times 10^{-4}\,\mathrm{m\,px^{-1}}$. Any error on this scaling factor will only affect the interpretation of the shift size, but not the actual results.
After obtaining a measure (either in pixel or m) of the induced shifts, the impact on the measurement of n_e can be evaluated. To reduce the information and to gain an easy way to represent the effect of a shift on n_e, the mean value $\mu(n_e)$ and the standard deviation $\sigma(n_e)$ were calculated for each plasma experiment. The time intervals over which these values were calculated were matched to the time intervals with constant heating power. This means the startup phase of the ECRH of about 1 s (see figure 4.1) was excluded and the varying experiment length was taken into account.
In figure 5.4a the results are shown for laser 1 and scattering volume 1. The mean value of n_e is plotted over the position of laser 1. Because the electron density was not exactly the same for all the experiments, $\mu(n_e)$ was normalised to the mean density of laser 3

$\mu(n_{e3})$, which was kept steady through all the experiments. As a reference, a grey line at a height of 1 was drawn. Where the red n_e crosses the grey line, laser 1 and laser 3 measure the same mean density. Looking at the profile in figure 5.4a it can be seen that there is a significant drop in measured electron density if the laser is shifted by only a few millimetres.
For a good measurement not only a high signal, but also a low scatter of the measured quantity is needed. To get a measure of the scatter to signal ratio the standard deviation $\sigma(n_e)$ was divided by the mean value $\mu(n_e)$. This is presented for laser 1 and stray volume 1 in figure 5.4b. The behaviour is inverse to the one in 5.4a. In this case, a low value means a good signal to scatter ratio.

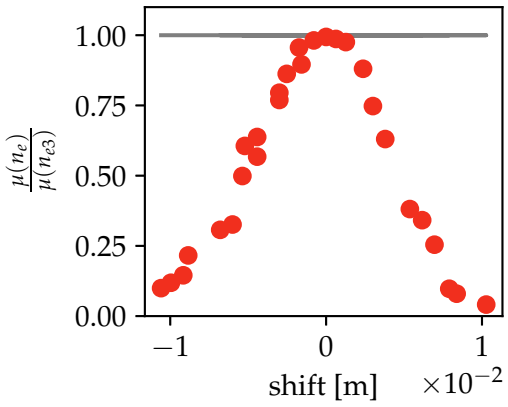

(a) Mean value of n_e for different beam positions. Each value represents one shot with a constantly shifted beam position. A shift of 1 cm leads to effectively no signal.

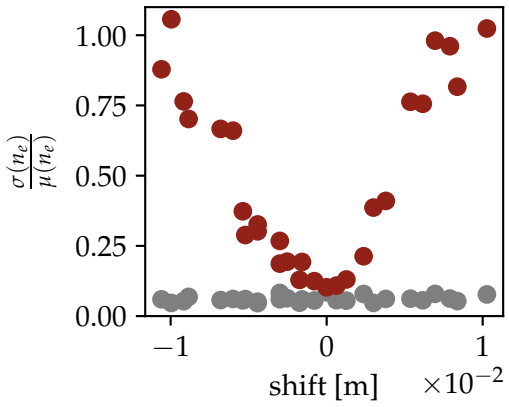

(b) Standard deviation with respect to the mean value for different beam positions. This quantity gives a measure of the scatter to signal ratio. Complementary to a this ratio rises for larger shifts.

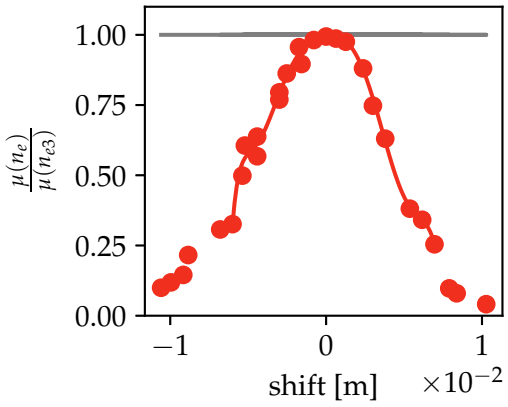

(c) The red line represents a high order polynomial fit around the maximum.

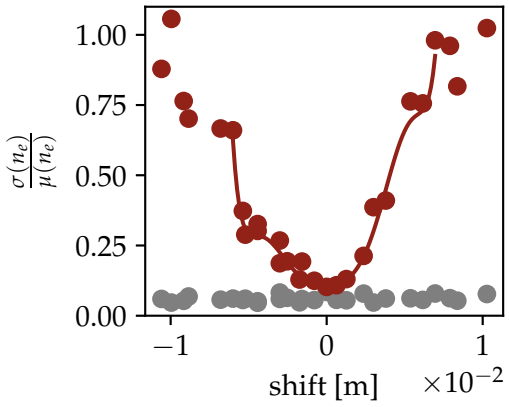

(d) The red line represents a high order polynomial fit around the minimum.

Figure 5.4

The same graphs were obtained for all the scattering volumes and both lasers (1 and 2). An overview graph with all scattering volumes can show if the maxima of $\mu(n_e)$ or the minima of $\sigma(n_e)$ lie in one line through the vessel, meaning that an optimal path exists for all the scattering volumes. To get such an overview graph the information has been reduced. A high order polynomial fit was applied, focusing on a good match around the extrema. This can be seen in figures 5.4c and 5.4d for laser 1 and volume 1. With those polynomials the overview graph shown in figure 5.5 was produced. The dots below the polynomials represent the positions of the maxima. It can be seen that for laser 1 there is no straight line through the maxima of all the scattering volumes. Therefore, the best position is not adjustable with parallel shifts.
To find the optimal (reachable) beam position the extrema are apparently not sufficient. Therefore, a range in which the values are above 90 % of the extreme values is included in the figure. This range is represented by the bars around the dots and will be called optimum range further on. It can be seen that the best position for the scattering volumes can be found around 2 mm (right direction). That would have been the optimal alignment position reachable by purely shifting in the horizontal direction. The same result can be shown by analysing the minima of $\sigma(n_e)$, which is shown in figure 5.6. Here, the optimum ranges are consisting of values between $\sigma(n_e)_{min}$ and $1.5\sigma(n_e)_{min}$. The percentage was chosen such that the ranges are roughly of the same size for μ and σ. The same procedure was applied for laser 2. The final results for all scattering volumes are shown in figures 5.7 and 5.8. Here, it can be seen that it is possible to draw a straight line through most of the extrema. Therefore, the best position can be reached with horizontal shifts for most of the scattering volumes. Only for the outer volumes this does not fit as well. The best horizontal shift would be around -2.5 mm (left direction).
In conclusion, this kind of analysis can in principle be used to find the optimal positioning of the beam. However, not only horizontal, but also vertical and angular shifts have to be included for optimal results. This also means that in the future the previous analysis has to be done for more spatial dimensions.

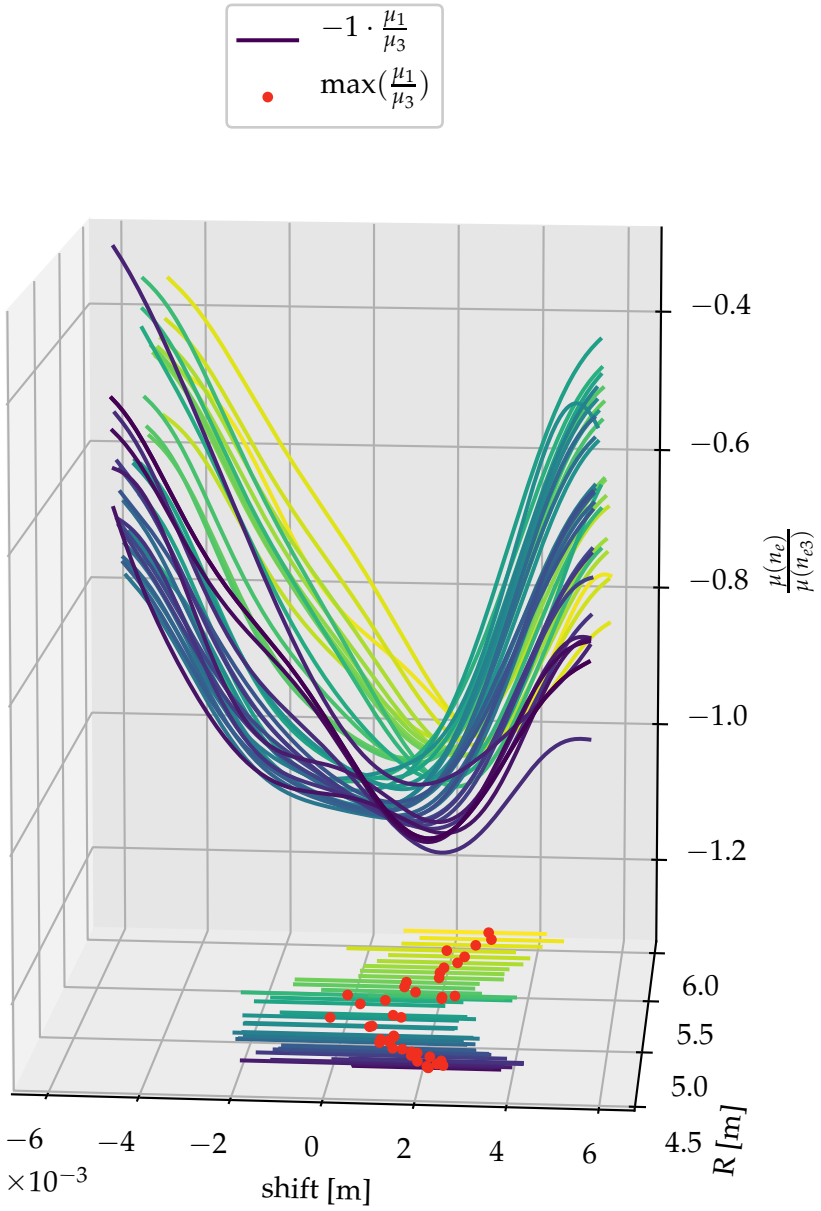

Figure 5.5: Electron density over shift curves of laser 1 shown over the major radius R. Each curve is the result shown in figure 5.4c for a volume at a certain R. For easier visibility the density curves are inverted. Projected below the curves are the shift positions of the maxima as red dots and the optimum ranges. The optimum ranges show the shifts where the measured density is over 90 % of the maximum value. The ideal beam path would connect all dots. With horizontal shifts alone this cannot be realised in this case. Taking the optimum ranges, the best horizontal position of the beam would be at about 2 mm relative to the initial position.

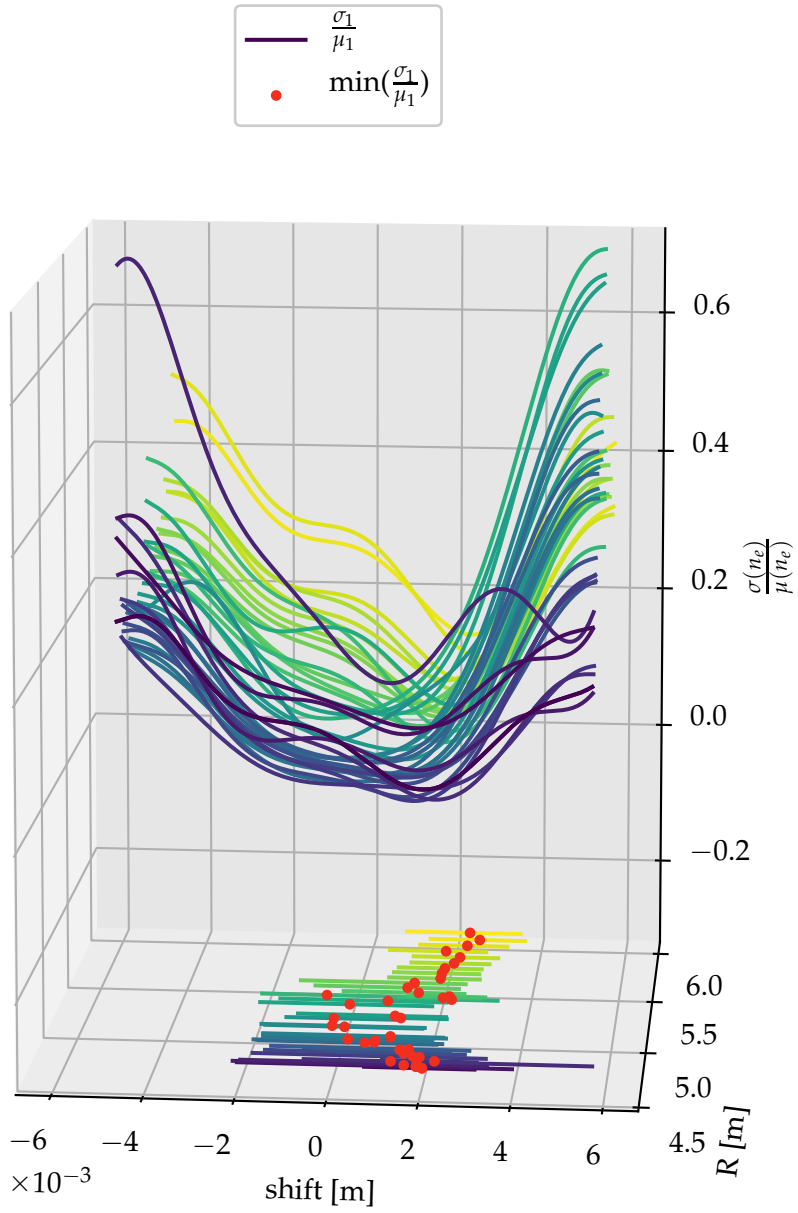

Figure 5.6: Electron density fluctuations over shift curves of laser 1 shown over the major radius R. Each curve is the result shown in figure 5.4d for a volume at a certain R. Projected below the curves are the shift positions of the minima as red dots and the optimum ranges. The optimum ranges show the shifts where the density fluctuations are under 150 % of the minimum value. The ideal beam path would connect all dots. With horizontal shifts alone this cannot be realised in this case. Taking the optimum ranges, the best horizontal position of the beam would be at about 2 mm.

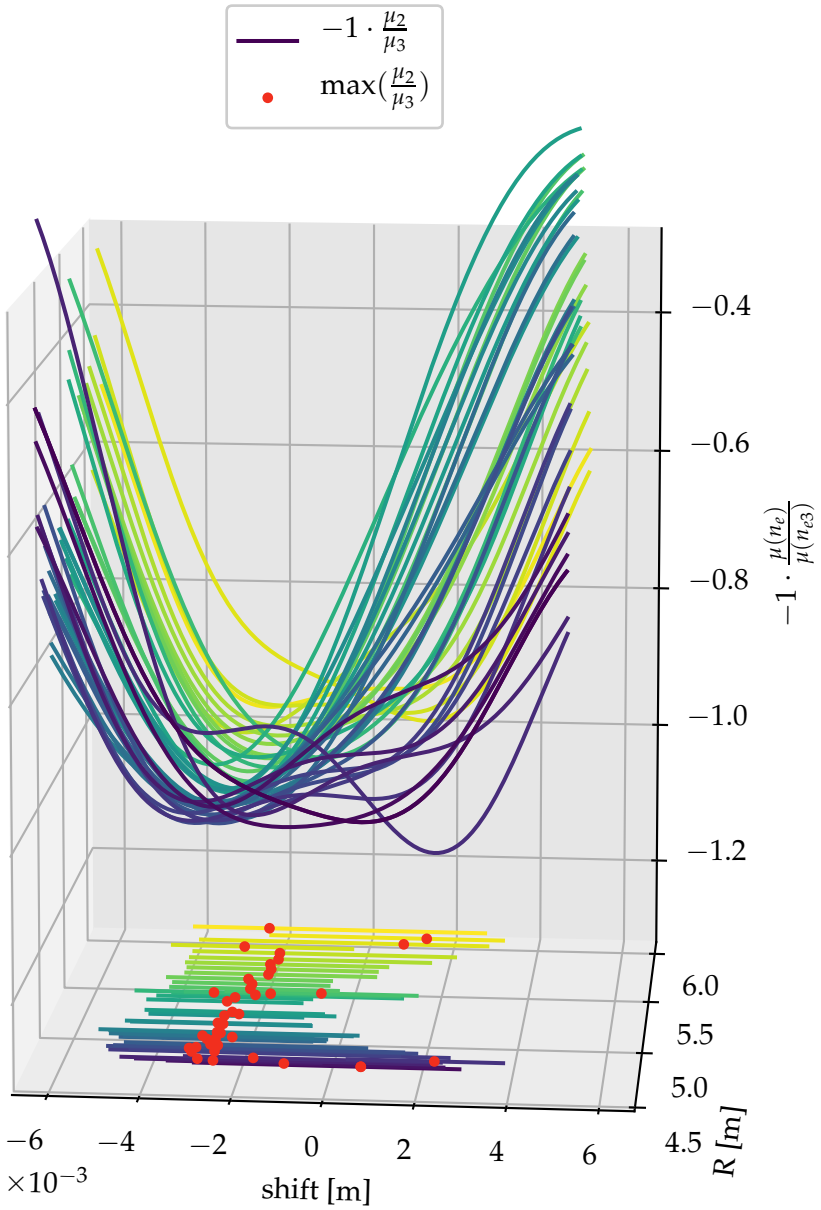

Figure 5.7: Same representation as in figure 5.5, but for laser 2. The ideal beam path would connect all dots. Except for the volumes at the edges a horizontal shift of −2.5 mm would bring the beam path close to the optimum.

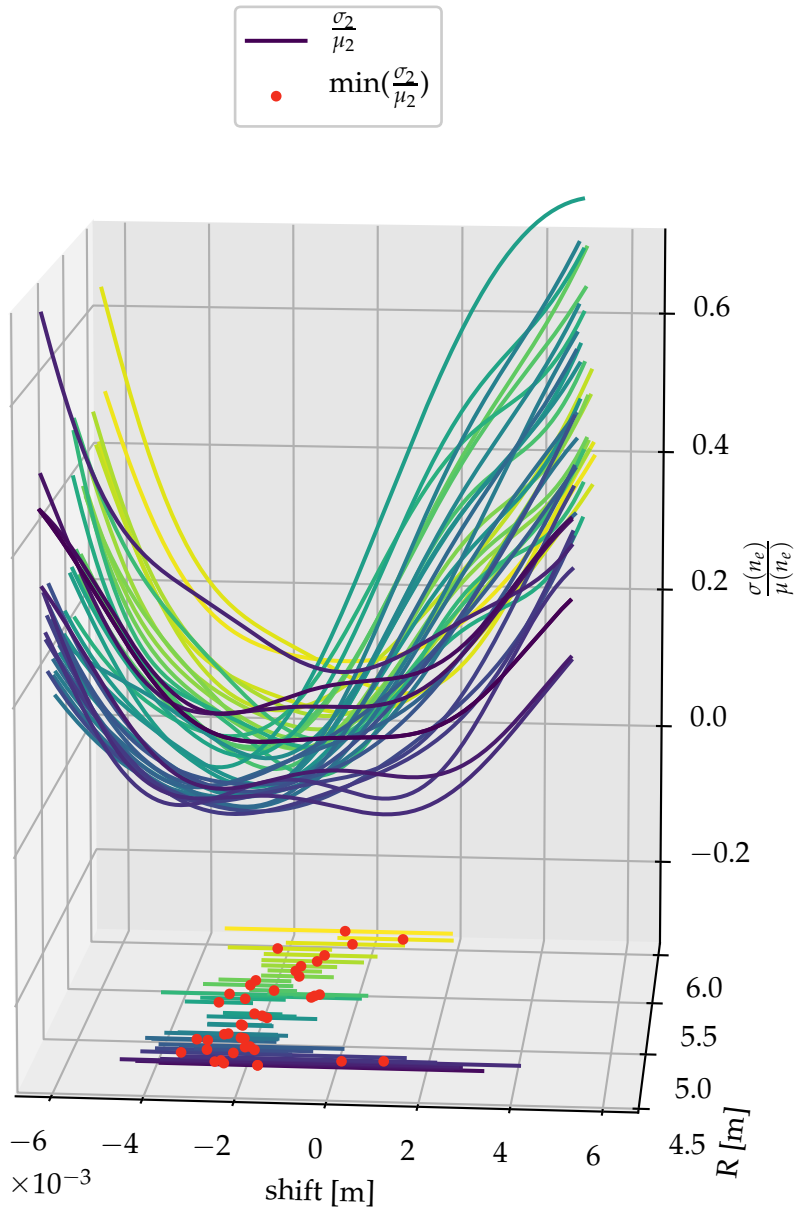

Figure 5.8: Same representation as in figure 5.6, but for laser 2. The ideal beam path would connect all dots. With horizontal shifts alone this cannot be realised in this case. The shift value of −2.5 mm from figure 5.7 seems to give a best position with respect to the fluctuations as well.

To further see the impact of the induced misalignments a representative selection of averaged n_e profiles are shown for different shifts of laser 1 in figures 5.9a and 5.9b. It can be seen that the shifts can change both the amplitude and the shape of the profiles. As observed in figure 5.5, a shift to the right would lead to a better alignment. This explains why the n_e profile shifted by 0.6 mm in 5.9b has higher densities than the unshifted one in 5.9a. Shifts in the left direction do not seem to change the profile shape, but the absolute measurement changes. For example a shift of -3 mm reduces the measured density by one third. Roughly the same can be said about the right shifts, with the exception of the 5.4 mm profile which changed significantly in shape and height. It can be concluded that with a laser shifted by 5.4 mm no reliable profile information can be obtained.

Example profiles for laser 2 are shown in figures 5.9c and 5.9d. The situation for this laser looks different. Consistent with the analysis above, shifts into the left direction (5.9c) seem to only change the profiles marginally. This stable region would be the desired alignment position. There, small changes in the alignment of the laser would not effect the outcome drastically. In contrast, the right shifts (5.9d) exhibit an even more pronounced change in measured density and profile shape than those of laser 1. Even a transition from a peaked profile to a hollow profile can be seen. It is important to note that this transition is solely caused by shifting the laser and not because of changes in the plasma parameters. This is particularly problematic, because one of today's questions for W7-X is if the profiles are hollow, as seen in other stellarators [34] or peaked, as seen in the shown examples. If the laser alignment can also change the measured profile shape and discharges with changing plasma parameters are analysed, then answering this question becomes even more challenging.

One reason for laser 2 exhibiting such a strong dependence on shifts in the right direction has already shown up in figure 5.7. The unshifted profile (at shift = 0) was positioned at the rightmost border of the optimum ranges or slightly outside them. Therefore, it had to be expected that shifts in that direction would influence the profiles more strongly. This is also why the shape changes: while the outer volumes are still inside the optimum ranges, the inner volumes are far outside these intervals. This leads to a stronger drop in the measured density in the centre volumes than in the outer volumes, resulting in the observed conversion from peaked to hollow.

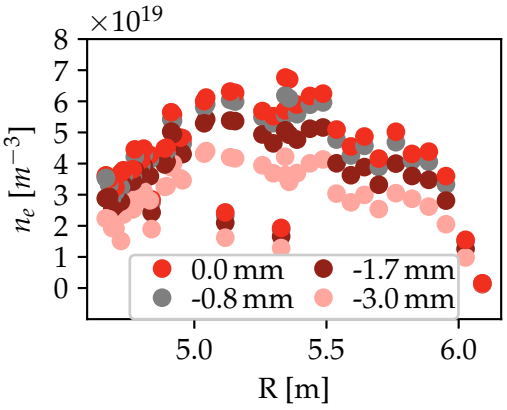

(a) Laser 1: n_e profiles with left shifts.

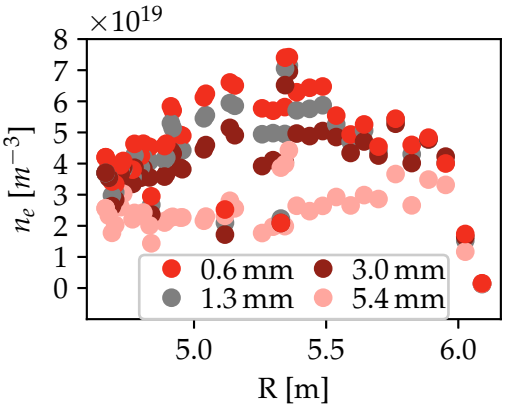

(b) Laser 1: n_e profiles with right shifts.

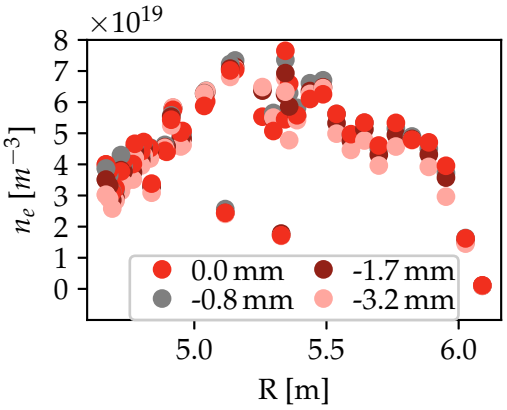

(c) Laser 2: n_e profiles with left shifts.

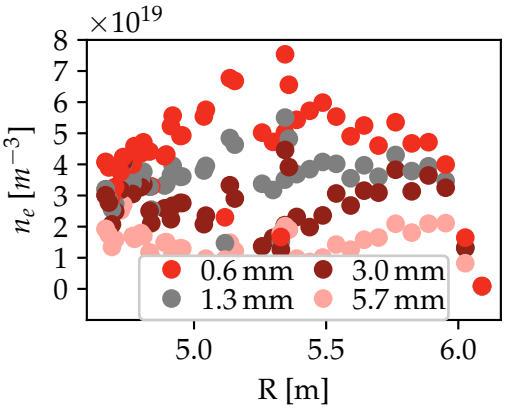

(d) Laser 2: n_e profiles with right shifts.

Figure 5.9: Electron density n_e profiles as a function of the major radius R for different shifts of the lasers. Figures a and b correspond to laser 1. Figures c and d correspond to laser 2. The left figures represent shifts in the *left* or − direction and the right figures represent *right* or + shifts. For a, b and d it can be seen that the shifts influence the profile height and shape. In d a transition from a peaked (0.6 mm) over a flat (1.3 mm) to a hollow profile (3.0 mm) can be seen without any change in the plasma parameters. Figure c shows that it is possible to align the lasers such that the profiles are nearly unaffected by shifts of a few mm.

Taking the average of the optimum ranges could give a hint on how large the space is in which the lasers have to be kept stable. Assuming that it is equally important to have a good signal and a high signal to noise ratio, the mean value was taken of both kinds of optimum ranges ($\mu(n_e)$ and $\sigma(n_e)$) together. This resulted in a range size of 4 mm. This corresponds to the design margin of ± 2 mm for the Thomson scattering system at W7-X (see section 2.5.4). But it has to be kept in mind that in principle nothing should change inside of the design margin and with the calculated result, the measured densities are only 90 % at the edges and the scatter to signal ratio is larger by a factor of 1.5. So the design margin is not really fulfilled. One reason for that could be a larger beam diameter than expected. The beams on burning paper are shown in figure 5.10. It seems that the burning paper does not give a reliable measurement for the beam size. Because of its non linear blackening behaviour the edges of the beam are not seen. Those edges seem to have enough laser energy to influence the beam profiles like shown before. It should be noted that laser 3 has a smaller spot size than laser 1 and 2. This could contribute to the better results of that laser and will be discussed in more detail in the next section (5.1.2).

Counter measures for such small adjustment margins could be widening the scattering volumes via optics, shifting the beam focus to reduce the beam size or reducing the beam size by tailoring the lasers. The last point seems to be promising as laser 3 has a small beam diameter and delivers profiles with smaller scatter. Because the lasers are all of the same type, it should be possible to tune the beam diameter of the other two as well. Another approach would be including position measurements of the lasers on both sides of the beam pass through the vessel and getting a calibration factor for a range of laser paths, thus correcting for the misalignment after the measurement. It could be argued that if misalignment is the deviation from the calibration position and the calibration was done for all positions, then there is no misalignment anymore. Considering the scatter, it is still favourable to find the optimal position.

Up to now the effect of misalignment was only examined for intentional shifts and the profiles were averaged over the whole experiment programme. Because the alignment affects profile height and shape, it would be reasonable to assume that effects like beam pointing stability and mechanical vibrations of components could affect the measurements. That this really is the case will be shown in the following section.

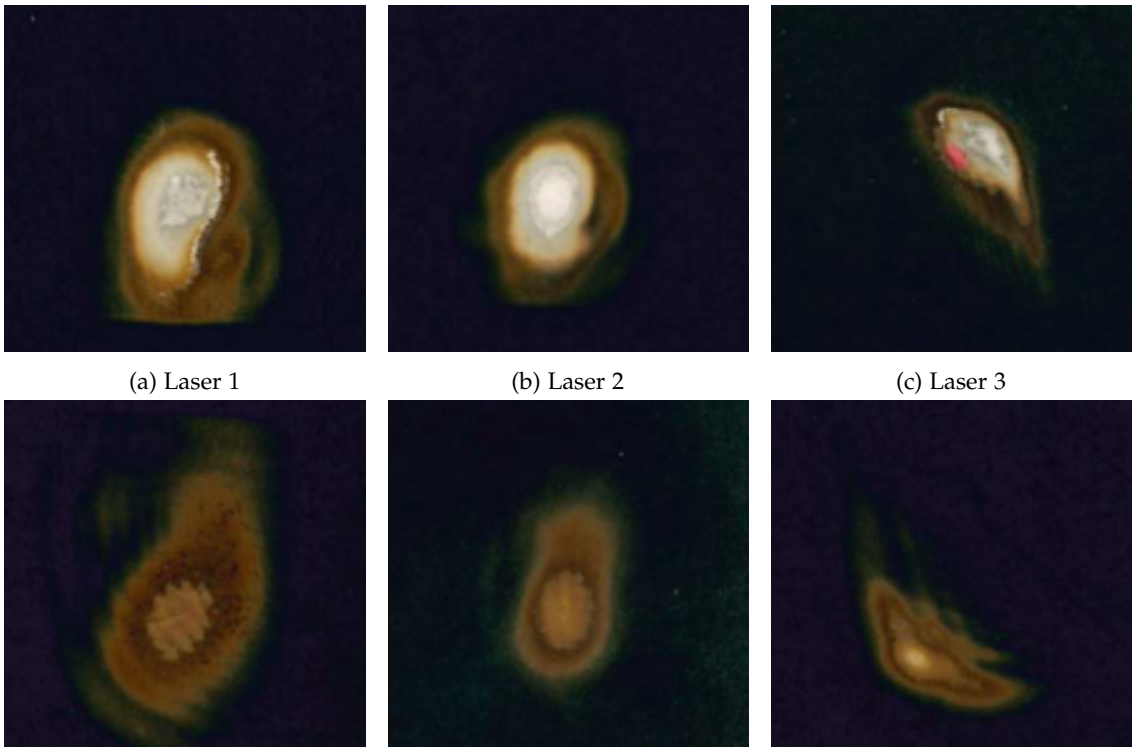

(a) Laser 1 (b) Laser 2 (c) Laser 3

(d) Laser 1 (e) Laser 2 (f) Laser 3

Figure 5.10: Beam profiles on burning paper. Top images a, b and c represent the beam profiles at the entrance of the vessel. Bottom images d, e and f after the exit of the vessel. Laser 3 has a smaller beam spot than laser 1 and 2.

5.1.2 *Alignment Fluctuations*

To see the influence of temporal changes of the alignment on the n_e profiles, programmes with constant plasma parameters had to be investigated. For that reason, the same operational day as in the previous analysis was chosen. The analysis could be done for all the programmes on that day, but for simplicity the reference programme (number 12 also seen in figure 4.1a) where no manual shifts were introduced was chosen. In principal the analysis is the same as before, with the difference that the profiles of n_e and the lasers (for measuring the beam position) are not averaged anymore. For the beam profiles this means more fluctuations in the beam shape and the edges which were used before to determine the beam position did not give a good measure. Instead, the centre of mass of the profiles was used. For the density instead of using the mean $\mu(n_e)$ the actual n_e profiles at a given time point were evaluated.
In figure 5.11 the single pulse profiles are shown. As a comparison the averaged profile, which was used in the previous analysis, is shown in red. It can be seen that the average profile gives a good representation of the profiles, but the individual profiles still have deviating shapes. To visualise the beam position, the centre of mass was plotted below at the arbitrary height of 50. These graphs also show what was concluded in the previous section: laser 3 has a smaller beam diameter. Additionally, the centre of mass and thus the position of the beam of laser 3 varies less than the position of laser 1 and 2. After obtaining the positions of the individual laser shots, those had to be compared to the corresponding values of n_e.

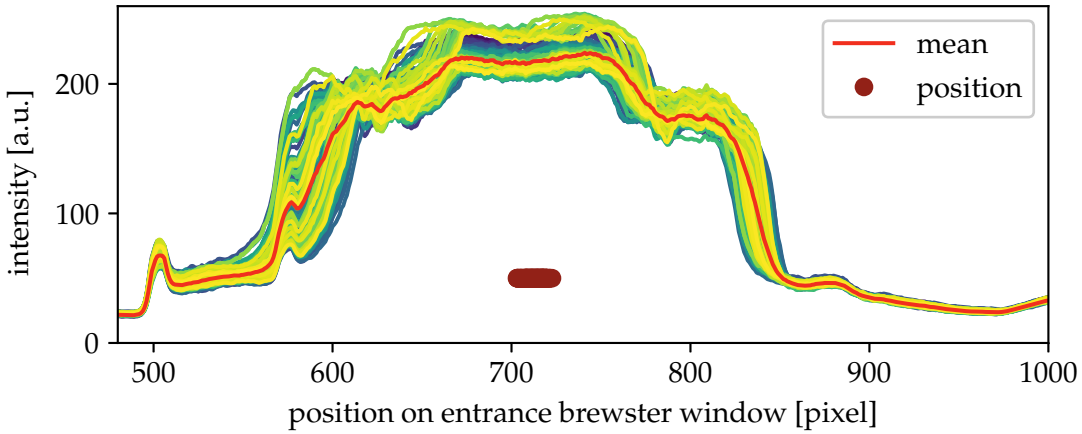

(a) Laser 1

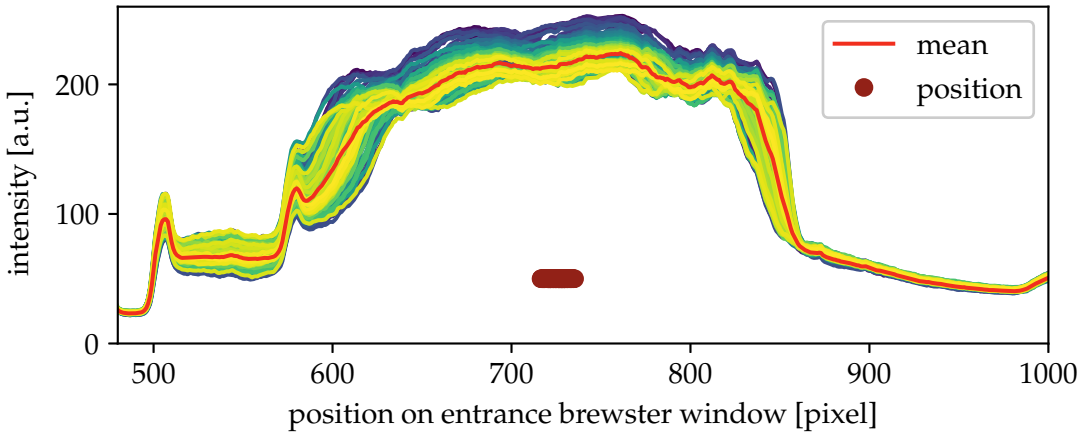

(b) Laser 2

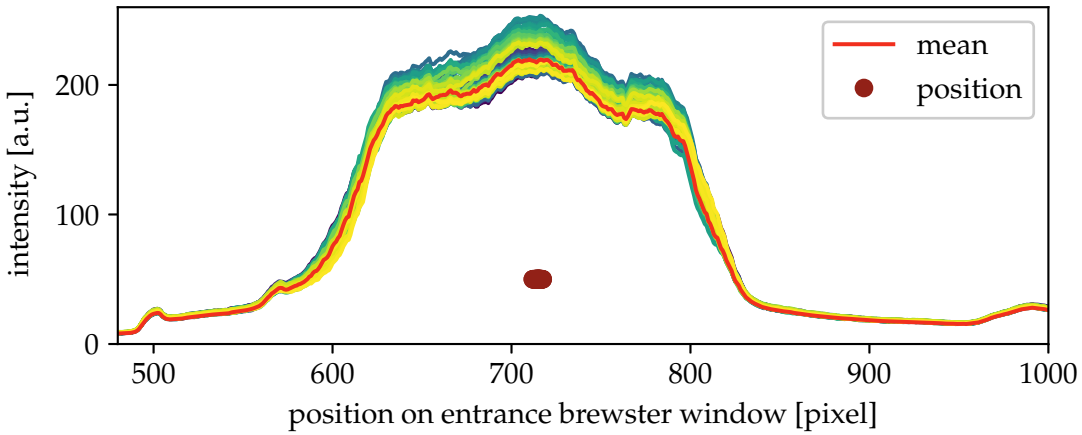

(c) Laser 3

Figure 5.11: Single laser shot beam profiles for one W7-X shot. In red the previously used averaged beam profile is shown. It can be seen that the average profile gives a good representation of the single shot profiles, but there are still some deviations. As dark red dots the calculated beam positions are plotted below the profiles. The centre of mass was used as the position. Laser 1 and 2 show a lot more deviation in the position than laser 3.

Because of the constant plasma parameters during this experiment the measured density in one scattering volume should be the same over the whole programme. Parameters giving evidence for a constant density are for example the electron temperature, the diamagnetic energy (measured with diamagnetic loops) and the line integrated density (measured with an integral electron density dispersion interferometer). Because these three individually measured parameters are constant in time, the density profiles can also be assumed to be constant. In figure 5.12 the density for three of the scattering volumes is plotted over the beam position for all three lasers. For consistency regarding the previous analysis, the initial beam position is set to the average position and the deviation from that position is called shift.

At the first glance it is again apparent that laser 3 is more stable, which is seen by the smaller range of shifts. It can also be seen that for volume 1, laser 1 has a flat density characteristic and thus is well aligned for that scattering volume. This results in a comparable jitter of n_e to the one of laser 3. Laser 2 however seems to sit on one edge of the scattering volume. This results in a significant drop of signal on the right side. By regarding the other shown volumes it can be seen that there are cases for which laser 1 or laser 2 measure either a flat or dropping characteristic. This indicates again that in order to align the laser optimally for all the scattering volumes, the one dimension (horizontal) evaluated here is not enough.

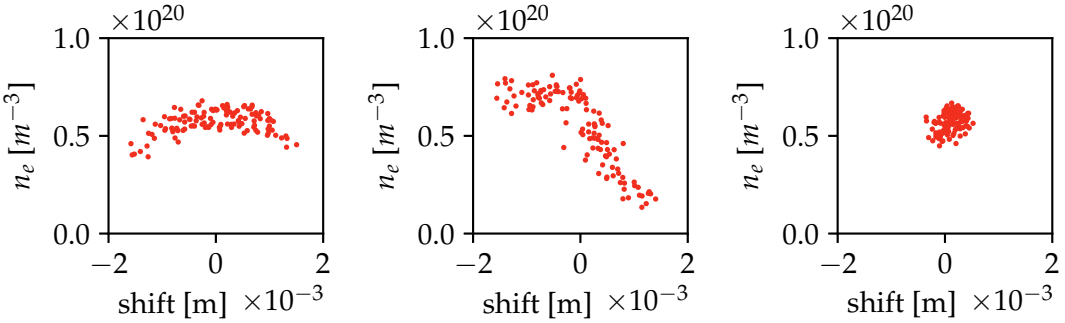

(a) Volume 1 with $R = 3.692\,\text{m}$

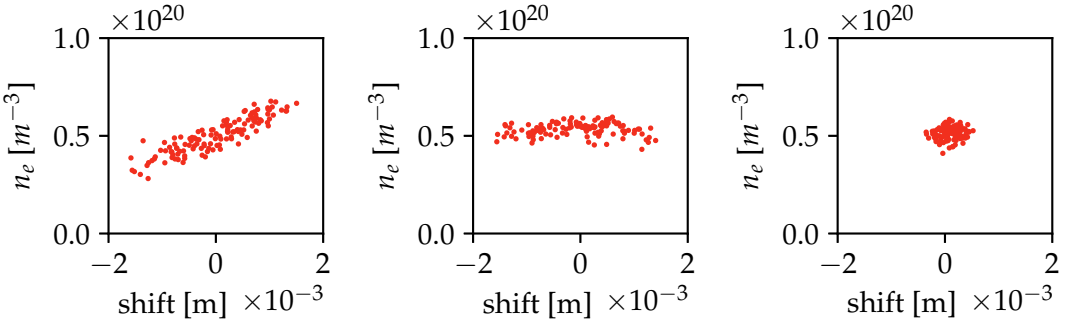

(b) Volume 11 with $R = 4.047\,\text{m}$

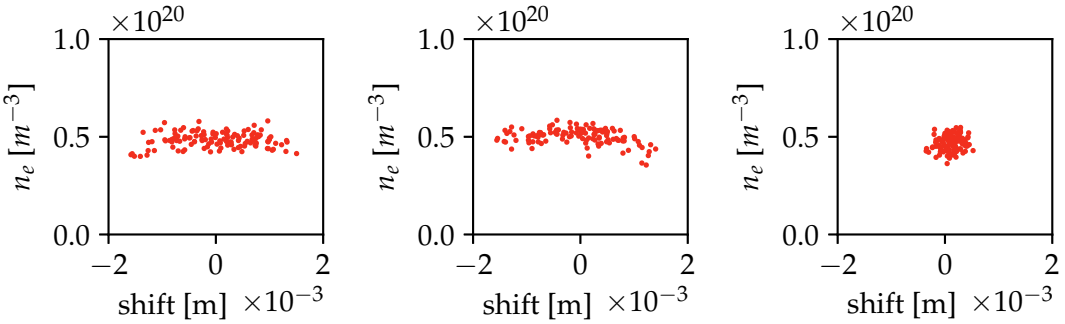

(c) Volume 1036 with $R = 3.475\,\text{m}$

Figure 5.12: Non-averaged n_e over shift characteristics for three different volumes located at major radius R. From left to right the measured data can be seen for laser 1, 2 and 3. A flat density characteristic means that the same density was measured, despite positional changes between laser shots. This is the desired operational mode. It can be seen that for the first volume (a) laser 1 measured a flat characteristic, while the characteristic measured with laser 2 exhibits a significant drop on the right side. For the second shown volume (b) the characteristic of laser 2 is flat and the one of laser 1 is shift dependent. For the third volume (c) all characteristics are flat. This shows that even if a laser is aligned for one volume, it is not necessarily aligned for all the volumes. Like before it can be seen that for laser 3 the variation of the position is smaller than for the other 2 lasers.

The characteristics with dropping edges show that the positional fluctuations introduce a significant error to the measurement. Fore example, in scattering volume 1, laser 2 measures only about a fourth at the right edge compared to the left edge. To give an impression of the error bars introduced by these positional fluctuations all the measured n_e values are shown over the major radius R in figure 5.13. This shows, as expected, the least variation in laser 3. To better compare the other two lasers with the more stable third laser, the data points of the third laser were plotted in black on top of the previous graphs in figure 5.14. The increase of variation can be seen by the protruding red data points. It is visible that laser 1 mostly shows more deviation on the outboard side (larger R) of the vessel. Laser 2 shows the most deviation in the centre. There, in the margins of the possible values only because of the positional jitter either a hollow, flat or peaked n_e profile can be drawn.

In conclusion, these alignment fluctuations are responsible for a significant error in the measurement. This has to be compensated in the future for example by the aforementioned positional calibration and position control has proven to be an essential factor. In the next step, it will be investigated why the beam positions of laser 1 and 2 seem to fluctuate more than the beam positions of laser 3.

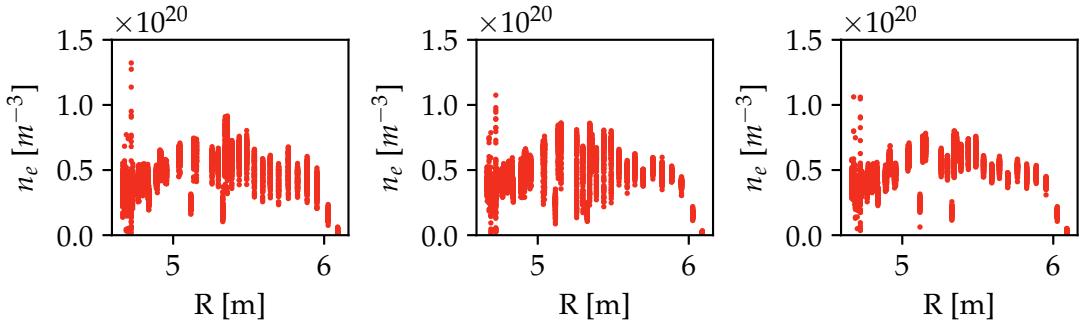

Figure 5.13: Displayed are all measured electron densities n_e over the major radius R for laser 1, 2 and 3 (left to right). The graphs give an impression of the error of the n_e measurement.

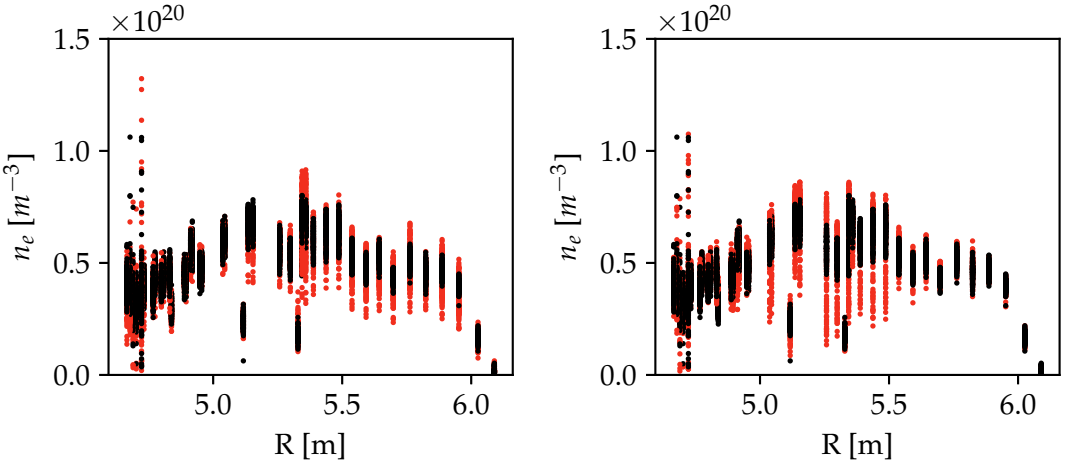

Figure 5.14: Shown in red are all measured electron densities n_e over the major radius R for laser 1 (left) and 2 (right). For better comparison the densities measured with laser 3 are shown in black. The increase of the error caused by the stronger fluctuations of laser 1 and 2 can be seen for most volumes (major radii) by the much larger scatter of the red values. The most significant effect can be seen for the middle volumes and laser 2.

5.1.3 *Identifying the source of positional fluctuations*

When two of three identically built lasers exhibit more spatial fluctuations than the third one, mechanical vibrations come to mind. That only two of the lasers should have a larger beam pointing stability (counter-intuitively the pointing stability is given in µrad, so a smaller pointing stability means a more stable laser) seems unlikely.
In the mirror setup of the Thomson scattering system, laser 1 and 2 go over the same mirrors while laser 3 has a separate one. So these mirrors seem likely candidates. To find the responsible ones, the mirrors were tested in the lab after the campaign ended. The test was done as described in the following and a schematic diagram of the experimental setup can be found in figure 5.15.
An adjustment laser was guided through the mirror box. It was projected on a screen and imaged with a camera. With the camera the movement of the laser was tracked. In several measurements, each of the mirrors in the mirror box were exposed to a constant airflow one at a time. This method was used to ensure a contact free measurement and because airflow, caused by a pressure difference between the torus hall and the labs, could be the source of the mechanical vibrations.
The measurement is shown for one mirror box in figure 5.16. It can be seen that one of the large mirrors exhibits a stronger variation than the others. A view into the mirror box is shown in figure 5.17. Laser 1 and 2 go over the large mirrors while laser 3 goes over the small mirrors. A closer look onto the large mirror which exhibits the jitter is shown in figure 5.18. Unlike the other mirrors which are connected directly to the mirror holder, this mirror is connected via an aluminium angle with the small mirror, which is then connected to the mirror holder. This was done because of spatial constraints. However, the L shaped fitting is too flexible regarding torsion. This causes the larger jitter which is only in one degree of freedom and which corresponds to the jitter axis (horizontal) seen in the previous analysis. As a consequence, the angle was exchanged with a square shaped tube (see figure 5.18b), which is not susceptible to torsion. That this improves the stability is proven by the repeated measurement shown in figure 5.16. A small jitter still exists, but not one mirror is standing out like before. This will hopefully improve the measurements during the next campaign.

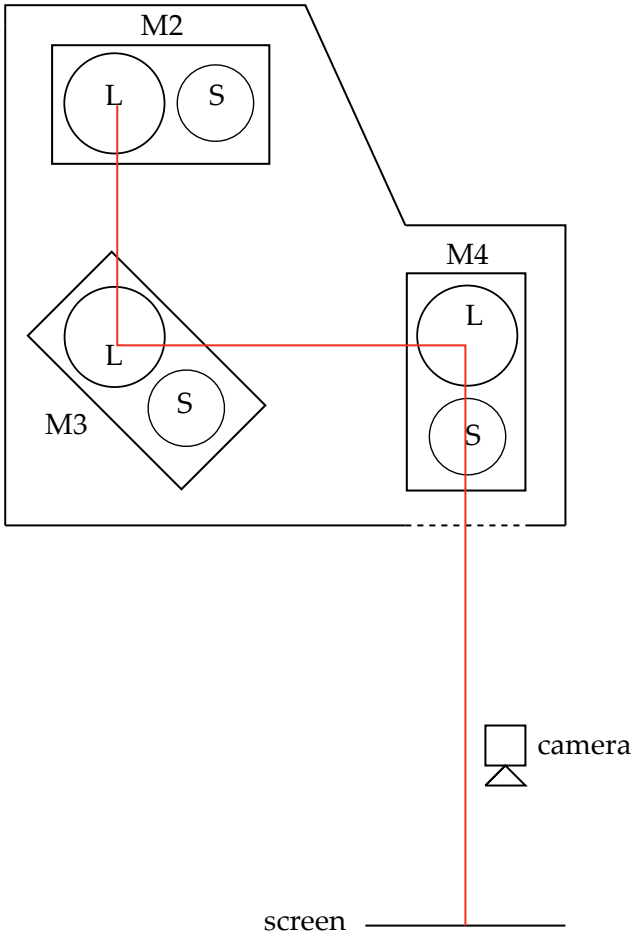

Figure 5.15: Scheme of the mirror box with the mirror sets M2, M3 and M4. Each set consists of a large mirror L and a small mirror S. During this experiment an adjustment laser (red line) went over all the large mirrors onto a screen. One after the other, the mirror sets were exposed to a constant airflow. The resulting movement of the laser on the screen was captured by a camera. The experiment was repeated with a beam path over all the small mirrors.

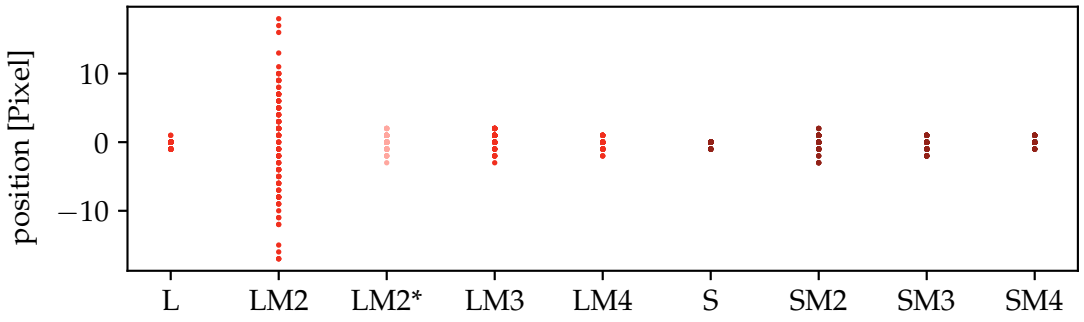

Figure 5.16: Beam positions (centres of mass) of an adjustment laser on a screen while a constant airflow was present on a mirror in the beam path. On the x-axis the indicator *L* denotes that the beam path went over the large and *S* over the small mirrors. *M#* is the name of the mirror with airflow. The two reference measurements without airflow are marked with just an *L* or *S*. It can be seen that only while there was an airflow on *LM2* changes the beam position. A repeated measurement with an improved mirror holder is indicated by *LM2**, proving that the mirror holder was responsible for the strong position variations of laser 1 and 2 during the experiments.

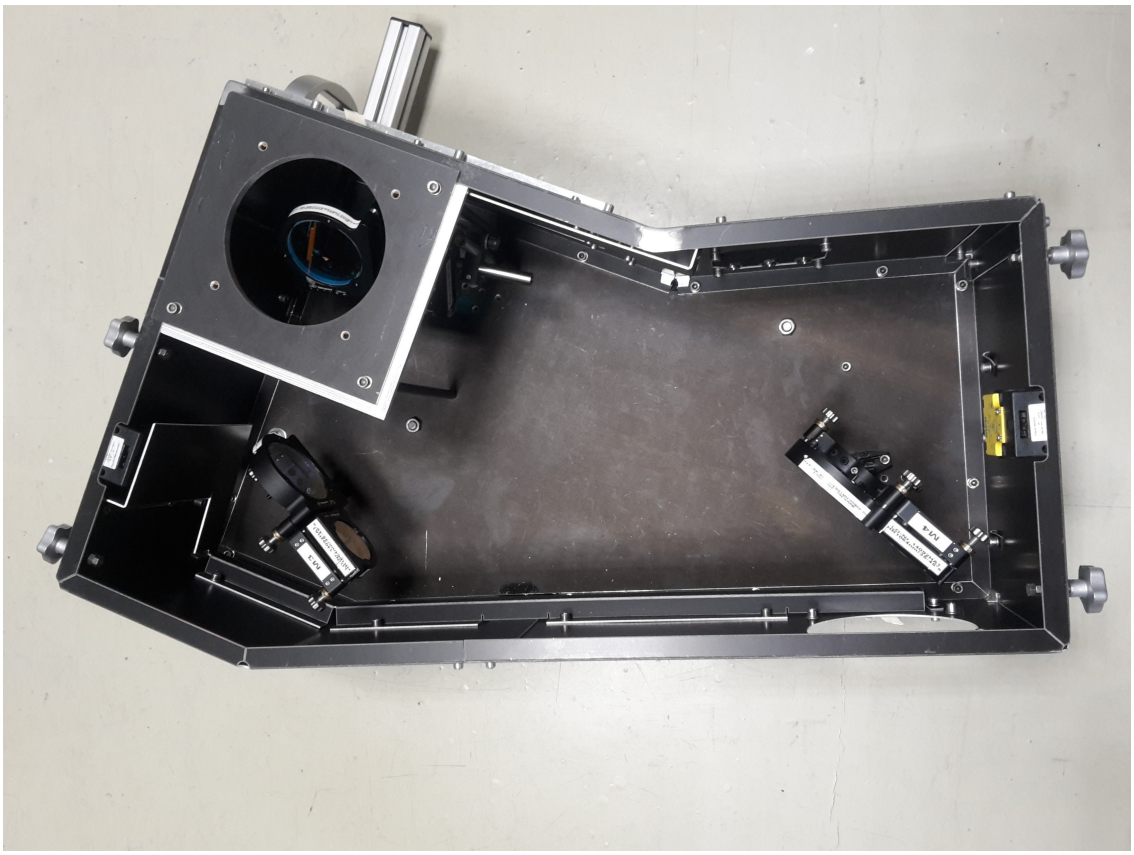

Figure 5.17: Image of the mirror box. The laser enters the box from the top through the entrance hole. It goes from mirror M2 (upper left), over M3 (lower left) to M4 (lower right) and exits through the exit hole. During this experiment the box is strapped to the table to reduce vibrations from the box itself.

(a) Old version of the mirror holder with an L shaped bar as a connection between the small mirror (left) and the large mirror (right).

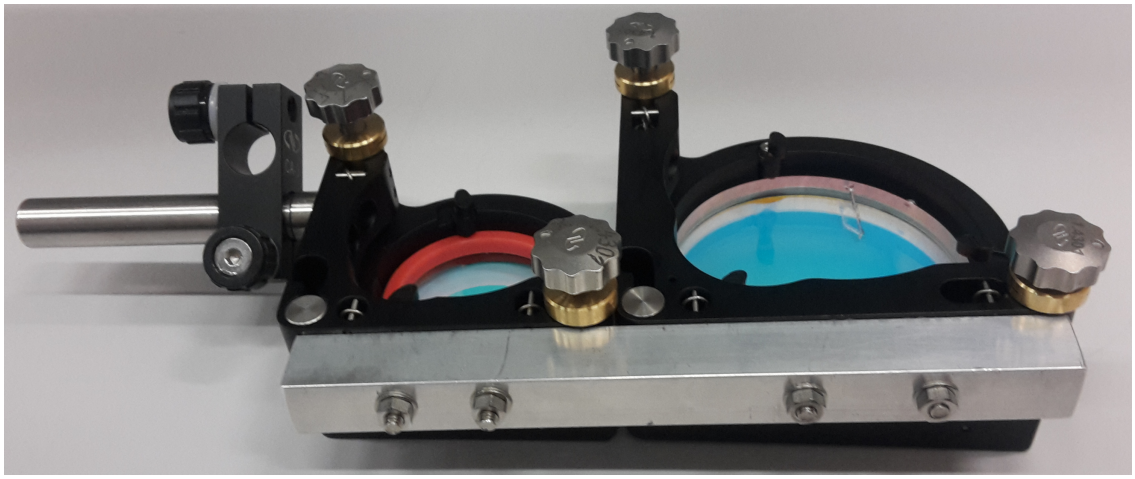

(b) New version of the mirror holder with a square shaped tube as the mirror connection.

Figure 5.18: Images of the old a and the new b version of the mirror holder.

5.2 SPECTRAL CALIBRATION

Comparing several spectral calibration measurements shows that the spectral calibration for each filter varies in a $\pm 5\,\%$ range. The goal of this analysis is to include this systematic error between measurements into the Bayesian data analysis model described in section 2.6.4. The idea is to include nuisance parameters representing the uncertainties of the calibration. In the Thomson model (see figure 2.7) the theoretical scattering spectrum (calculated from the initial guess for n_e and T_e with equation 2.26) is multiplied with the spectral calibration of each channel. When the result is multiplied with the respective absolute calibration factor, it should represent the *theoretical* measurement in a channel given the initial guess for n_e and T_e. To include the uncertainty of the spectral calibration in the model, a set of parameters called *filterFactors* was added to the model. One filterFactor is a random number between 0.95 and 1.05 which will be multiplied to the spectral calibration of one channel. This represents the aforementioned $\pm 5\,\%$ uncertainty of the spectral calibration measurement. To represent the calibration process, only four of five spectral channels per volume are multiplied with a filterFactor. The spectral channel, which is also absolutely calibrated (channel five) will not be varied. In the model this means that only relative changes between the channel calibrations are allowed (as was intended).

In total, there is one filterFactor for each channel (except each fifth channel for the aforementioned reason) resulting in $42 \cdot 4 = 168$ nuisance parameters. Now, instead of only guessing n_e and T_e for each volume for each iteration of the MCMC, n_e, T_e and the filterFactors $\{f_i\}$ are guessed for each iteration. This increases the dimensionality of the model from $2 \cdot 42 = 84$ to $2 \cdot 42 + 4 \cdot 42 = 252$. To reduce this high dimensionality the model was changed to calculating one volume at a time, which leaves solving a $2 + 4 = 6$ dimensional problem 42 times. The *guessing* of these parameters resolves to drawing a random number from a probability distribution. As mentioned in section 2.6 to denote no prior knowledge of the quantities, a uniform distribution was chosen for n_e and T_e. The same is done for the filterFactors. Hence with each iteration of the model not only n_e and T_e are varied, but also the spectral calibration is different from variation to variation. How this affects n_e and T_e will be discussed in the following.

The initial values are set to $n_e = 1 \times 10^{19}\,\mathrm{m}^{-3}$, $T_e = 1\,\mathrm{keV}$ and filterFactors = 1.0. The Hooke and Jeeves algorithm used to get into a parameter space with high probability usually takes about 16 iterations. To ensure MCMC conversion, 100,000 iterations are discarded (*burned*) and samples generated by the following 50,000 iterations are saved. For an exemplary iteration of the MCMC see section 2.6.6. This process is repeated for every scattering volume.

In figure 5.19 the density (top) and temperature (bottom) profiles without variation of the filterFactors are shown. The bars in the figure represent a colour coded histogram of the samples drawn with the MCMC (after MCMC conversion). In Bayesian terms they represent the joined probability distribution, consisting of priors and likelihood, in other words the posterior distribution without the normalisation with the evidence (see section 2.6). To reduce the information, the most likely value, also called the maximum-a-posteriori (maximum of the posterior) is shown as a white dot for each volume. The error bars represent the 95 % confidence intervals. As a side note, 95 % confidence intervals are the non-Gaussian/asymmetric equivalents of the $\pm 2\sigma \approx 95.45\,\%$ of Gaussian distributions. From the example of the density profile in figure 5.19 it also becomes evident that the

model and thus the error bars cannot explain the drastic changes in n_e of neighbouring plasma volumes in the given error bars. Before this thesis it was unclear if the systematic error in the spectral calibration is responsible for these channel-to-channel variations.
The temperature profile looks more reasonable, but also there not every substructure seems physically meaningful considering the error margins. The temperature in the volume located at the outer edge is not well represented because there was not enough scattering signal. This becomes evident, when looking at the density measured in that volume. With near to no signal, any temperature is as likely as the other. Hence it is important to always take both, n_e and T_e profiles, into account to interpret the measurement.
The n_e and T_e profiles for the same time point with the inclusion of the spectral calibration error of $\pm 5\,\%$ (meaning filterFactors are in a range of 0.95 to 1.05) are shown in figure 5.20. The result looks similar to the one without the filter variation. For a better comparison only the maximum-a-posteriori values and the 95 % confidence intervals for both scenarios are shown in figure 5.21. It becomes evident that the changes in the model only affected the results slightly. The 95 % confidence intervals increase slightly with the inclusion of the spectral calibration error (with filterFactors). The maximum-a-posteriori values are mostly the same.

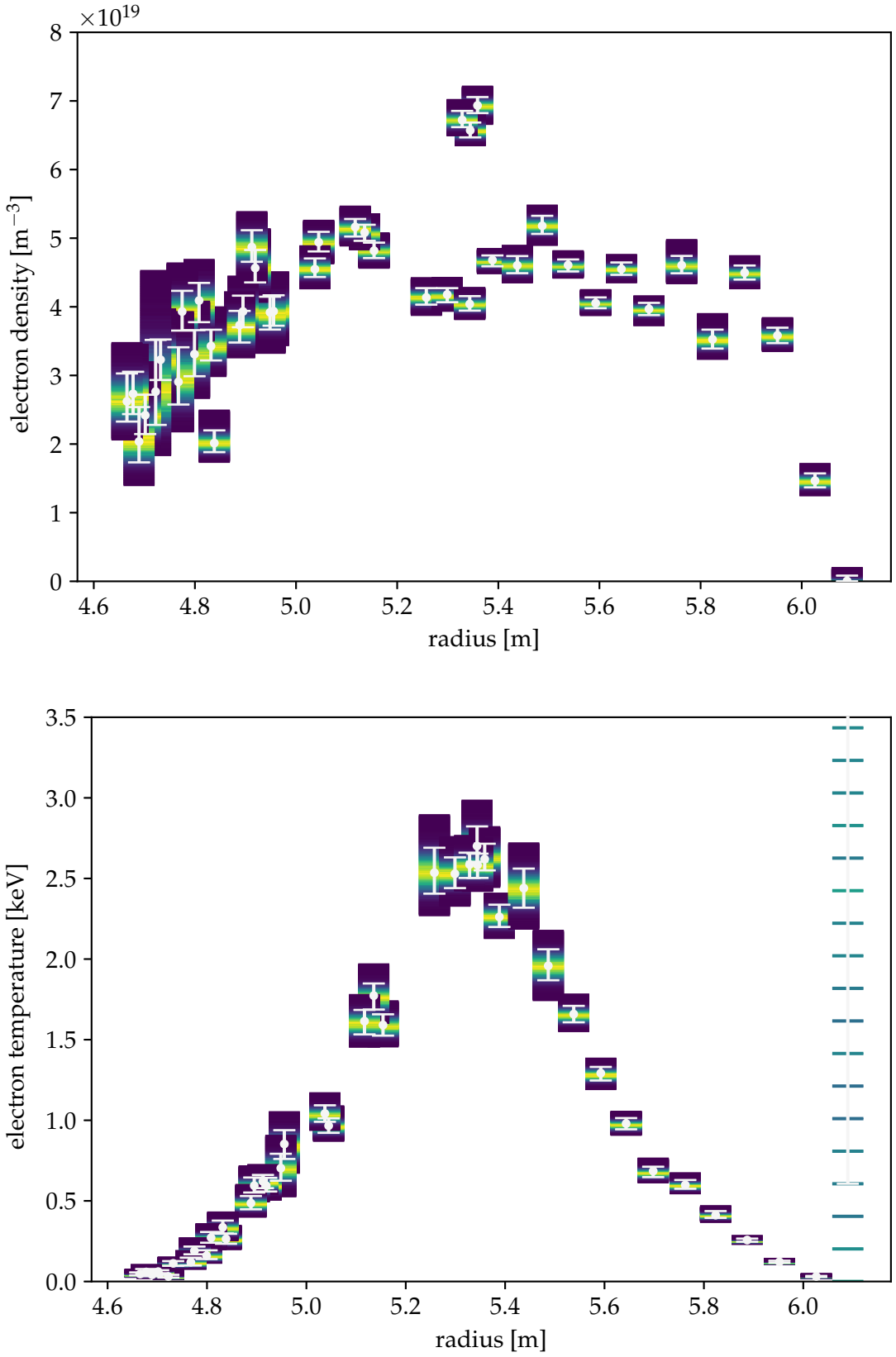

Figure 5.19: Shown are the electron density (top) and temperature (bottom) over the major radius resulting from the Bayesian analysis **without** any variation of the spectral calibration. As dots the most likely values (maximum a posteriori) are plotted with the 95 % confidence interval as error bars. Underneath each dot, a colour coded histogram of the MCMC samples is shown. This colour coded histogram represents the posterior distribution, resulting from the Bayesian analysis. The most likely value and the 95 % confidence interval are calculated from this distribution.

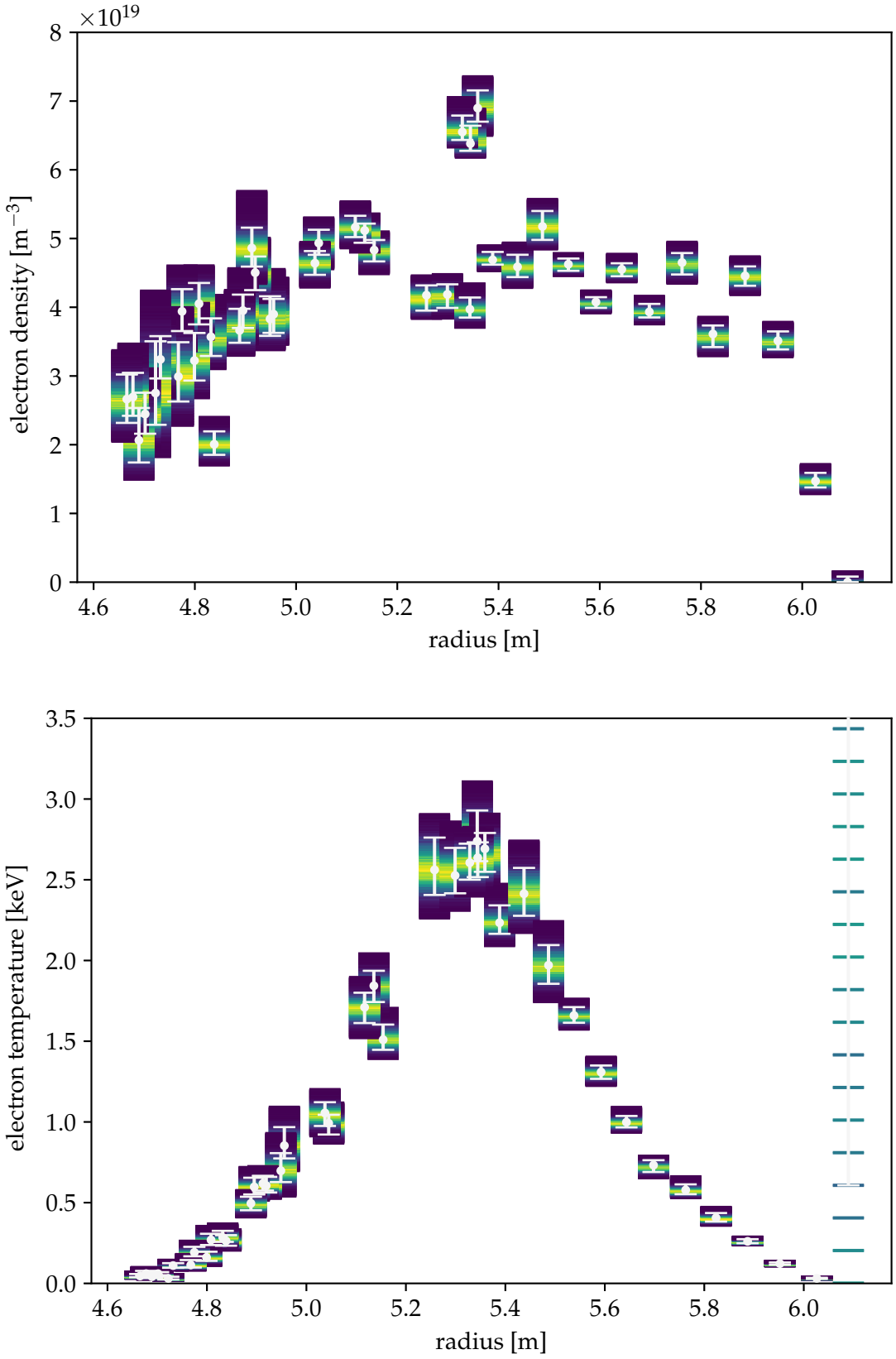

Figure 5.20: Shown are the electron density (top) and temperature (bottom) over the major radius resulting from the Bayesian analysis **with** variation of the spectral calibration. As dots the most likely values (maximum a posteriori) are plotted with the 95 % confidence interval as error bars. Underneath each dot, a colour coded histogram of the MCMC samples is shown. This colour coded histogram represents the posterior distribution, resulting from the Bayesian analysis. The most likely value and the 95 % confidence interval are calculated from this distribution.

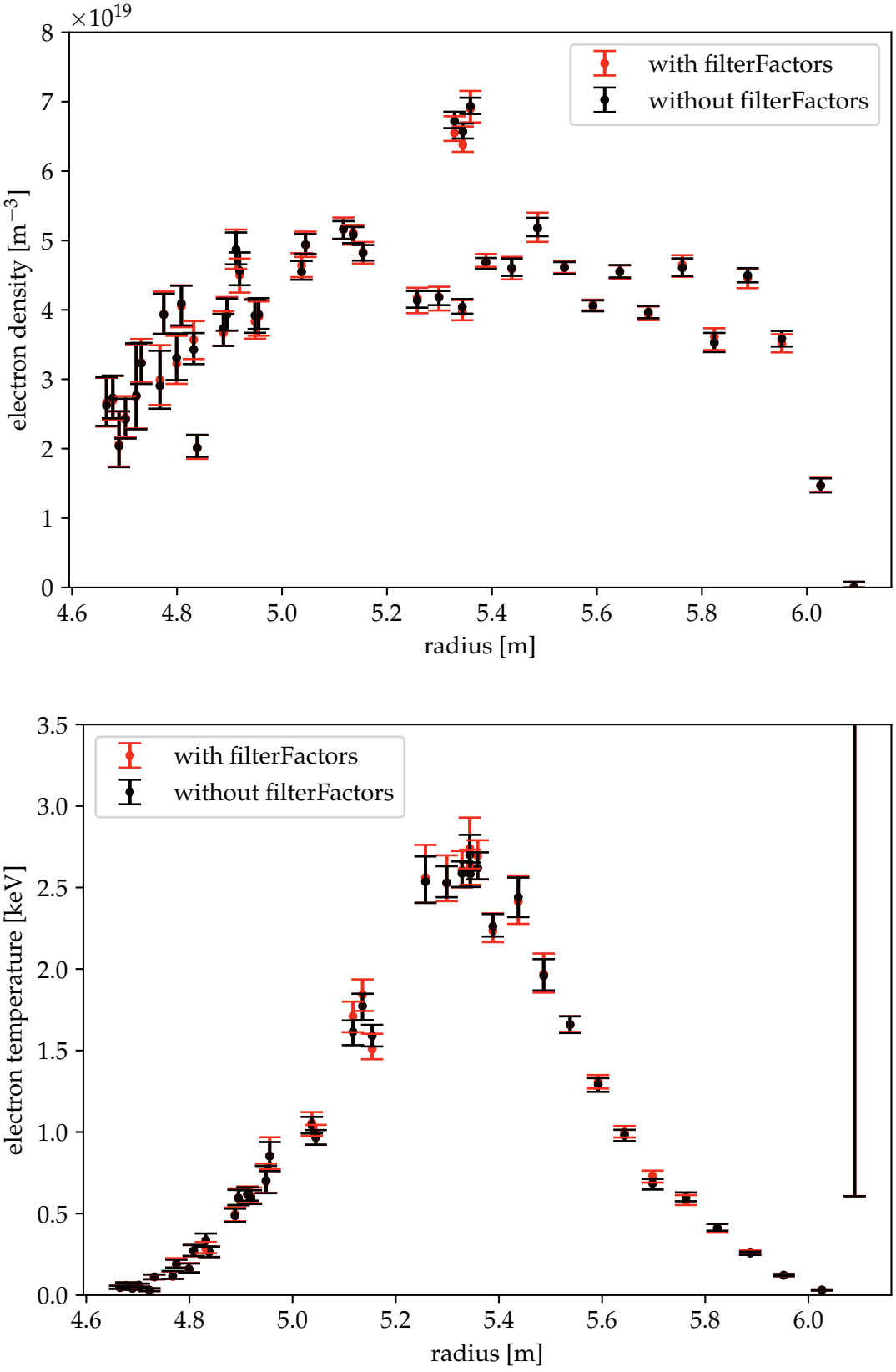

Figure 5.21: Shown are the electron density (top) and temperature (bottom) over the major radius with (red) and without (dark red) variation of the spectral calibration. It can be seen that the results are almost the same. The variation of the filterFactors seems to only slightly increase the error bars.

In the following it will be investigated if the small impact of the variation of the spectral calibration on the 95 % confidence intervals is due to a *self calibration* effect. It is in the nature of an MCMC to preferentially assume parameters with a high probability. This could lead to 'only' shifting the spectral calibrations by a more or less fixed value via the filterFactors (if the posterior pdf is narrow). In principal this is a desired effect because it means compensating this kind of systematic error, but it could result in small error bars. To investigate this effect, the marginalised posterior distributions of the filterFactors are shown for one volume in figure 5.22. The marginalised posterior pdf's of the four filterFactors (four varied polychromator channels) are represented by histograms of the sample distributions. The topmost filterFactor shows a nearly uniform pdf, meaning that the variation of this filter has no significant impact on the posterior pdf. The second filterFactor shows a broad but localised distribution, favouring a slightly smaller spectral calibration factor. The third and fourth filterFactor assume mostly the extreme cases and a part of the distribution seems neglected. This result was unexpected. For a further study of this effect, the analysis was repeated for two other prior distributions, which is shown in figures 5.23 and 5.24. In figure 5.23 the filterFactors were varied between 0.975 and 1.025 and in figure 5.24 they were varied between 0.90 and 1.10.
In comparison to the initial analysis, it can be seen that the posterior distributions for all three cases look nearly identical. This behaviour is expected in the case of filterFactor one (top most) and two (second from top). FilterFactor one shows a nearly uniform distribution for all three cases. FilterFactor two shows a localised distribution for all three cases, but the distribution seems to be cut off in the case with a smaller prior range and the larger prior range shows that the initial case might also be cut off. Only looking at this filterFactor distribution, it could indicate that the assumption of a ± 5 % error, which was based on experimental observations, might still be too small from a purely statistical point of view as the distribution only drops to near zero at the edges for the ± 10 % case. However, the behaviour of filterFactor three and four is not yet understood. It is strange that both factors tend to assume mostly the extreme cases and that a part of the distribution seems not to be explored. To check if this non-exploration of a portion of the parameter space is the cause for the only small increase in the error bars, an alternative method was tried, which will be discussed in the following.

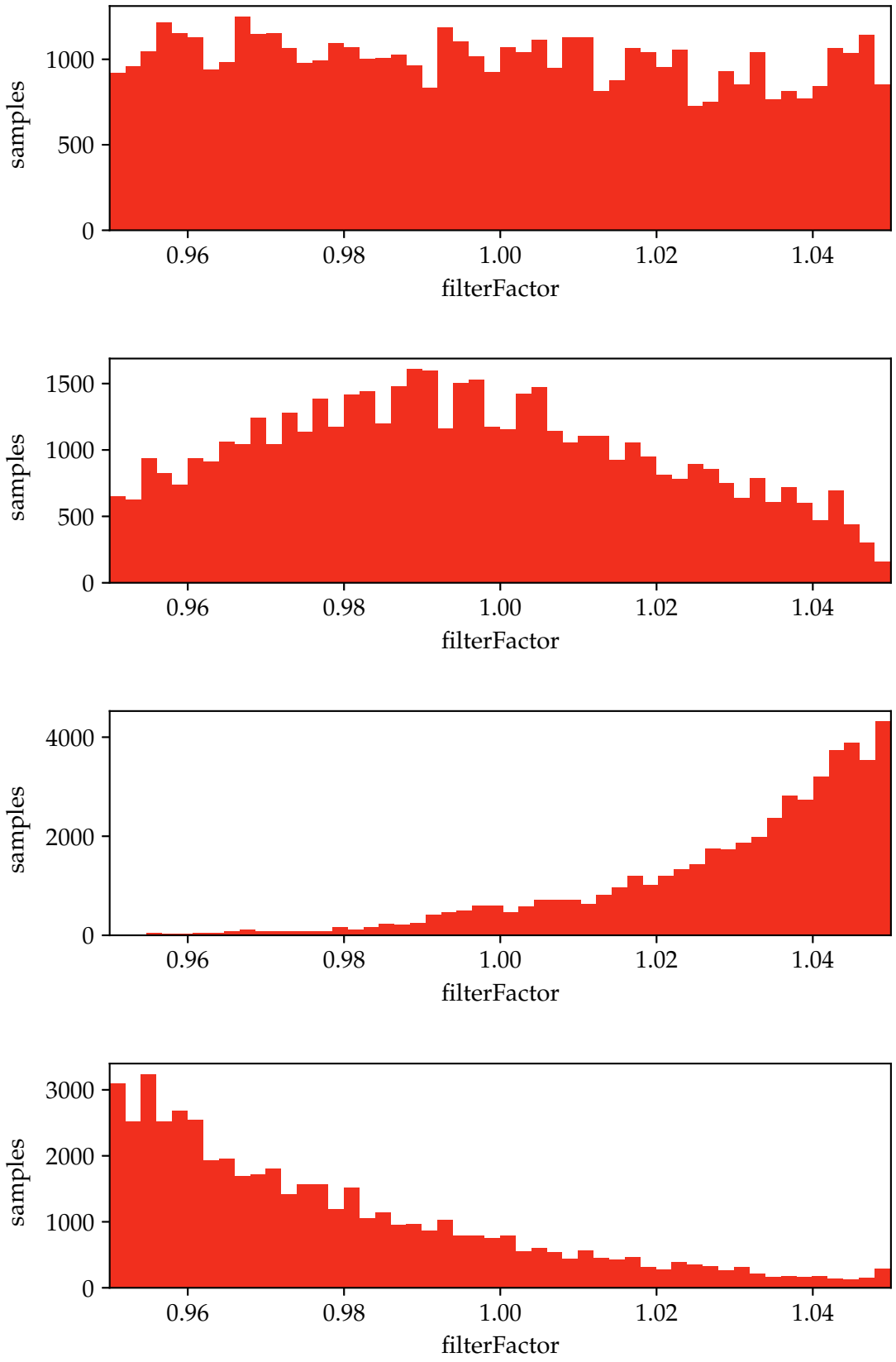

Figure 5.22: Posterior distribution of the filter variation for one volume and the four varied polychromator channels represented by a histogram of the filterFactors. The filterFactors are distributed between 0.95 and 1.05.

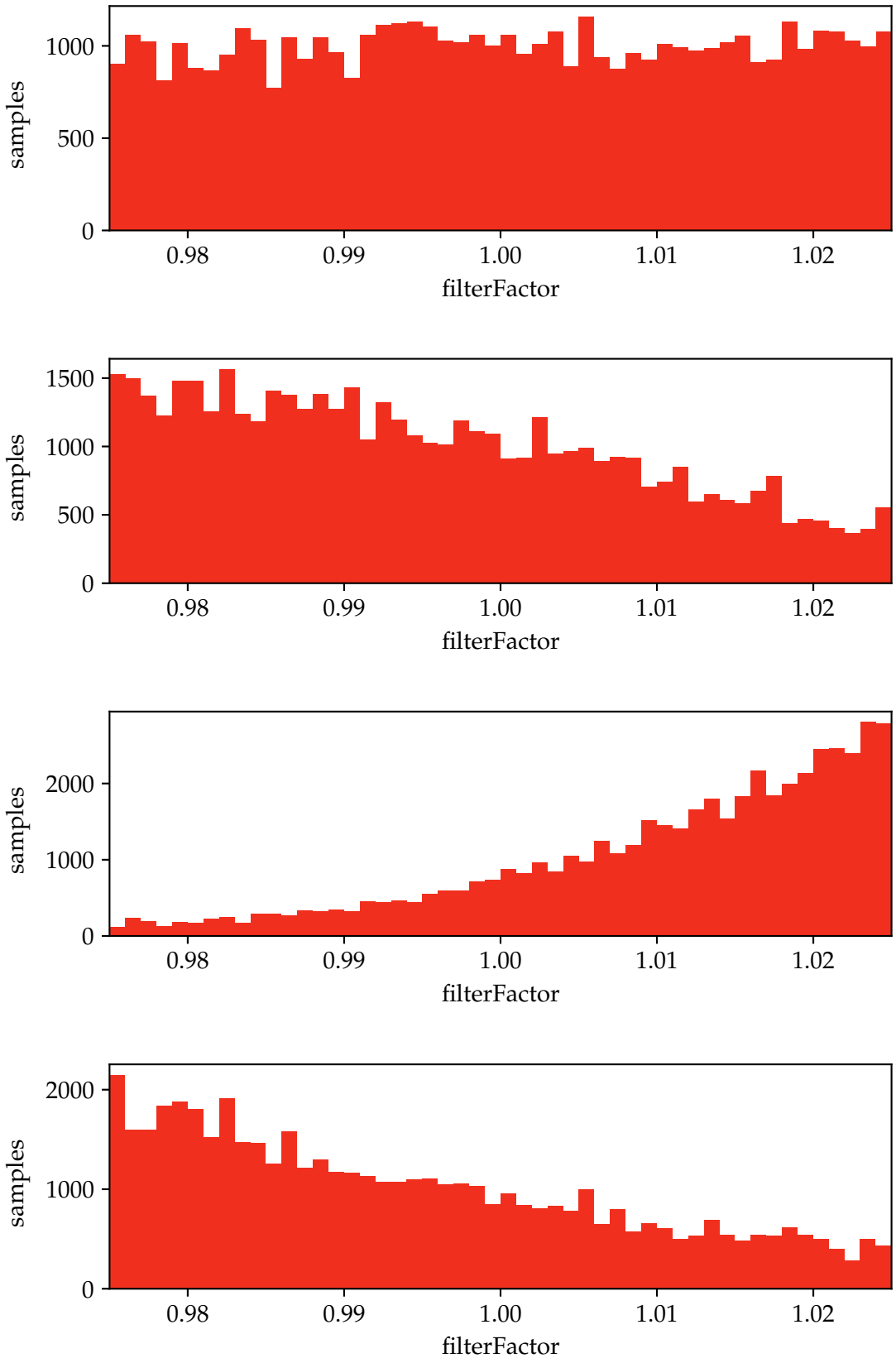

Figure 5.23: Posterior distribution of the filter variation for one volume and the four varied polychromator channels represented by a histogram of the filterFactors. The filterFactors are distributed between 0.975 and 1.25.

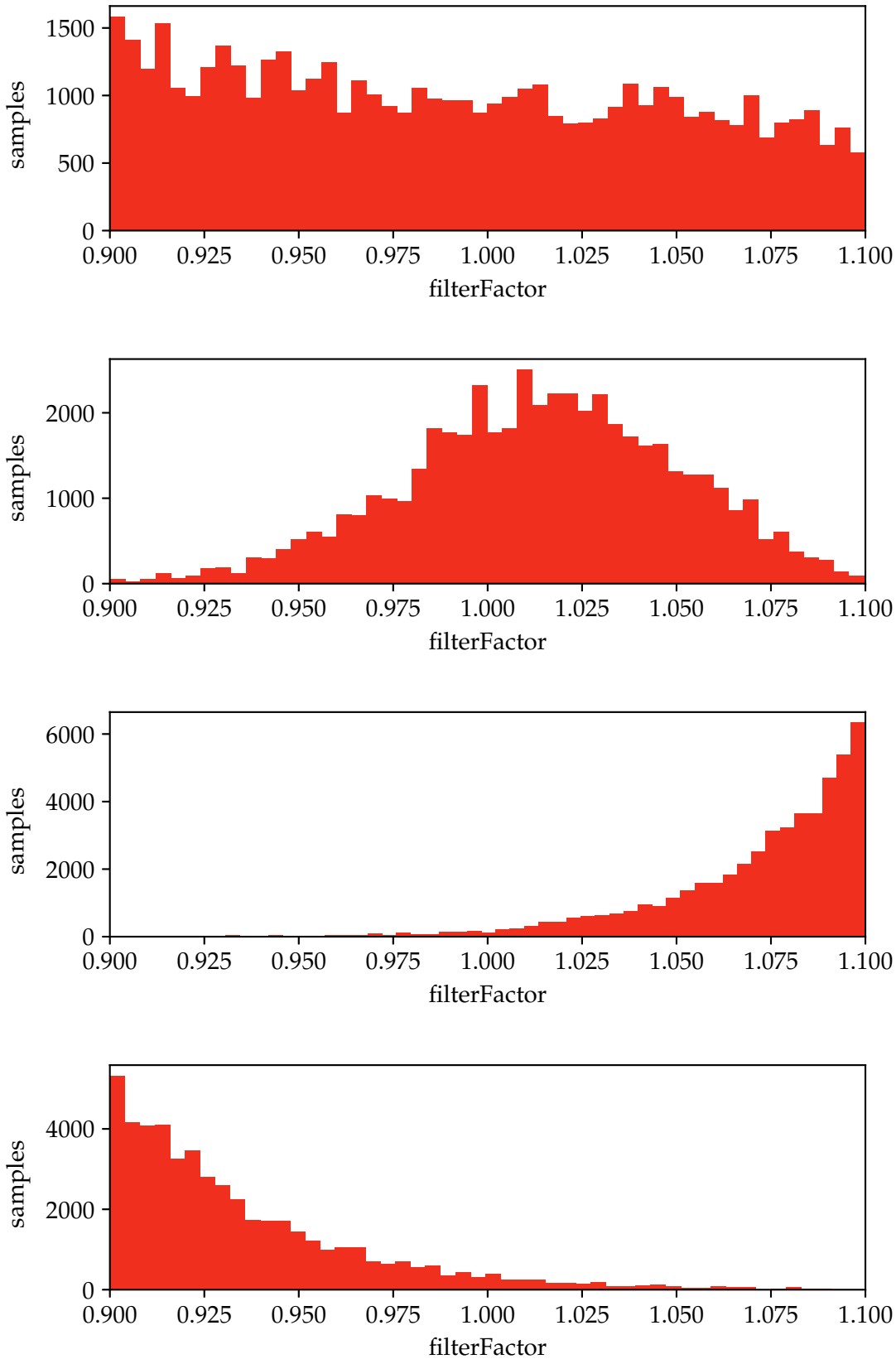

Figure 5.24: Posterior distribution of the filter variation for one volume and the four varied polychromator channels represented by a histogram of the filterFactors. The filterFactors are distributed between 0.9 and 1.1.

Instead of implementing the filterFactors as free parameters, which are uniformly distributed between 0.95 and 1.05, the filterFactors were set to fixed values and the MCMC analysis was conducted multiple times for different sets of filterFactors. Each individual filterFactor is set to one of the values 0.95, 1.00 or 1.05 and all combinations of these numbers. Mathematically speaking, this is a 4-tuple of the set $(0.95, 1.00, 1.05)$ and thus there are $3^4 = 81$ different combinations. For this analysis the disregarded number of samples was set to 5000 and the saved number of samples was also set to 5000. These smaller sample numbers can be justified by two reasons: first, because the filterFactors were set to a constant value, the number of dimensions was reduced. Second, for the further analysis only the maximum-a-posteriori values are used, which converge faster than for example the 95 % confidence intervals.
In figure 5.25 the 81 maximum-a-posteriori values for each volume (red dots) are shown, as well as the maximum-a-posteriori values and error bars previously shown (dark red crosses) in the analysis with fitted signal and filter variation (see figure 5.20). It can be seen that both kinds of analysis are generally in good agreement. It was expected that the spread of the sets would be larger, because all of the sets are treated equally, whereas when the filterFactors are varied as free parameters the different combinations are assumed according to their posterior probability. However, the spread of the sets is not significantly larger. Consequently, it cannot be concluded that the non-exploration of some parameter spaces is responsible for the small error bars.
Summarising, the marginalised posterior pdf's of the filterFactors showed little self calibrating for filterFactor one and two. FilterFactor three and four do not behave as expected. In chapter 6 it will be discussed, if that behaviour can indeed be self calibration and if the calibrations of these spectral channels were more than 10 % off. An alternative approach with fixed filter sets did not show that the behaviour of filterFactors three and four are responsible for the small 95 % confidence intervals.
After the self calibration seems not to be the source for the small error bars and the unphysical features in the profiles, a second possible source, the data preprocessing, will be cross checked in the following.
As shown before in figure 2.12, the error bars gained from fitting the scattering signal are small and may influence the MCMC, biasing the model. Also one concern was that for low signal channels noise peaks could be fitted by the preprocessing routine, resulting in artificial signal with aforementioned small error bars. For that reason, another method for preprocessing the data was investigated: the raw signal was averaged over nine pulses of the same laser. More specifically, the four laser pulses (of the same laser) before and the four pulses after the investigated pulse were taken for the average. This decreases the background noise, making it possible to directly integrate the signal, without the need of a fit. Noise peaks would be suppressed by this method, because they should average out. The averaging procedure is justified because the investigated experiment had nearly constant plasma parameters for its duration.
Similar to the preprocessing shown in figure 2.9, in figure 5.26 the average signal and the analysed raw signal of one scattering volume are shown. The error for this average integral is assumed to be the standard deviation of the background $\sigma_{\text{background}}$ integrated over the integration interval. The integration interval is chosen to be the same as the interval used to extract a single peak for the fitting routine. This error is large on purpose to explore the 'worst-case' error bars of the raw data and to have a contrast to the small error bars of the fit method.

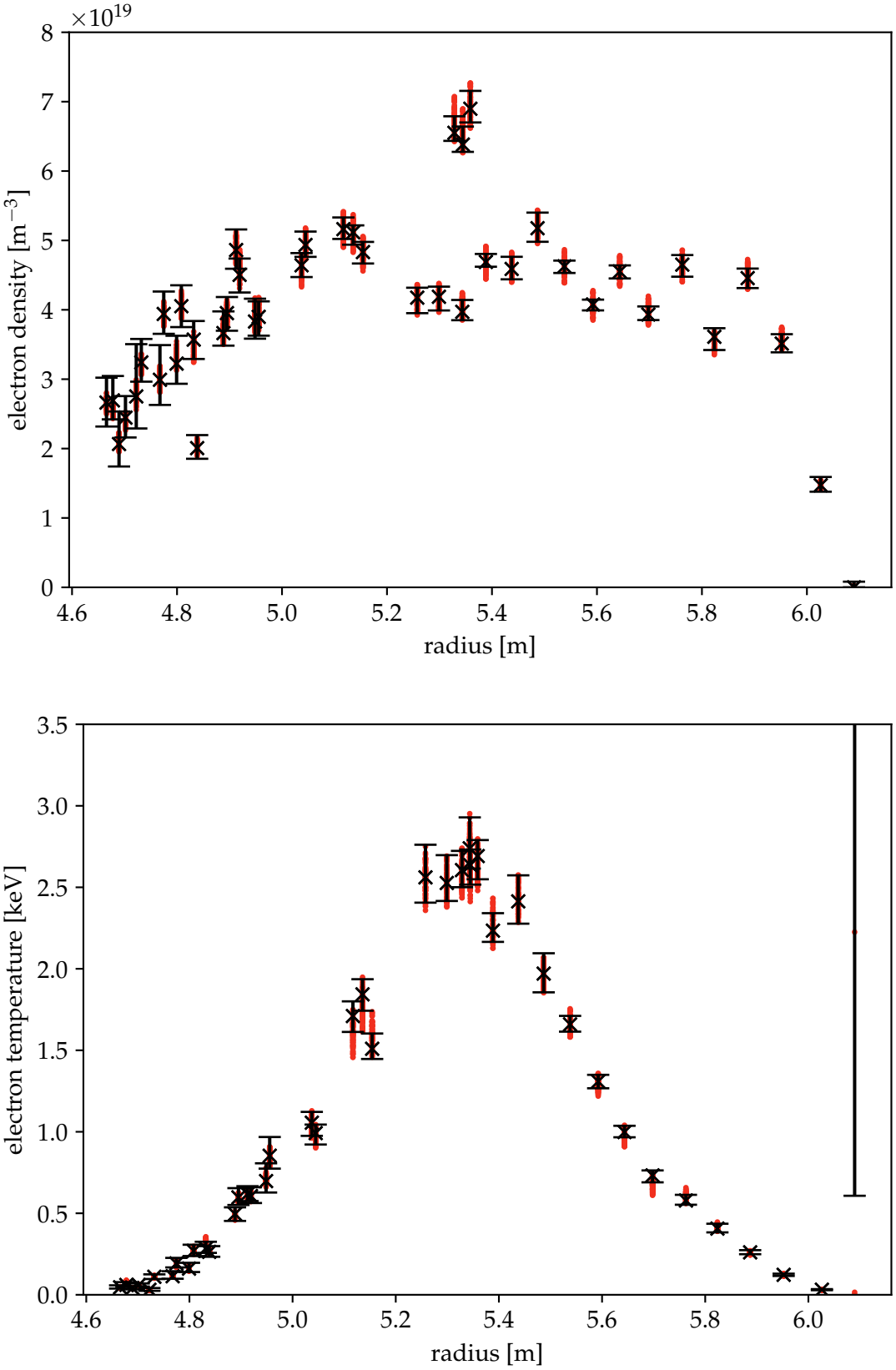

Figure 5.25: Shown are the electron density (top) and temperature (bottom) over the major radius resulting from the repeated Bayesian analysis with fixed filter sets. As dots the maximum-a-posteriori values of each filter set analysis are plotted in red. For comparing, the previously shown (see figure 5.20) maximum values with confidence intervals with variation of the filterFactors resulting from the fit method are shown in dark red as x. It can be seen that the range of the maximum-a-posteriori values of the fixed filter sets are similar to the previously calculated intervals.

The averaged raw data integrals and the corresponding error were used as the observation in the model and the results are shown without spectral calibration variation in figure 5.27 and with variation in figure 5.28. On first glance, the profile shape did not change significantly, but the error bars increased. In the following, first the comparison of both averaging results will be discussed and second the comparison between the averaging and fitting results.
To better see the impact of the filterFactors on the average preprocessing analysis, the comparison is shown in figure 5.29. Like in the fitting analysis, both results show only small differences, meaning only a small influence of the variation of the filterFactors. This leaves the conclusion that the size of the error bars of the preprocessed data do not influence the variation of the spectral calibration.
To better see the aforementioned differences between the average and fit preprocessing, both are compared in figure 5.30. The profiles are only shown with variation of the spectral calibration, but as seen previously the results without the variation are nearly identical for both average and fit. It can be seen that the 95 % confidence intervals are larger for the averaged signals. Considering the larger error bars the maximum-a-posteriori values agree with each other. As expected, the larger error of the averaged preprocessed data resulted in larger n_e and T_e error bars. Taking into account that the averaged preprocessed data error was chosen as a worst-case, the n_e and T_e error bar should be overestimated. As the fitting error seems underestimated, realistic n_e and T_e error bars would lie somewhere between both results shown in figure 5.30.
The spectral calibration error analysis was conducted in the same way for two other plasma experiments which has shown similar results and can be found in appendix section C.

Summarising the results of the spectral calibration analysis, it can be stated that the variation of the filterFactors, which was implemented to include spectral calibration uncertainties, does not change the results of the analysis significantly. Two tests for the changed model were conducted. The first test was varying the filterFactors manually with fixed combinations to show if the parameter space was sufficiently explored by the MCMC. This test has shown similar results to the variation of the filterFactors as free parameters. The second test was changing the preprocessing of the data from a fitting routine to an averaging routine, which gives a larger error bar for the observations. Testing the model with and without variation of the filterFactors has shown that the larger observation error bar does increase the resulting n_e and T_e error bars, but still hardly any difference could be found between the variation and non-variation of the filterFactors. The outcomes of both tests indicate that the filterFactors were implemented correctly. This leads to the conclusion that the errors in spectral calibration cannot explain the unphysical features of the n_e and T_e profiles. A possible explanation for the appearance of the features in the profiles will be given in chapter 6.

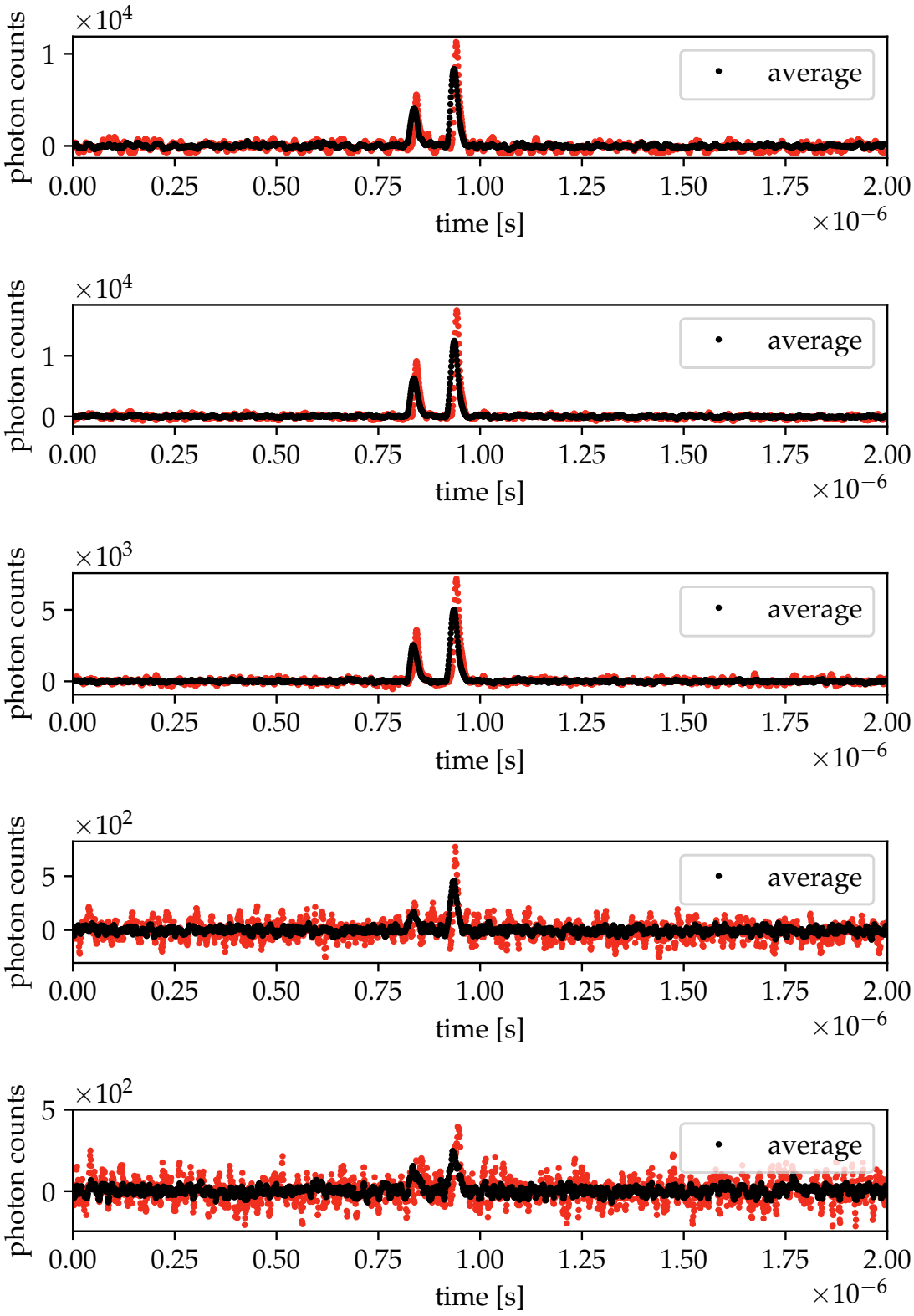

Figure 5.26: Raw and average scattering signal for one volume. Shown are the time traces of the scattering signals from one polychromator for each spectral channel (one to five from top to bottom). The first signal peak in each graph belongs to the first scattering volume and the second peak belongs to another volume, analysed with the same polychromator. The average signal from the previous and next four pulses of the same laser is shown in dark red. The integral of the average signal gives the total amount of photons detected in a given volume and spectral channel. This is used as an alternative to the fitting process.

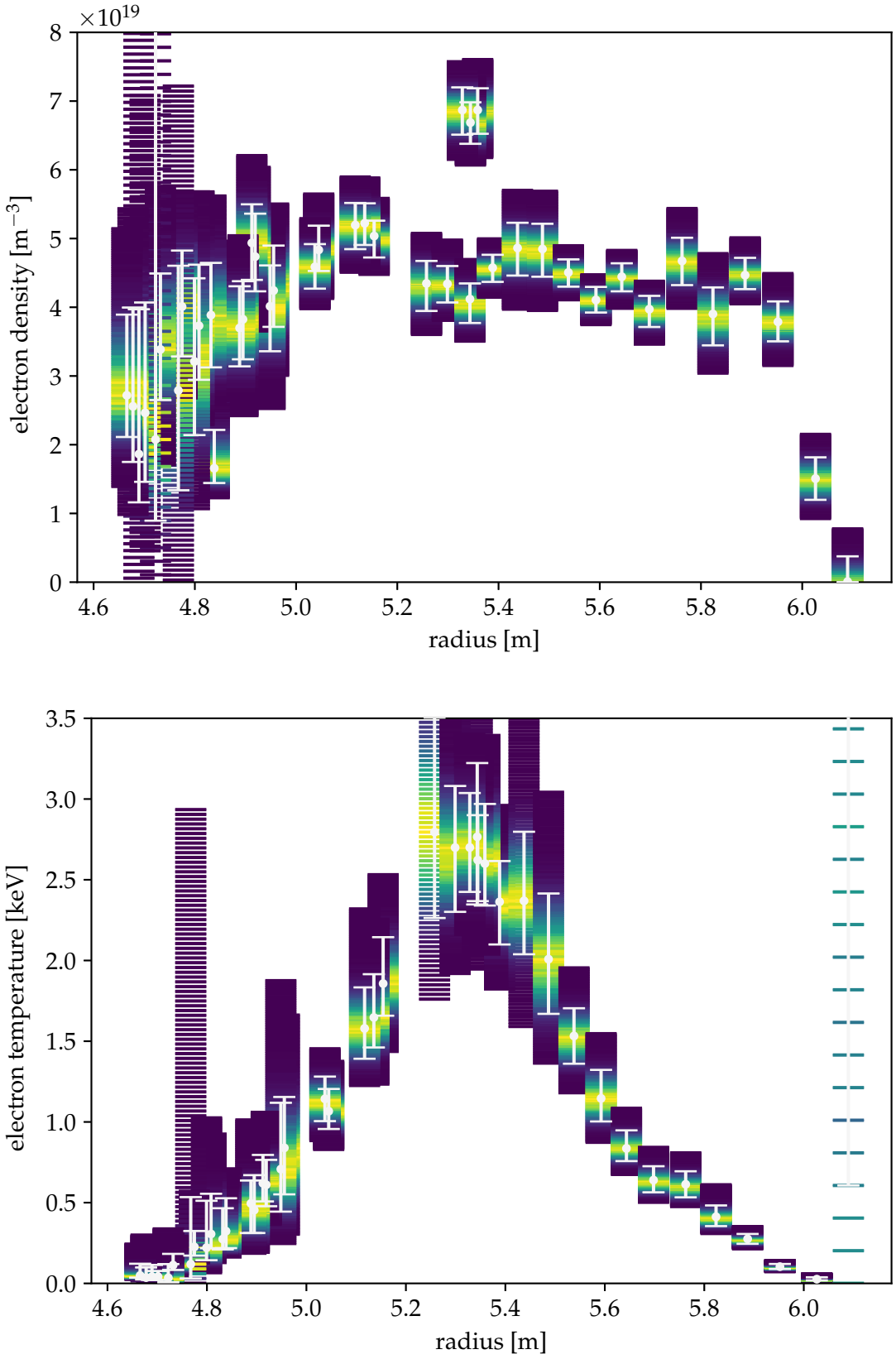

Figure 5.27: Shown are the electron density (top) and temperature (bottom) over the major radius with the alternative method of averaging the raw signal and **without** variation of spectral calibration.

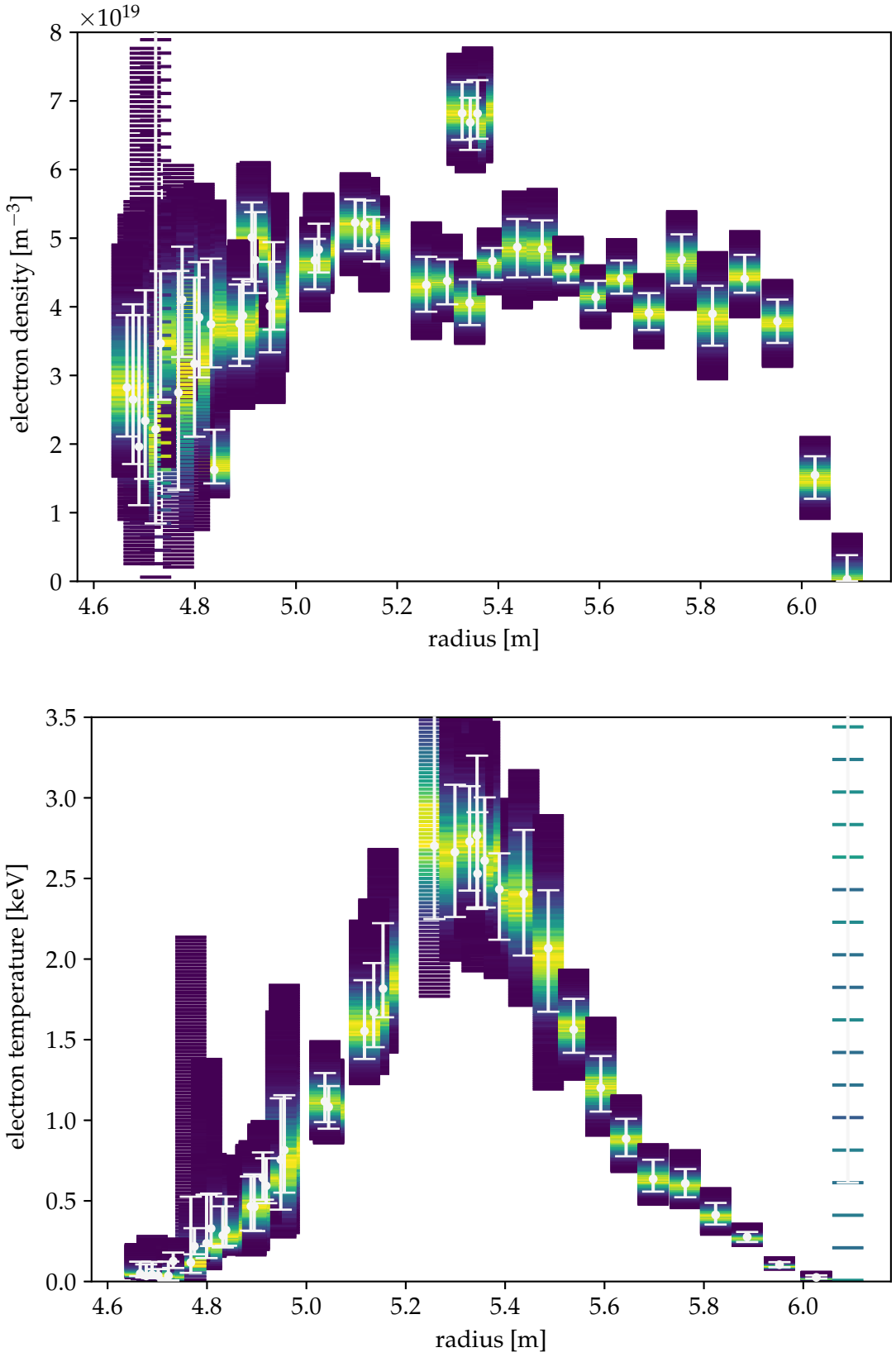

Figure 5.28: Shown are the electron density (top) and temperature (bottom) over the major radius with the alternative method of averaging the raw signal and **with** variation of spectral calibration.

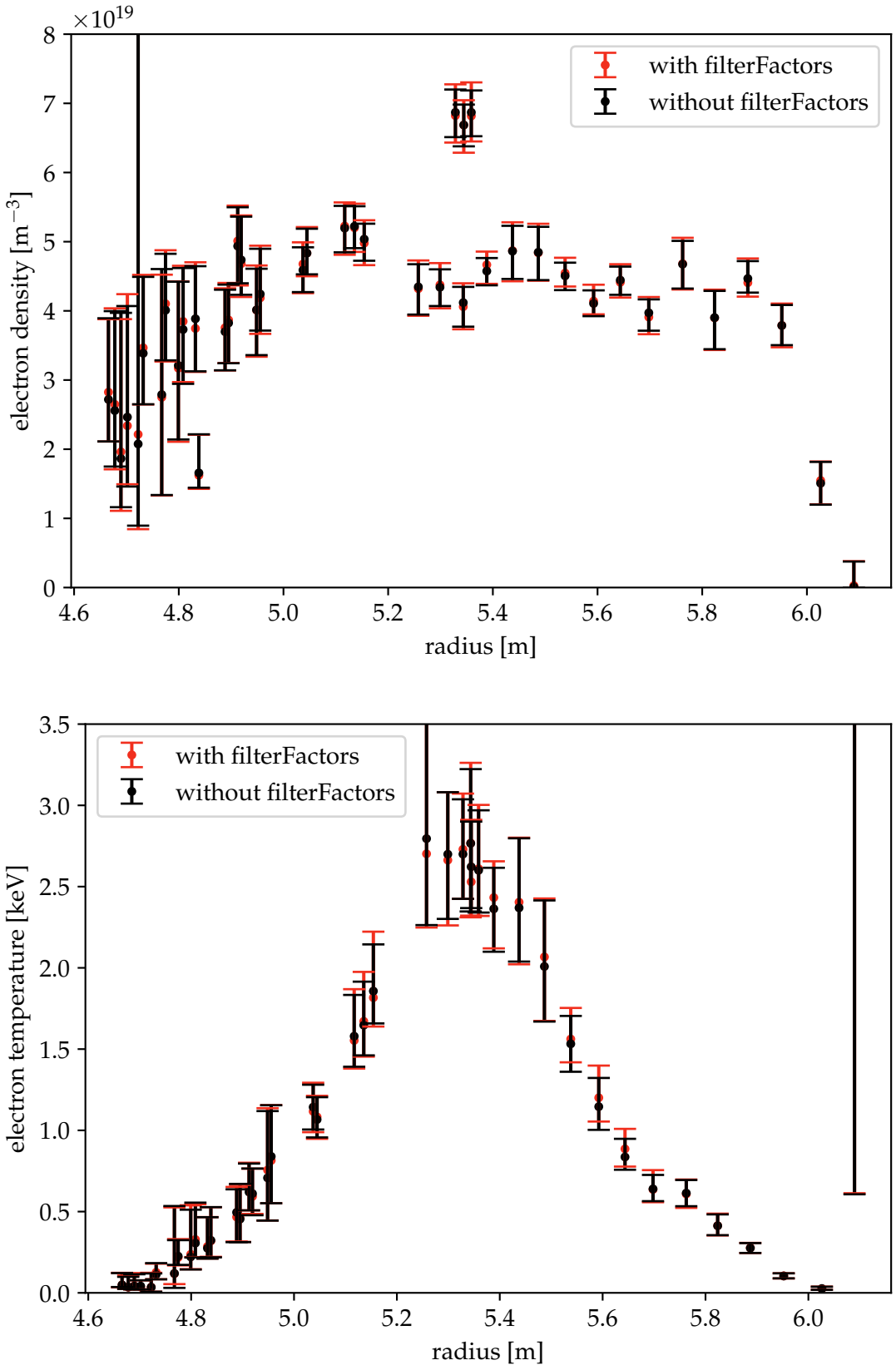

Figure 5.29: Comparison of the n_e and T_e profiles with (red) and without (dark red) variation of the spectral calibration for the averaged signals.

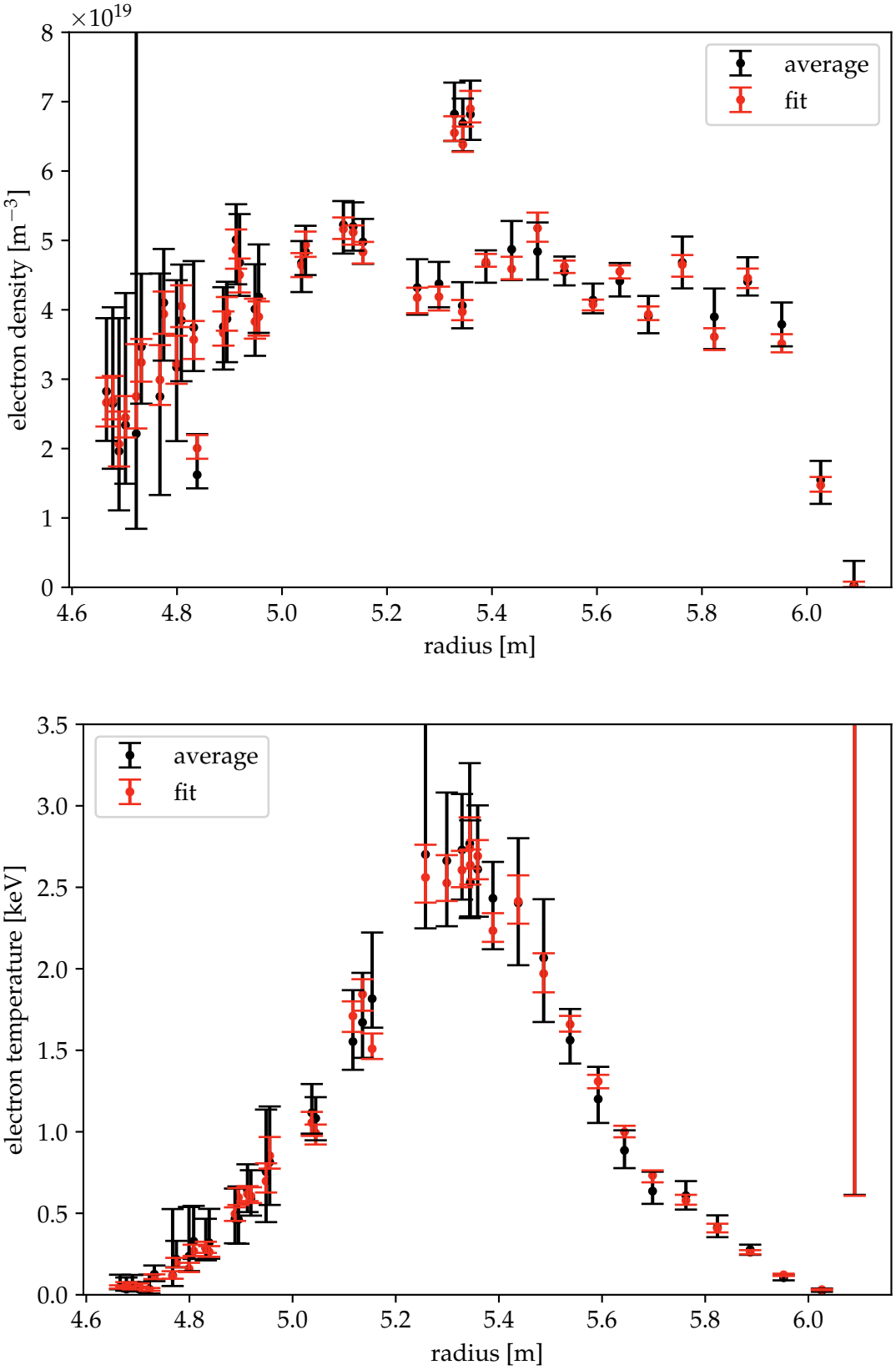

Figure 5.30: Shown are the electron density (top) and temperature (bottom) over the major radius with fitted raw data (red) and averaged raw data (dark red) **with** variation of the spectral calibration. It can be seen that the error bars of the averaged signal are larger than those of the fitted data.

6 DISCUSSION

In the course of this thesis, two systematic errors of the Thomson scattering diagnostic were investigated: the influence of misalignment of the lasers and the influence of errors in spectral calibration. The former analysis has shown a significant influence on the measured electron density, whereas the latter analysis yielded no significant influence on the derived electron density and temperature.
The spectral calibration analysis with the Thomson model has been checked with two tests indicating that the reason for the unphysical features in the density and temperature profiles has to be something not yet included in the Bayesian Thomson model. One important example source of error not yet included in the model has arisen with the analysis of the laser misalignment. Indeed it has been shown that the positional fluctuation of the lasers has a significant influence on the measured electron density. This means that these positional fluctuations influence each individual measurement and should be included in the Bayesian Thomson model or should be compensated by *positional calibrations*. Moreover, it can be assumed that the positional fluctuations of the lasers were also present while calibrating. As the absolute calibration is the result of averaging over many laser pulses, this means that the resulting absolute calibration factors are averaged over multiple laser positions. The analysis indicates, that also in the absolute calibration, different laser positions should result in different calibration factors. Hence, the averaged calibration factor is bound to be faulty for many laser pulses (laser positions). This could even lead to the calibration factor for a volume being too small or to big for most laser pulses, when the laser was positioned at the edge of a volume. This could in turn lead to specific volumes measuring higher (or lower) densities for most laser pulses and could explain for example the three centre volumes (seen in figure 5.20) always having a higher density than the surrounding volumes.
Another point for discussion arose by analysing the marginalised posterior distribution of the spectral calibration factors (filterFactors; see figures 5.22 - 5.24). It has been observed that some filterFactors tend to mostly assume the extreme values. The subsequent analysis with fixed filter sets did not yield any evidence that this behaviour is an artefact of the model. One conclusion could be that the model is trying to self-calibrate, but some spectral channel calibrations are more than 10 % off. A possible cause for that could be the spectral calibration method with the diffuse scattering plate. This plate is not placed in the same position as the scattering volumes, but is placed closer to the glass fibres. As this changes the scattering geometry, it could lead to changing the étendue. The étendue is dependent on the emitting area and during the spectral calibration, the scattering plate is placed close to the collection optics. The area should then be defined by the collection optics' aperture. This area is projected onto the diodes placed behind the spectral filters and the laser pulse energy is measured. During the plasma experiment, the emitting area is defined by the cross section of the laser with the plasma, which is then projected by the collection optics onto the diodes. If this area is different from the one during calibration, the étendue changes and might lead to an off-set spectral calibration. As an example, if during a plasma experiment the area of the diode projected through the collection

optics onto the scattering volume is larger than the emitting area than the diode is not fully 'filled'. However, during calibration the emitting area can be assumed to match the projected diode area because the scattering plate is so close to the collection optics and thus the diode can be assumed to be fully filled. This discrepancy in emitting are and consequently étendue would lead to the aforementioned off-set in calibration. This effect can vary between spectral channels because it depends on the individual scattering geometry of each channel. Additionally, if the diodes sensitivity were non-linear in space, this could increase the effect because then it is also relevant where the smaller emitting area overlaps with the diode area. If the spectral channels indeed have a varying off-set, can be tested in the future, by using an alternative calibration measurement with an OPO (optical parametric oscillator). This OPO is a wavelength tunable laser, which can use the same beam path as the Thomson lasers, thus ensuring the same scattering geometry. Scott et al. have shown at W7-X that using an OPO and Rayleigh scattering at different gas pressures, can give absolute and spectral calibration measurements [33]. As the study was a proof-of-principle, the OPO measurement still has to be properly implemented. However, a comparison with the present calibration methods seems promising and might give answers to open questions that came up during this thesis.

7

SUMMARY AND CONCLUSIONS

To find reasons for unphysical features in the electron density and temperature profiles measured by the Thomson scattering diagnostic, and to obtain more realistic error bars, the systematic errors of laser misalignment and spectral calibration were investigated.
The analysis of the laser misalignment was conducted in two parts: intentional misalignment and alignment fluctuations. The intentional misalignment was conducted on a series of plasma experiments with nearly constant plasma parameters. The horizontal misalignment was increased in step for two lasers and a third laser was kept steady for comparison. The influence of the misalignment was investigated for the mean electron density (averaged over the plasma experiment duration) as well as the relative variation of the density measurement. Both parameters showed a dependence on the horizontal misalignment. For one laser an optimal alignment could be found with this method. The other laser showed that a one dimensional (only horizontal) treatment is not sufficient because angular misalignment could also influence the beam path. This has to be kept in mind for the further laser alignment.
An alignment margin of 4 mm was found to limit the experimental error of n_e to less than 10 %. It should be kept in mind that this range is measured at the entrance Brewster window of the plasma vessel and not in the vessel, where the scattering volumes are located. The analysis has shown a strong impact of the laser position on the profile shape. This leads to the the conclusion that the laser alignment is a crucial factor in obtaining reliable electron density profiles. For the third laser it was shown that it is possible to keep the mean position of a laser stable through a range of experiments.
Because of the impact of the alignment on the measurement, the following alignment fluctuation analysis was conducted, to investigate if they are of a magnitude, sufficient to influence the measurement. The alignment fluctuations were investigated for an exemplary plasma experiment. It was observed that two lasers have stronger horizontal fluctuations than the third. Similar to the previous analysis, the electron density (now of single time point measurement) was compared to the respective beam positions. The alignment fluctuations are indeed of a magnitude to sufficiently influence the measurement. As a consequence of these alignment fluctuations and their impact on the measurement, the electron density profile shape can vary between time points, depending on the respective beam position of the laser. As a counter measure, the absolute calibration could be performed for different beam positions, enabling a correction of the effect.
As mentioned previously, the alignment fluctuations and with them the effect on the density measurement were more pronounced for two lasers. It could be shown that air flow in the mirror boxes may cause mechanical vibrations. Various mirrors and their holders were tested in the laboratory for their stability. It was found that both *fluctuating* lasers go over the same mirrors, some of which were connected to the mirror holder by an L-shaped fitting, which was susceptible to torsion. Exchanging these fittings to more stable square-shaped ones solved the problem.

The second investigation concerned the error of the spectral calibration. Comparing several spectral calibrations has shown that they deviate in a $\pm 5\,\%$ range. Before this thesis, it was unclear if this error of the spectral calibration is responsible for the features in the electron density and temperature profiles. To include the spectral calibration error, the existing data analysis tool, which is a model based on Bayesian statistics, was extended by nuisance parameters representing the calibration error. This model was then evaluated with the Markov Chain Monte Carlo method.

The resulting change in density and temperature profiles (including error bars) is not sufficient to explain the unphysical profile features. A more detailed analysis of the nuisance parameter distributions showed a self-calibration effect. However, an alternative method (manual variation of the nuisance parameter space) without self-calibration showed similar results. To rule out the preprocessing of the raw data (fitting) as a source of error, especially for low signal-to-noise ratios, another method (averaging) was tested, also showing a small impact on the results. Thus, the source of the errors of the spectral calibration of some channels of $\pm 10\,\%$ is not known.

The wanted explanation for the profile features could be given by the inclusion of the positional fluctuations in the statistical model. This can be realised by performing a positional calibration. Another promising analysis is the alternative calibration with an optical parametric oscillator and Rayleigh scattering. This method is using the same scattering geometry as the Thomson measurement and could show if the different scattering geometry of the present calibration is the source of the spectral calibration errors.

ACKNOWLEDGMENTS

Finally, I want to give my thanks to all the people that helped me in my work for this thesis. First and foremost, I want to give my thanks to Professor Wolf and IPP for enabling me to write my thesis at Wendelstein 7-X. It has been an enriching and inspiring experience. I also want to thank Professor Wolf for his guidance and constructive advice throughout all of my work. Moreover, I want to thank Professor Breitschwerdt for taking the time to examine my thesis. My special thanks goes to Golo Fuchert who always helped me and was a very good advisor to me. Thank you for taking the time to answer my questions and for figuring out with me how to best validate, interpret and present my results. Furthermore, I want to thank Ekkehard Pasch for taking me under his wings, taking interest in my work, offering tips and tricks and giving me an overall very warm welcome. I have to say, that the few weeks during OP1.2b were very exciting for me and I want to thank all the people from the Thomson group sitting with me in the control room, explaining their work and letting me participate in this great experiment. Many thanks are also in order for Jens Meineke and Karsten Lehmann who helped me in the lab experiments and provided me with the technical details. For the computational help, I have to thank Udo Hoefel. You took so much time to help me and I really appreciate it. Also on that note, I want to thank the rest of the Minerva people for their help and instructions, particularly Sehyun Kwak and Jakob Svensson. Additionally, I want to give my thanks to Evan Scott who let me participate in his experiments and was always kind and helpful to me. One of the important things is a kind working atmosphere and I want to thank all the people who took their part in providing it for me. I want to thank Fabian Wilde who was friendly with me and introduced me to the others right at the beginning so that I never felt unwelcome. Further on that note, I want to thank all the nice people, who I shared an office with, for the nice working environment and the fruitful conversations. Jan Paul Koschinsky was always there for a walk around the 'lake' and a pleasant lunch break and I want to thank him for that. Also many thanks to all the other Ph.D. students who were always kind, easy to talk to and willing to help. There are so many people I want to thank, like Hannes Damm who helped me a lot in the beginning or Sergey Bozhenkov who helped me with his previous work,... Let's just say one final thank you to all the people of Wendelstein 7-X who helped me in one way or another to complete this thesis. In particular, I want to thank my girlfriend Annabelle Spanier, who was with me through this whole experience and was always someone I could rely on. Finally, I want to thank my family who supported me through my whole studies and made this possible in the first place.

Part V

APPENDIX

A

TECHNICAL DETAILS OF THE W7-X THOMSON SCATTERING DIAGNOSTIC

A.1 OVERVIEW

In this section an overview of the Thomson scattering system at W7-X will be given. Because the diagnostic was and is going to be upgraded between operational periods, the focus of this chapter will mainly lie in the status of the diagnostic during OP1.2b (most recent operational period). A more detailed description of the Thomson setup during OP1.1 can be found in the [21]. In general one measurement follows this order: A laser pulse is generated. It is guided over mirrors into the vessel. The plasma particles scatter light via Thomson scattering. The scattered light is collected by optics and guided to a polychromator, which measures the scattered spectrum. The remaining part of the laser pulse leaves the vessel and is dumped. Following this order the various parts of the diagnostic will be described shortly in the next sections. Afterwards a more detailed description of a mirror box which is essential for this thesis will be given.

A.2 LASERS

Three linearly polarised pulsed Nd:YAG lasers (InnoLas SpitLight 2500) with a wavelength of 1064.14 nm are in use. Each of the lasers has a repetition rate of 10 Hz. In standard operation the lasers fire alternating so that the net repetition rate of Thomson measurements is 30 Hz. The lasers have a tunable pulse energy of 0.7 J to 2.5 J and the pulse duration is about 8 ns. This gives a laser power of about 90 MW to 310 MW during a pulse. This high laser power is needed, because of the low Thomson scattering cross-section mentioned in chapter 2.5.3. The pulse diameter inside the vessel varies between about 4 mm to 9 mm and can be adjusted with a converging lens with a focal length of 4 m. Because of spatial constraints, the lasers are not located in the torus hall (of W7-X), but in a separate so-called laser room. From there the beams are guided with mirrors into the torus hall.

A.3 TORUS HALL SETUP

The setup in the Torus hall is shown in figure A.1. From the left the lasers are being guided through black tubes into the entrance mirror box. There the beams are guided through the vessel and onto the beam dump. From above two collection optics are looking at the inboard and outboard side of the plasma, respectively. Each of the collection optics consists of a set of lenses (achromatic) and a number of glass fibre bundles. Every glass fibre bundle is looking at a different position in the plasma, to gain spatially resolved electron density and temperature profiles. Further on the part of the volume seen by a specific fibre bundle that coincides with the beam path is called a scattering volume. The optic looking onto the outboard side of the vessel contains 16 fibre bundles, meaning 16 individual scattering volumes. The inboard side contains 79 fibre bundles, but only 26

are currently connected to a polychromator. The sizes of the scattering volumes vary. In general the volumes on the outboard side are larger than the volumes on the inboard side. The individual volume size was determined before the experiments by illuminating the fibre bundles from the back and projecting them on the scattering plane in the vessel.

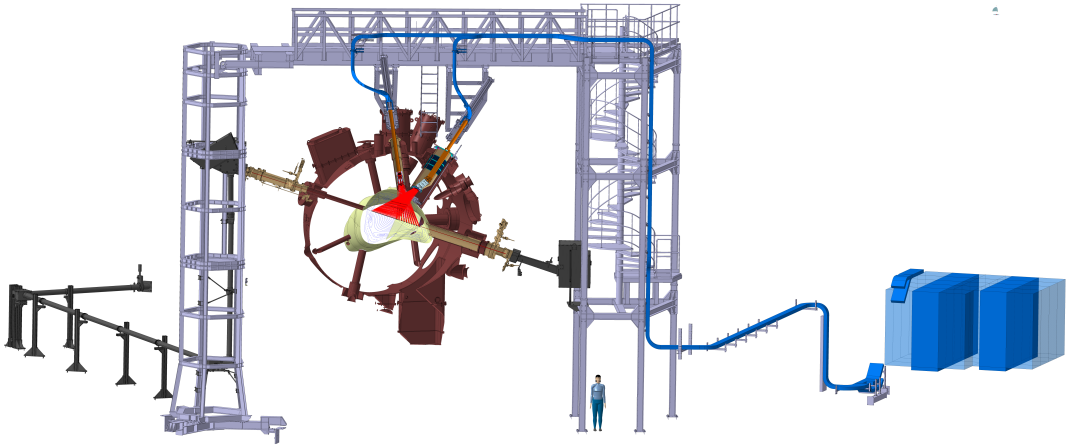

Figure A.1: Overview of the Thomson diagnostic at W7-X. The laser beams are guided from the bottom left through black tubes into the inner tower of W7-X. There the entrance mirror box guides the beam through the vessel. From above two sets of collection optics gather the Thomson scattered light. Each of the red lines represents the sight line of a glass fibre bundle, showing the spatial resolution of the diagnostic. After passing through the vessel the beams are absorbed in a beam dump located in the exit mirror box. The holding structure is called the Thomson bridge. It is mostly decoupled from W7-X to reduce vibrations of the diagnostics components.

A.4 POLYCHROMATORS

The fibre bundles leave the torus hall and go into the so-called polychromator room. There each fibre bundle ends in a polychromator. A polychromator consists of five consecutive interference filters, each equipped with an avalanche photodiode. Each diode measures the fraction of photons belonging to its filter's transmission wavelengths. To reduce stray light from the laser every filter has an optical density of six at the laser wavelength 1064 nm. As described in section 2.5 each polychromator yields five measurement points, representing the scattered Thomson spectrum. The diodes are operated in the AC-coupled mode. This represents a high pass filter with respect to the AC frequency. It gives the advantage that slowly varying background will be averaged out and only fast signals, like the Thomson scattering signal can be detected. The analogous signal of the diodes is amplified, converted into digital data and saved by a data acquisition card. Because of the short pulse duration a high sampling rate is needed. The used card operates at $1\,\mathrm{GS\,s^{-1}}$ (giga samples per second).
In principle every scattering volume needs its own polychromator. To reduce the cost,

the number of polychromators was reduced by two to three volumes sharing one polychromator. This was achieved by delaying the signals with respect to each other. The delay is caused be the use of different fibre lengths: 57 m, 77 m and 97 m. Because of the finite speed of light in the fibres, the stray light from the volume with 57 m fibre length arrives first at the polychromator, followed by the scattered light from the volume with 77 m fibre length and last is the one with 97 m fibre length. This more than halves the number of polychromators needed. Disadvantages are an increase in stray light (coming from multiple volumes instead of one) and a slight increase in analysis complexity, because the signals have to be separated afterwards. However because the delay is constant and was chosen large enough so that the signals do not overlap, this is easily done.

A.5 BEAM DUMP

The unscattered part of the laser pulses is guided out of the vessel. There a part of the pulse energy is measured by a pyroelectric laser energy monitor. The main part of the pulse energy is absorbed by the beam dump. A well designed beam dump is important to reduce stray light resulting from backscattering of the laser beam.

B

LIST OF MANUAL MISALIGNMENT EXPERIMENTS

In this section a list of the experiments conducted to investigate the influence of manual misalignment of the lasers will be given. The experiments took place on 18'th of October 2018, which was the last day of OP1.2b. At W7-X, experiments are labelled by operational date (year month day) and number of experiment of that day in the following format: *YYYYMMDD.NNN*

- 20181018.012
- 20181018.013
- 20181018.014
- 20181018.015
- 20181018.016
- 20181018.017
- 20181018.018
- 20181018.019
- 20181018.020
- 20181018.021
- 20181018.022
- 20181018.023
- 20181018.024
- 20181018.025
- 20181018.026
- 20181018.027
- 20181018.028
- 20181018.029
- 20181018.030
- 20181018.031
- 20181018.032
- 20181018.033

- 20181018.034
- 20181018.035
- 20181018.036
- 20181018.037
- 20181018.038
- 20181018.039
- 20181018.040
- 20181018.041

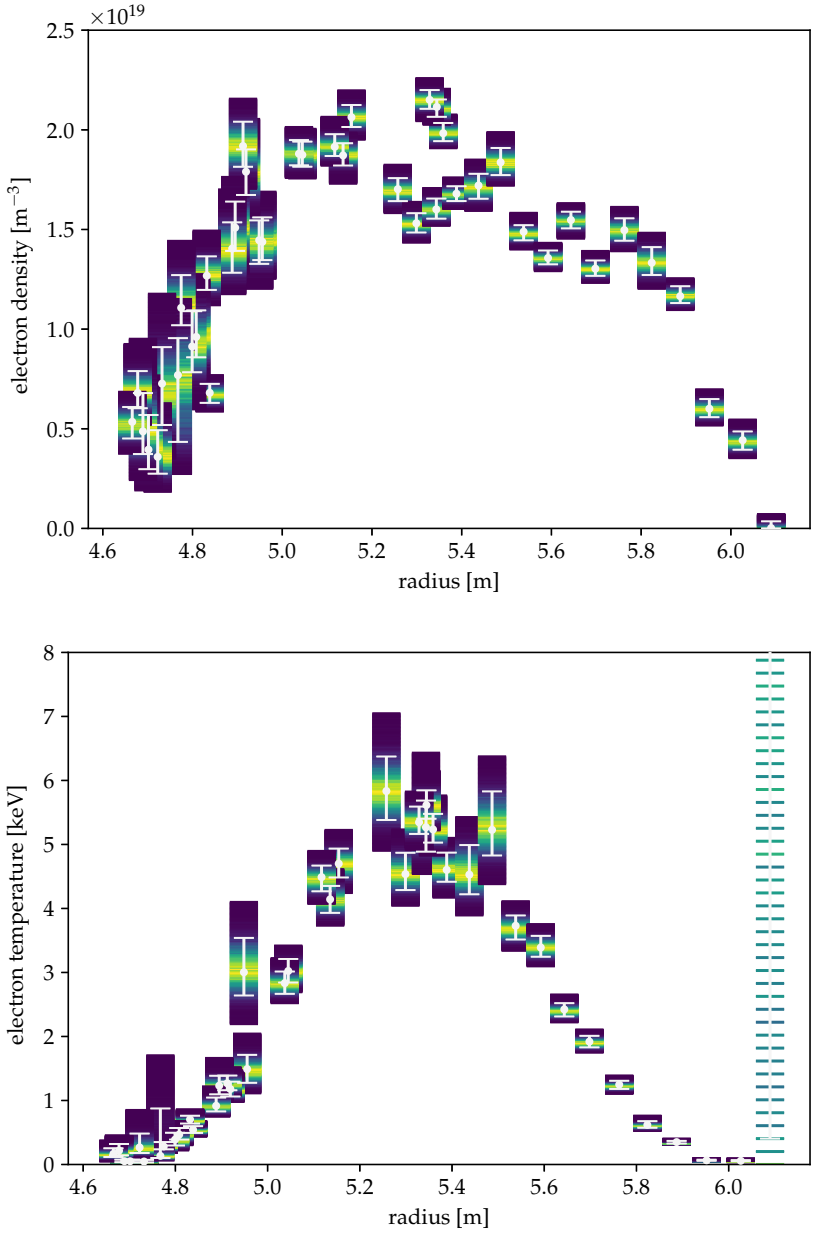

Figure C.1: Shown are the electron density (top) and temperature (bottom) over the major radius resulting from the Bayesian analysis **without** any variation of the spectral calibration for experiment 20180920.008. As dots the most likely values (maximum a posteriori) are plotted with the 95 % confidence interval as error bars. Underneath each dot, a colour coded histogram of the MCMC samples is shown. This colour coded histogram represents the posterior distribution, resulting from the Bayesian analysis. The most likely value and the 95 % confidence interval are calculated from this distribution.

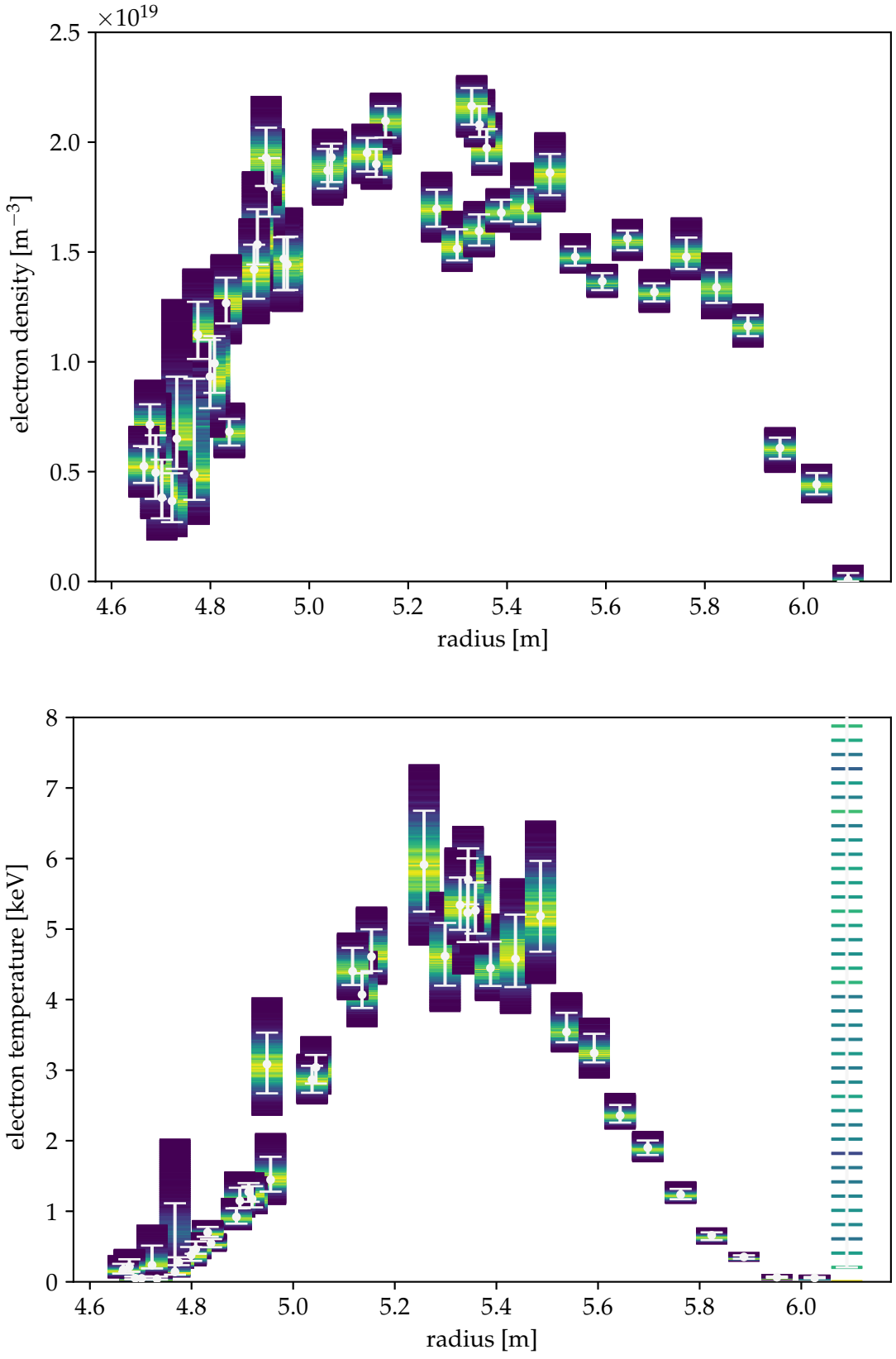

Figure C.2: Shown are the electron density (top) and temperature (bottom) over the major radius resulting from the Bayesian analysis **with** variation of the spectral calibration for experiment 20180920.008. As dots the most likely values (maximum a posteriori) are plotted with the 95 % confidence interval as error bars. Underneath each dot, a colour coded histogram of the MCMC samples is shown. This colour coded histogram represents the posterior distribution, resulting from the Bayesian analysis. The most likely value and the 95 % confidence interval are calculated from this distribution.

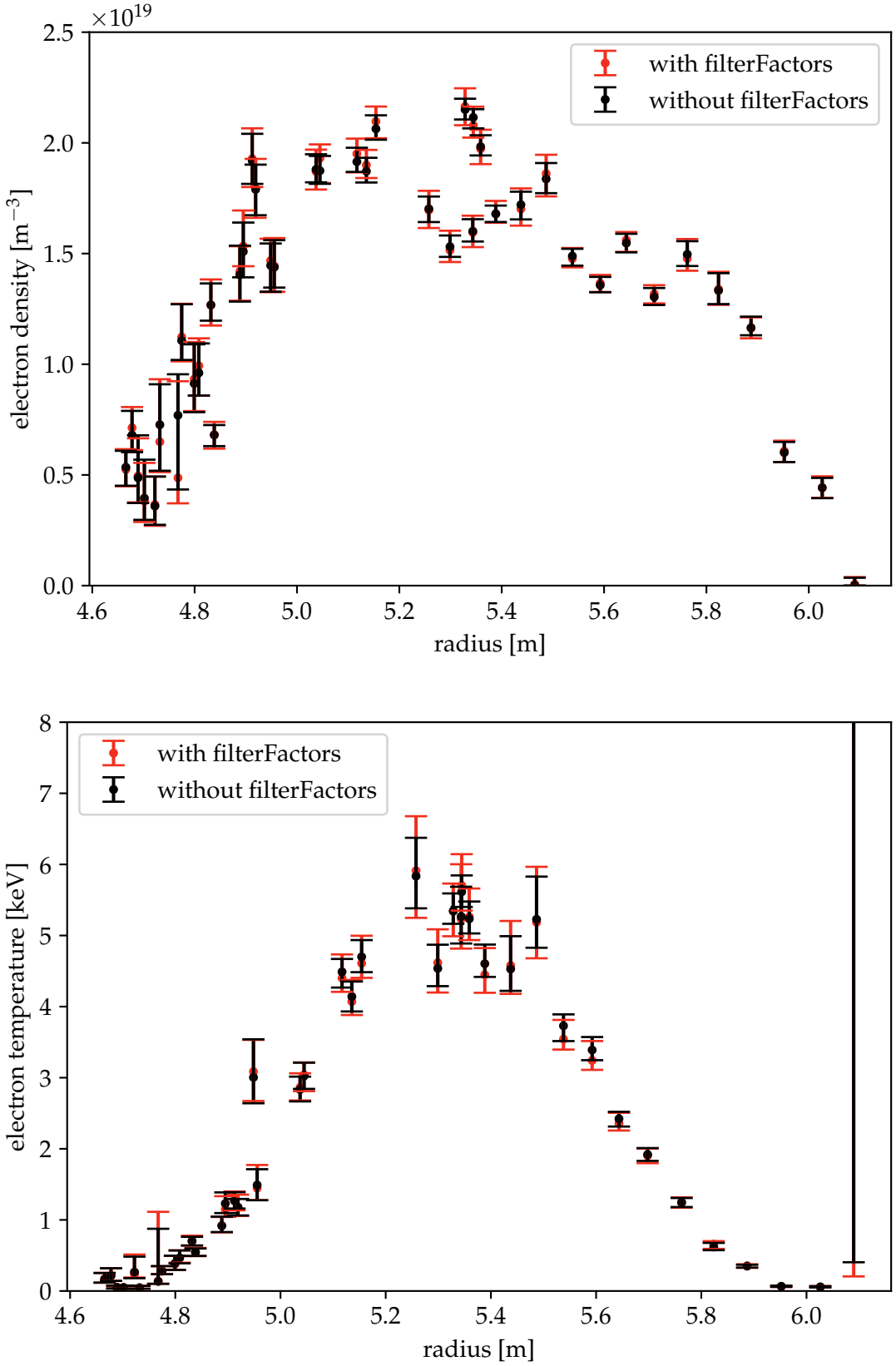

Figure C.3: Shown are the electron density (top) and temperature (bottom) over the major radius with (red) and without (dark red) variation of the spectral calibration for experiment 20180920.008. It can be seen, that the results are almost the same. The variation of the filterFactors seems to only slightly increase the error bars.

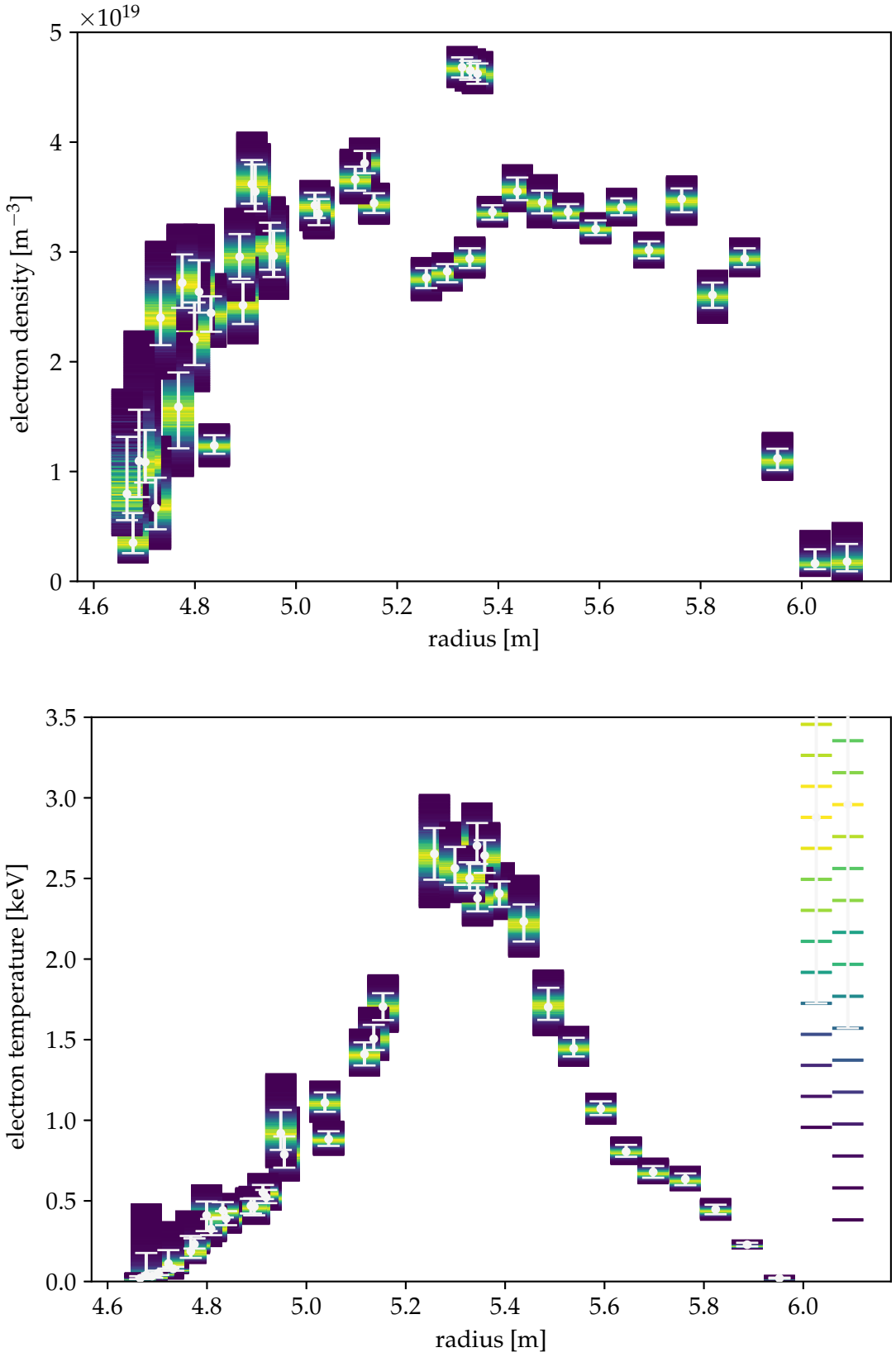

Figure C.4: Shown are the electron density (top) and temperature (bottom) over the major radius resulting from the Bayesian analysis **without** any variation of the spectral calibration for experiment 20180927.008. As dots the most likely values (maximum a posteriori) are plotted with the 95 % confidence interval as error bars. Underneath each dot, a colour coded histogram of the MCMC samples is shown. This colour coded histogram represents the posterior distribution, resulting from the Bayesian analysis. The most likely value and the 95 % confidence interval are calculated from this distribution.

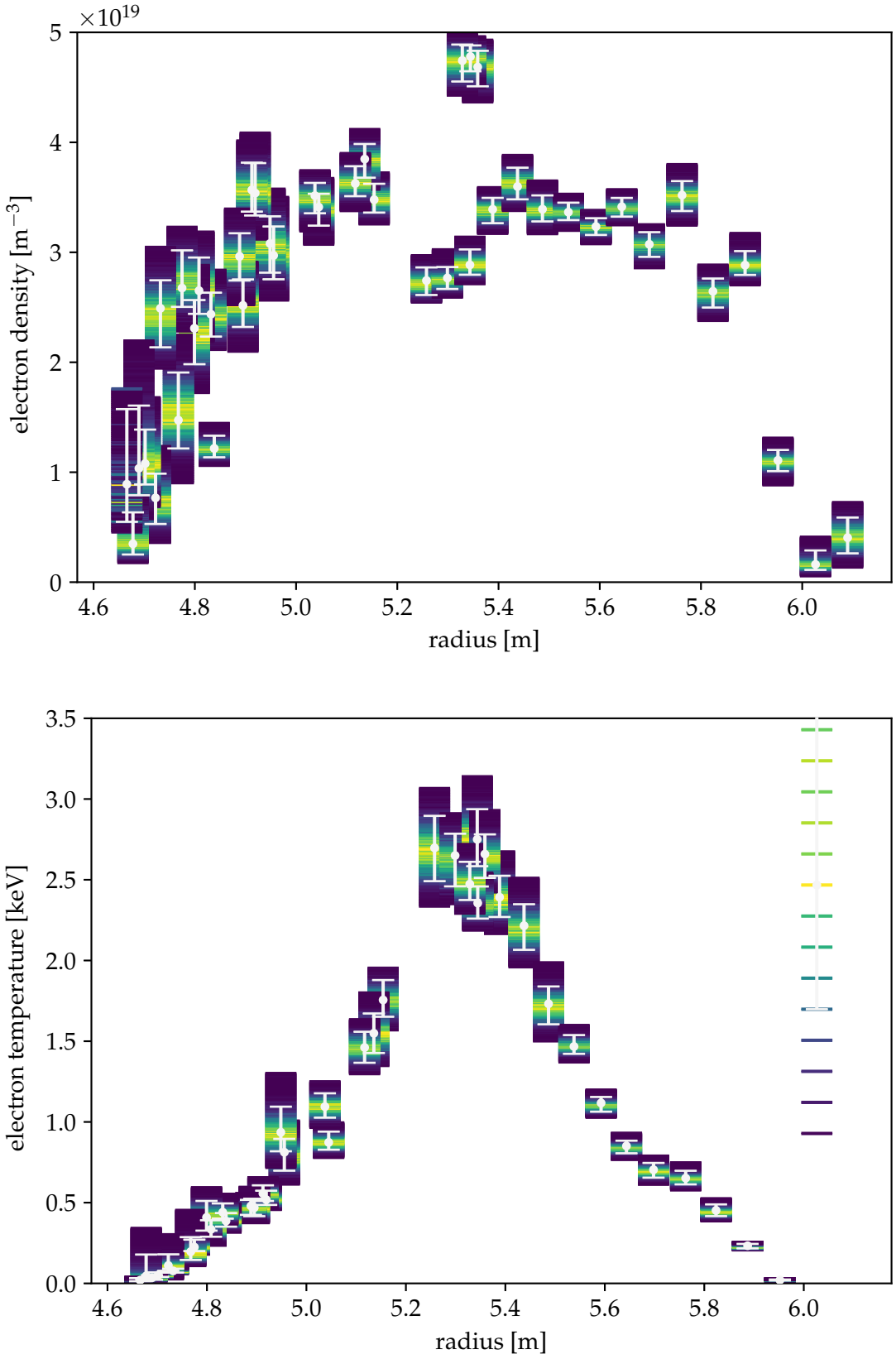

Figure C.5: Shown are the electron density (top) and temperature (bottom) over the major radius resulting from the Bayesian analysis **with** variation of the spectral calibration for experiment 20180927.008. As dots the most likely values (maximum a posteriori) are plotted with the 95 % confidence interval as error bars. Underneath each dot, a colour coded histogram of the MCMC samples is shown. This colour coded histogram represents the posterior distribution, resulting from the Bayesian analysis. The most likely value and the 95 % confidence interval are calculated from this distribution.

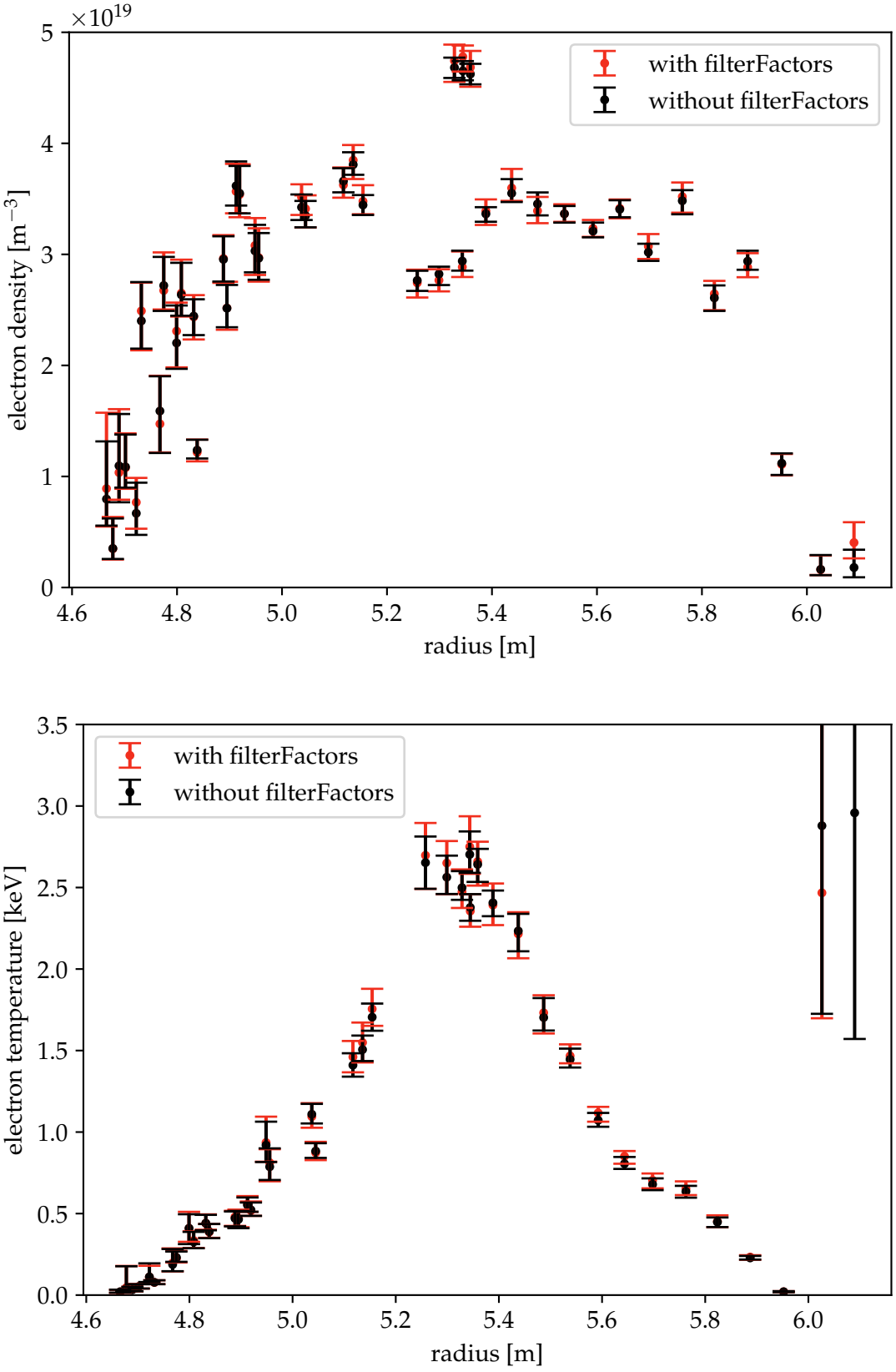

Figure C.6: Shown are the electron density (top) and temperature (bottom) over the major radius with (red) and without (dark red) variation of the spectral calibration for experiment 20180927.008. It can be seen, that the results are almost the same. The variation of the filterFactors seems to only slightly increase the error bars.

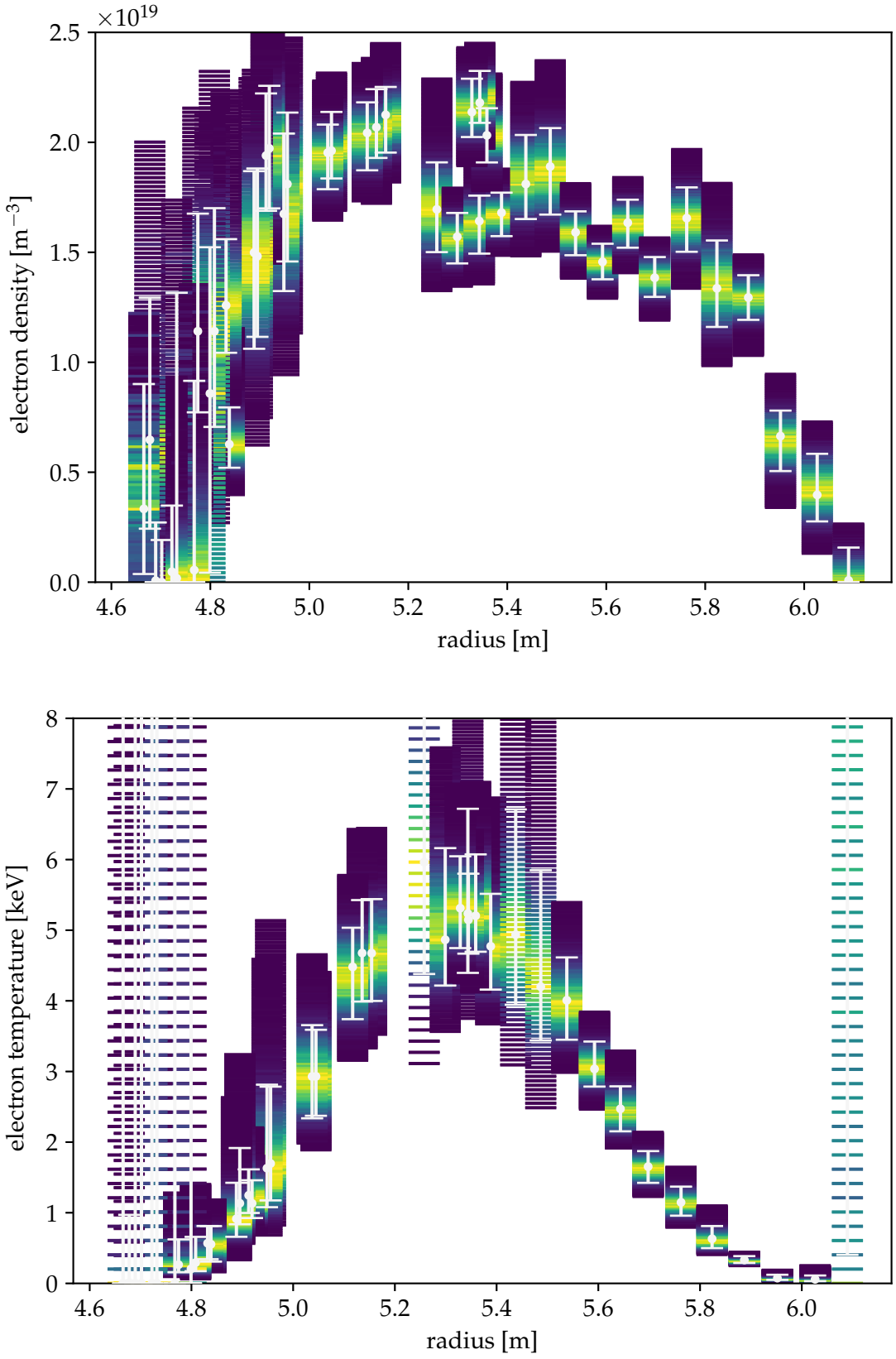

Figure C.7: Shown are the electron density (top) and temperature (bottom) over the major radius with the alternative method of averaging the raw signal and **without** variation of spectral calibration for experiment 20180920.008.

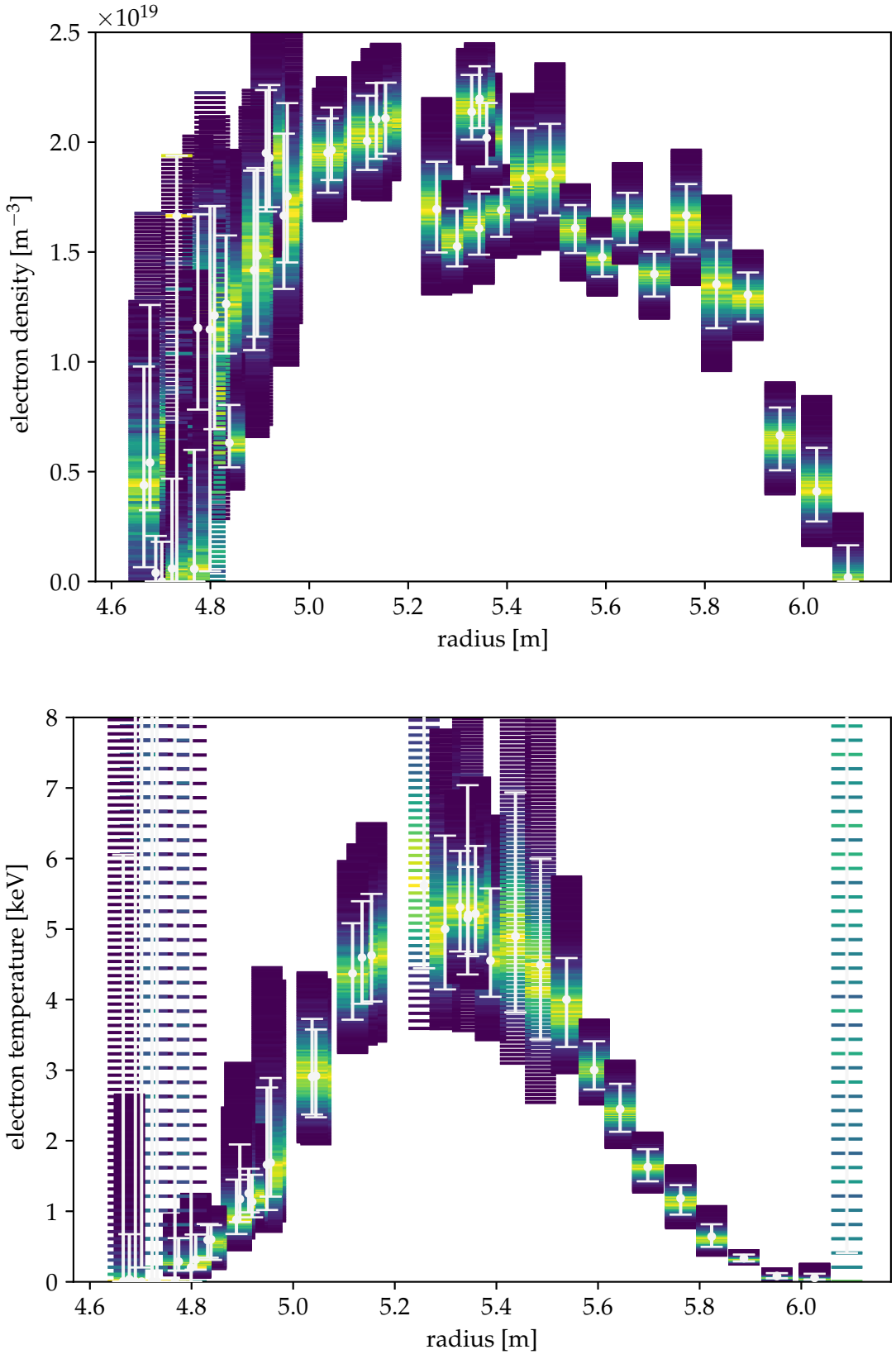

Figure C.8: Shown are the electron density (top) and temperature (bottom) over the major radius with the alternative method of averaging the raw signal and **with** variation of spectral calibration for experiment 20180920.008.

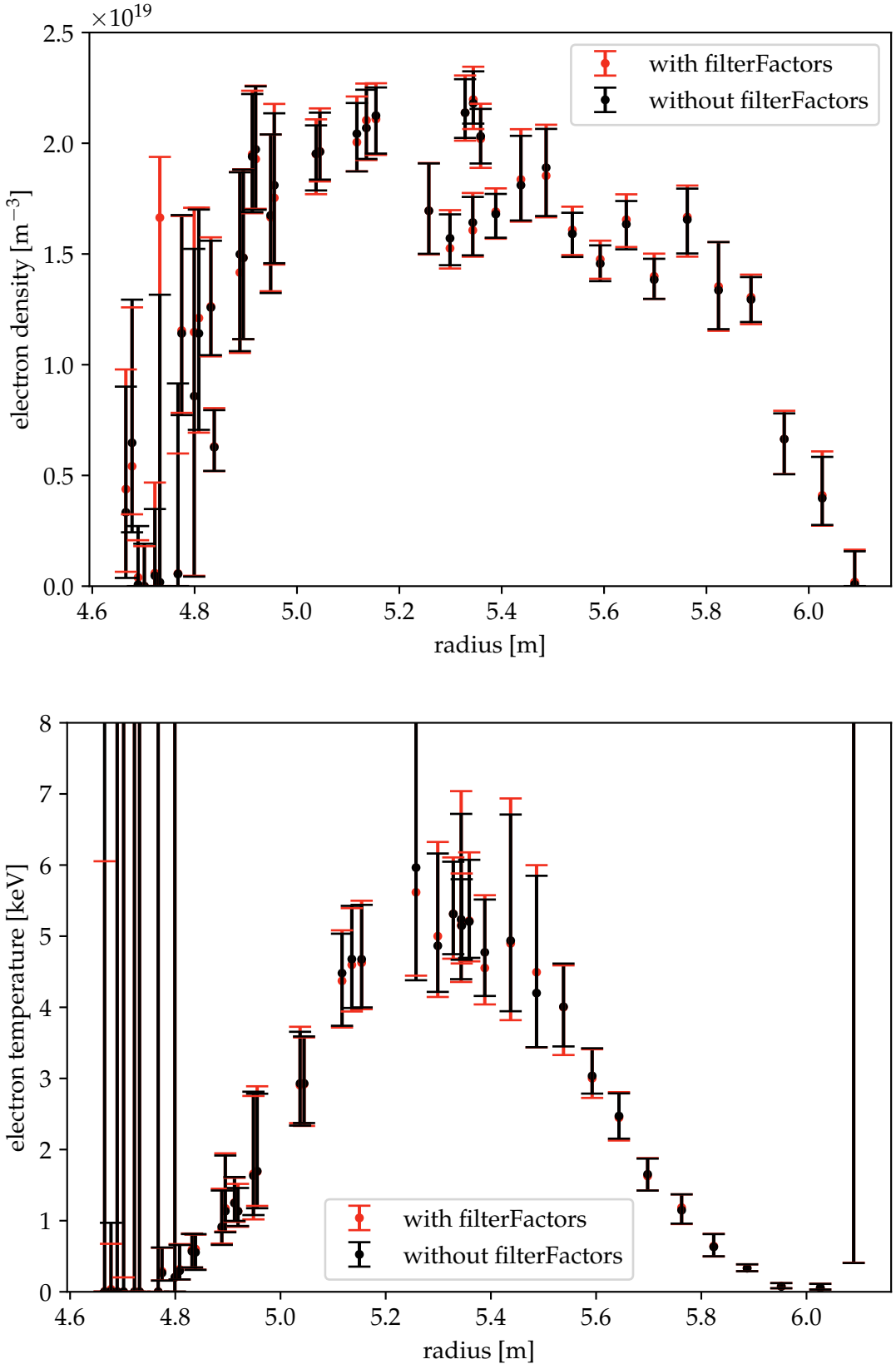

Figure C.9: Comparison of the n_e and T_e profiles with (red) and without (dark red) variation of the spectral calibration for the averaged signals for experiment 20180920.008.

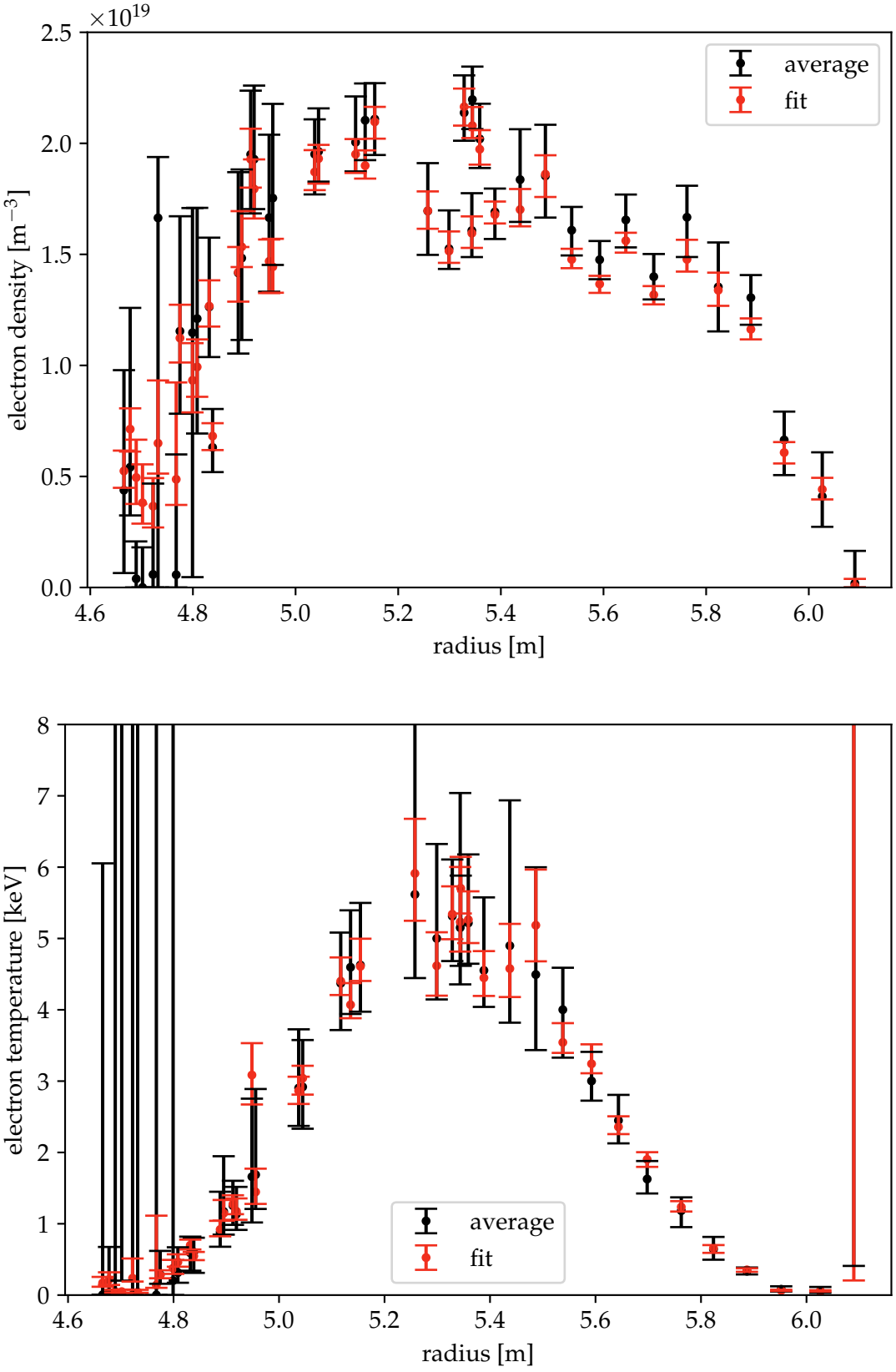

Figure C.10: Shown are the electron density (top) and temperature (bottom) over the major radius with fitted raw data (red) and averaged raw data (dark red) with variation of the spectral calibration for experiment 20180920.008. It can be seen, that the error bars of the averaged signal are larger than those of the fitted data.

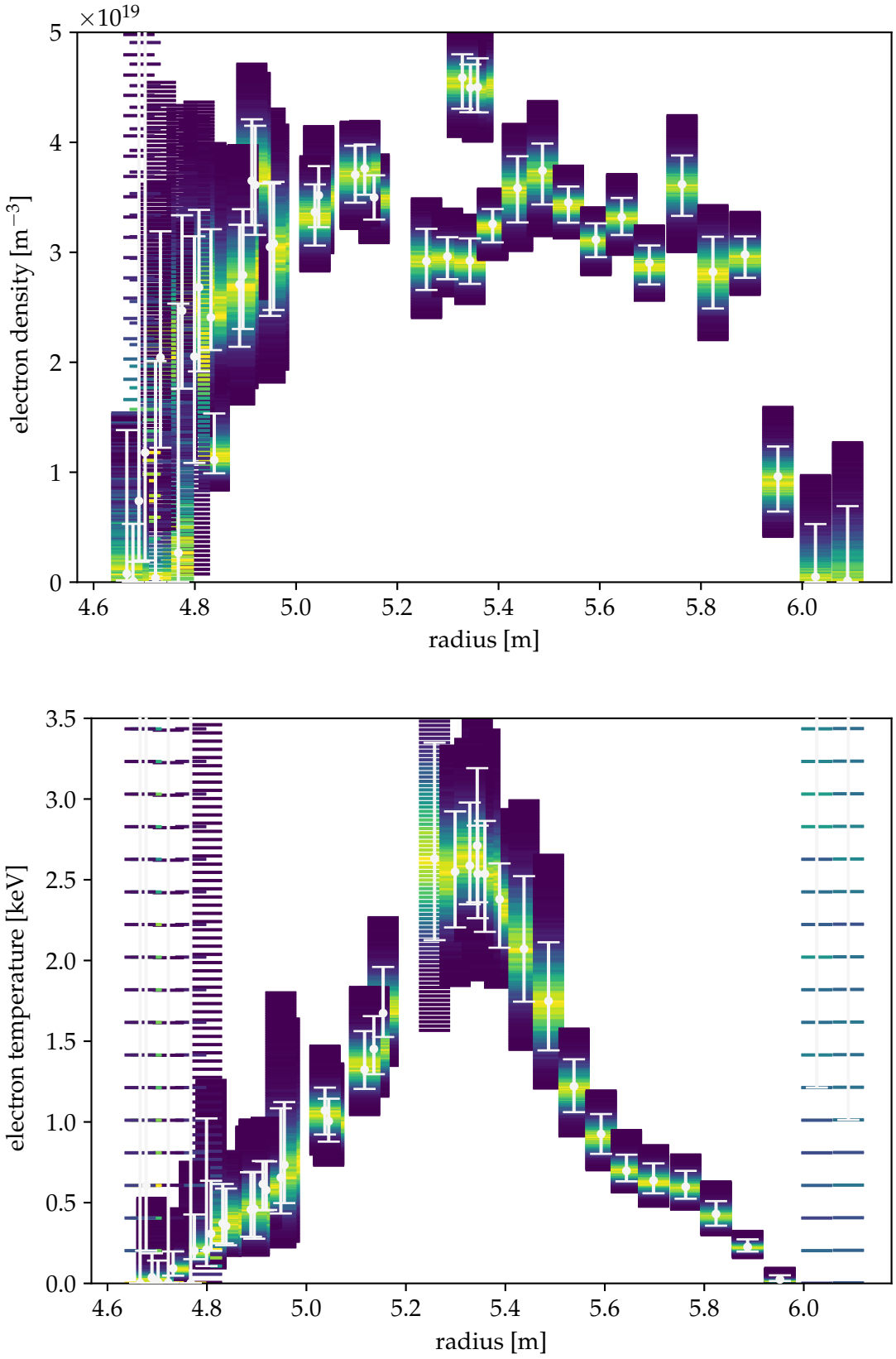

Figure C.11: Shown are the electron density (top) and temperature (bottom) over the major radius with the alternative method of averaging the raw signal and **without** variation of spectral calibration for experiment 20180927.008.

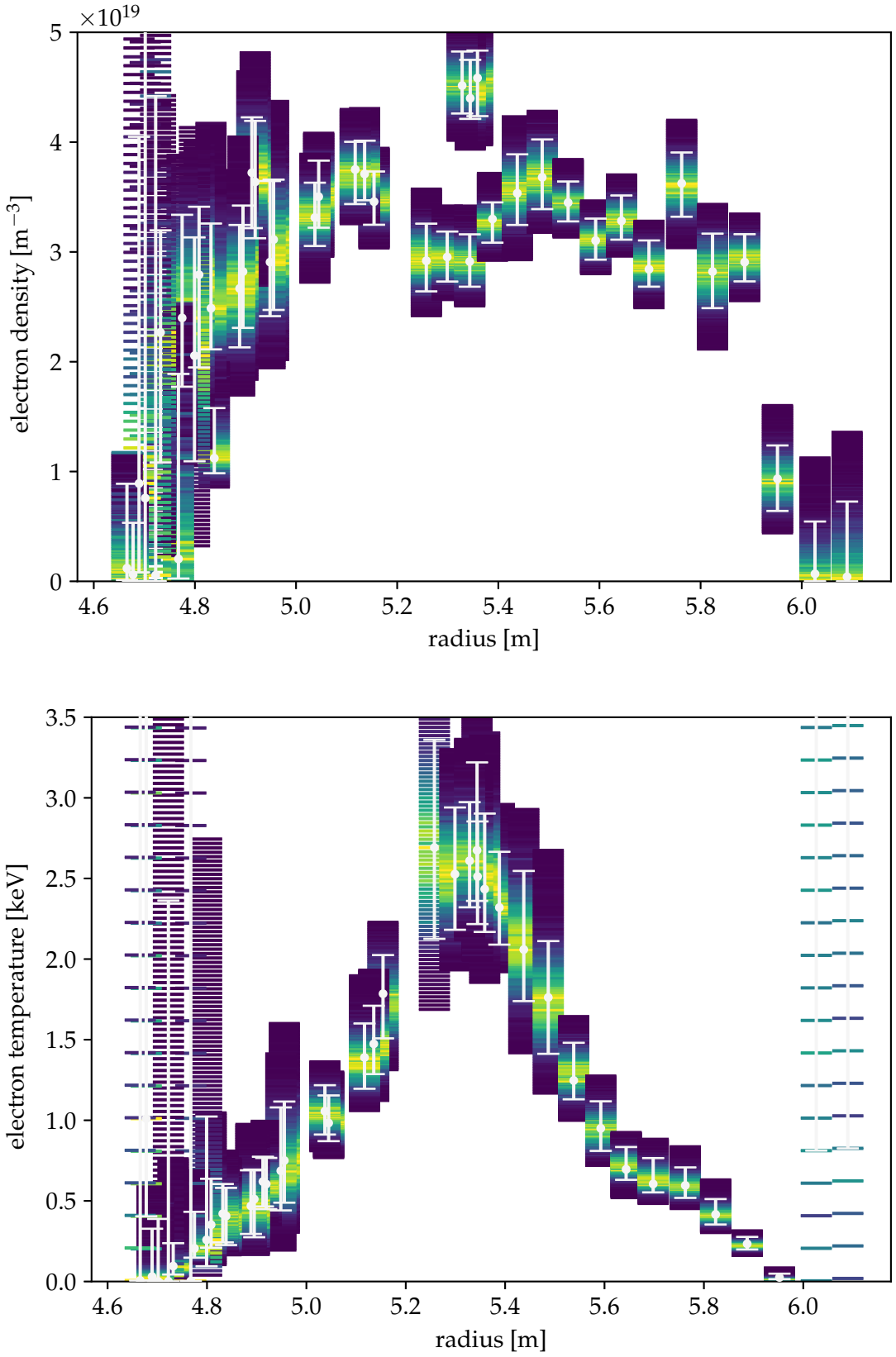

Figure C.12: Shown are the electron density (top) and temperature (bottom) over the major radius with the alternative method of averaging the raw signal and **with** variation of spectral calibration for experiment 20180927.008.

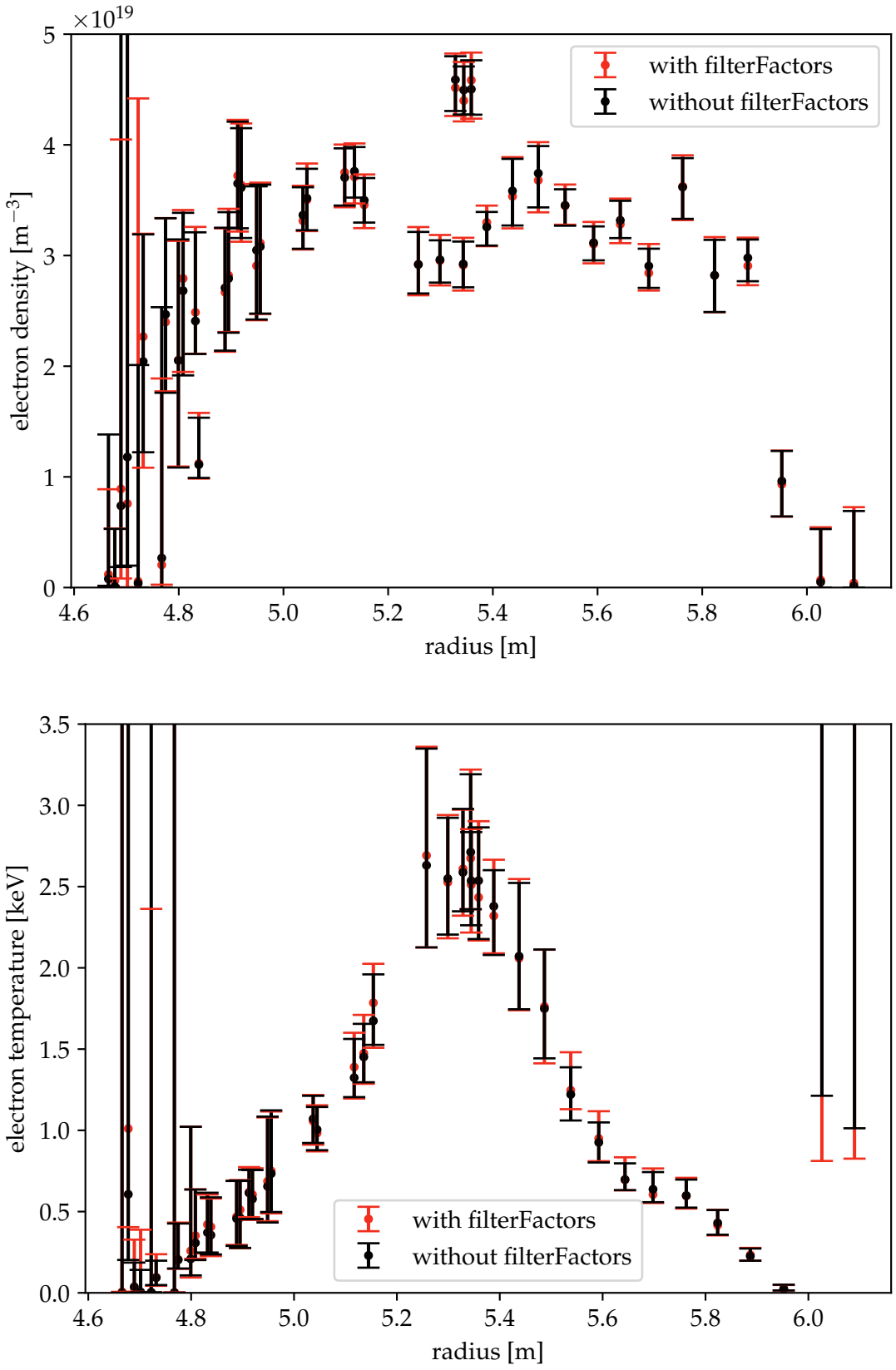

Figure C.13: Comparison of the n_e and T_e profiles with (red) and without (dark red) variation of the spectral calibration for the averaged signals for experiment 20180927.008.

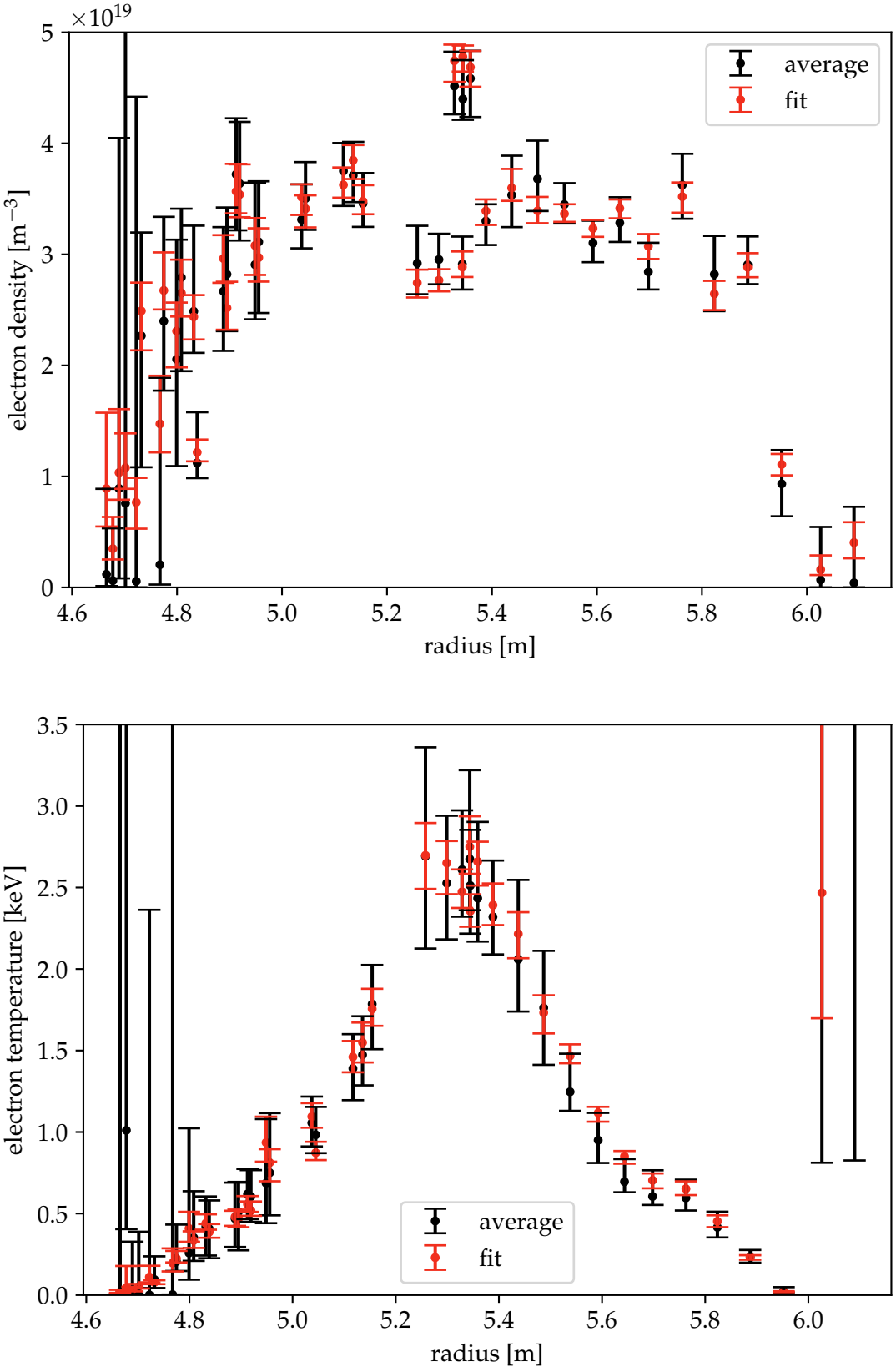

Figure C.14: Shown are the electron density (top) and temperature (bottom) over the major radius with fitted raw data (red) and averaged raw data (dark red) with variation of the spectral calibration for experiment 20180927.008. It can be seen, that the error bars of the averaged signal are larger than those of the fitted data.

BIBLIOGRAPHY

1. Milch, I. *Max-Planck-Institut für Plasmaphysik - 50 Jahre Forschung für die Energie der Zukunft* 1st ed. ISBN: 978-3-00-031750-7. https://www.ipp.mpg.de/44301/50_jahre_ipp.pdf (IPP, 2010).
2. Stix, M. *The Sun* 2nd ed. ISBN: 978-3-642-56042-2. https://doi.org/10.1007/978-3-642-56042-2 (Springer, Heidelberg, 2002).
3. Chen, F. F. *Introduction to Plasma Physics and Controlled Fusion* 3rd ed. doi:10.1007/978-3-319-22309-4 (Springer, Switzerland, 2016).
4. Piel, A. *Plasma Physics* 2nd ed. doi:10.1007/978-3-319-63427-2 (Springer, 2017).
5. Bosch, H.-S & Hale, G. Improved formulas for fusion cross-sections and thermal reactivities. *Nuclear Fusion* **32,** 611–631. doi:10.1088/0029-5515/32/4/i07 (Apr. 1992).
6. Bosch, H.-S & Hale, G. Improved formulas for fusion cross-sections and thermal reactivities. *Nuclear Fusion* **33,** 1919–1919. doi:10.1088/0029-5515/33/12/513 (Dec. 1993).
7. Stott, P. *et al. Diagnostics for Experimental Thermonuclear Fusion Reactors* 1st ed. ISBN: 978-1-4613-0369-5. doi:10.1007/978-1-4613-0369-5 (Springer, Boston, MA, 1996).
8. Raffray, A. *et al.* Breeding blanket concepts for fusion and materials requirements. *Journal of Nuclear Materials* **307-311,** 21 –30. ISSN: 0022-3115. doi:10.1016/S0022-3115(02)01174-1 (2002).
9. Wesson, J. *Tokamaks* 3rd ed. ISBN: 978-0-19-850922-6 (Oxford University Press, Oxford, 2004).
10. Wanner, M. Design goals and status of the WENDELSTEIN 7-X project. *Plasma Physics and Controlled Fusion* **42,** 1179–1186. doi:10.1088/0741-3335/42/11/304 (Nov. 2000).
11. Wolf, R. C. *et al.* Wendelstein 7-X Program-Demonstration of a Stellarator Option for Fusion Energy. *IEEE Transactions on Plasma Science* **44,** 1466–1471. doi:10.1109/TPS.2016.2564919 (Sept. 2016).
12. Pedersen, T. S. *et al.* First results from divertor operation in Wendelstein 7-X. *Plasma Physics and Controlled Fusion* **61,** 014035. doi:10.1088/1361-6587/aaec25 (Nov. 2018).
13. Hirsch, M *et al.* Major results from the stellarator Wendelstein 7-AS. *Plasma Physics and Controlled Fusion* **50,** 053001. doi:10.1088/0741-3335/50/5/053001 (Mar. 2008).
14. Nuclear Fusion Status and Prospects. *Fusion Basics.* https://www.ipp.mpg.de/986351 (Jan. 2019).
15. Clery, D. Twisted logic. *Science* **350,** 369–371. doi:10.1126/science.350.6259.369 (2015).
16. Cedillos-Barraza, O. *et al.* Investigating the highest melting temperature materials: A laser melting study of the TaC-HfC system. *Scientific Reports* **6.** doi:10.1038/srep37962 (Dec. 2016).

17. Carlstrom, T. N. *et al.* Design and operation of the multipulse Thomson scattering diagnostic on DIII-D (invited). *Review of Scientific Instruments* **63,** 4901–4906. doi:10.1063/1.1143545 (1992).

18. Narihara, K. *et al.* Design and performance of the Thomson scattering diagnostic on LHD. *Review of Scientific Instruments* **72,** 1122–1125. doi:10.1063/1.1319368 (2001).

19. Pasqualotto, R. *et al.* High resolution Thomson scattering for Joint European Torus (JET). *Review of Scientific Instruments* **75,** 3891–3893. doi:10.1063/1.1787922 (2004).

20. Kurzan, B. & Murmann, H. D. Edge and core Thomson scattering systems and their calibration on the ASDEX Upgrade tokamak. *Review of Scientific Instruments* **82,** 103501. doi:10.1063/1.3643771 (2011).

21. Pasch, E. *et al.* The Thomson scattering system at Wendelstein 7-X. *Review of Scientific Instruments* **87,** 11E729. doi:10.1063/1.4962248 (2016).

22. Falconer, I. J J Thomson and the discovery of the electron. *Physics Education* **32,** 226–231. doi:10.1088/0031-9120/32/4/015 (July 1997).

23. Hutchinson, I. H. *Principles of Plasma Diagnostics* 2nd ed. doi:10.1017/CBO9780511613630 (Cambridge University Press, 2002).

24. Bozhenkov, S. *et al.* The Thomson scattering diagnostic at Wendelstein 7-X and its performance in the first operation phase. *Journal of Instrumentation* **12,** P10004–P10004. doi:10.1088/1748-0221/12/10/p10004 (Oct. 2017).

25. Naito, O. *et al.* Analytic formula for fully relativistic Thomson scattering spectrum. *Physics of Fluids B: Plasma Physics* **5,** 4256–4258. doi:10.1063/1.860593 (1993).

26. Nolting, W. *Grundkurs Theoretische Physik 3* 10th ed. doi:10.1007/978-3-642-37905-5 (Springer, Berlin Heidelberg, 2013).

27. Sivia, D. & Skilling, J. *Data Analysis: A Bayesian Tutorial* 2nd ed. ISBN: 978-0-19-856832-2 (Oxford University Press, Oxford, 2006).

28. Hooke, R. & Jeeves, T. 'Direct Search' Solution of Numerical and Statistical Problems. *Journal of the Association for Computing Machinery* **8,** 212–229. doi:10.1145/321062.321069 (1961).

29. Metropolis, N. *et al.* Equation of State Calculations by Fast Computing Machines. *The Journal of Chemical Physics* **21,** 1087–1092. doi:10.1063/1.1699114 (1953).

30. Hastings, W. K. Monte Carlo sampling methods using Markov chains and their applications. *Biometrika* **57,** 97–109. doi:10.1093/biomet/57.1.97 (Apr. 1970).

31. Haario, H. *et al.* An adaptive Metropolis algorithm. *Bernoulli* **7,** 223–242. https://projecteuclid.org:443/euclid.bj/1080222083 (Apr. 2001).

32. Winston, R. *et al. Nonimaging Optics* 1st ed. ISBN: 978-0-12-759751-5 (Elsevier Academic Press, Burlington, 2005).

33. Scott, E. *et al.* Demonstration of an absolute Rayleigh scattering spectral calibration on the W7-X Thomson scattering system. *Journal of Instrumentation* **14,** C10033–C10033. doi:10.1088/1748-0221/14/10/c10033 (Oct. 2019).

34. Herranz, J. *et al.* Profile Structures of TJ-II Stellarator Plasmas. *Phys. Rev. Lett.* **85,** 4715–4718. doi:10.1103/PhysRevLett.85.4715 (22 Nov. 2000).

COLOPHON

This document was typeset using the typographical look-and-feel `classicthesis` developed by André Miede and Ivo Pletikosić. The style was inspired by Robert Bringhurst's seminal book on typography "*The Elements of Typographic Style*". `classicthesis` is available for both LaTeX and LyX:

https://bitbucket.org/amiede/classicthesis/